FINAL REPORT

Development of a Windbreak Dust Predictive Model and Mitigation Planning Tool

SERDP Project RC-1730

DECEMBER 2013

Eric Pardyjak
John Veranth
Scott Speckart
Sean Moran
Tim Price
University of Utah

SERDP
DOD ▪ EPA ▪ DOE

REPORT DOCUMENTATION PAGE

Form Approved
OMB No. 0704-0188

Public reporting burden for this collection of information is estimated to average 1 hour per response, including the time for reviewing instructions, searching existing data sources, gathering and maintaining the data needed, and completing and reviewing this collection of information. Send comments regarding this burden estimate or any other aspect of this collection of information, including suggestions for reducing this burden to Department of Defense, Washington Headquarters Services, Directorate for Information Operations and Reports (0704-0188), 1215 Jefferson Davis Highway, Suite 1204, Arlington, VA 22202-4302. Respondents should be aware that notwithstanding any other provision of law, no person shall be subject to any penalty for failing to comply with a collection of information if it does not display a currently valid OMB control number. **PLEASE DO NOT RETURN YOUR FORM TO THE ABOVE ADDRESS.**

1. REPORT DATE *(DD-MM-YYYY)*	2. REPORT TYPE	3. DATES COVERED *(From - To)*
16-09-2013	Final Report	04-09-2010 To 10-09-2013

4. TITLE AND SUBTITLE

Development of a Windbreak Dust Predictive Model and Mitigation Planning Tool

5a. CONTRACT NUMBER
RC-1730

5b. GRANT NUMBER

5c. PROGRAM ELEMENT NUMBER

6. AUTHOR(S)
Eric Pardyjak, John Veranth, Scott Speckart , Sean Moran , Tim Price

5d. PROJECT NUMBER

5e. TASK NUMBER

5f. WORK UNIT NUMBER

7. PERFORMING ORGANIZATION NAME(S) AND ADDRESS(ES)

University of Utah
75 South 2000 East
Salt Lake City, UT. 841128930

8. PERFORMING ORGANIZATION REPORT NUMBER

9. SPONSORING / MONITORING AGENCY NAME(S) AND ADDRESS(ES)

Strategic Environmental Research and Development Program (SERDP
4800 Mark Center Drive   Suite 17D08
Alexandria, VA 22350-3605

10. SPONSOR/MONITOR'S ACRONYM(S)
SERDP

11. SPONSOR/MONITOR'S REPORT NUMBER(S)

12. DISTRIBUTION / AVAILABILITY STATEMENT

Approved for public release; distribution is unlimited.

13. SUPPLEMENTARY NOTES

14. ABSTRACT
Fugitive dust from unconfined sources such as unpaved roads and construction areas can impair both health and visibility. In this report, the potential benefits of vegetative windbreaks in reducing vehicle-generated fugitive dust are studied and quantified using a combined experimental and computational approach. The overall hypothesis for this study is that maintaining native vegetation, establishing compatible plantings along roads, or constructing windbreaks could be a useful dust mitigation technique on military training ranges. This work focuses on PM10 dust particles with an aerodynamic diameter of 10 μm or less. The overall Objective of this project has been to address important fugitive dust issues for the Resource Conservation and Climate Change program area by developing and validating a proof-of-concept computational model for designing windbreaks for dust mitigation. The Technical Approach toward achieving this objective has been to utilize laboratory and field experiment data to develop improved models. Model development was accomplished by integrating particle dispersion and atmospheric turbulence theory with wind tunnel and field experiment data. The computational model for simulating near-road fugitive dust transport was integrated into the widely used Quick Urban and Industrial Complex (QUIC) Dispersion Modeling System. Prior to this project, QUIC had been applied to near-source pollutant transport around solid obstructions and this work extends its applicability to incorporate a novel sub-model to simulate the effects of both thin and deep vegetative canopies on wind fields and particle transport.

15. SUBJECT TERMS
fugitive dust, windbreaks, vegetation, deposition

16. SECURITY CLASSIFICATION OF:			17. LIMITATION OF ABSTRACT	18. NUMBER OF PAGES	19a. NAME OF RESPONSIBLE PERSON
a. REPORT	**b. ABSTRACT**	**c. THIS PAGE**	UU		Eric Pardyjak
U	U	U			**19b. TELEPHONE NUMBER** *(include area code)* 801-585-6414

Standard Form 298 (Rev. 8-98)
Prescribed by ANSI Std. Z39.18

ii

Table of Contents

List of Tables

List of Figures

List of Nomenclature and Acronyms

Symbol	**Meaning**
A	Area of substrates used for wind tunnel deposition tests
A'	Constant in windbreak turbulence similarity solution
B	Profile constant for vertical concentration profiles
B'	Constant in windbreak turbulence similarity solution
C	PM_{10} Concentration (may have subscripts *p* and *o* for predicted and observed)
C'	Constant in windbreak turbulence similarity solution
$\bar{c}_{int}$	Concentration at a location downwind integrated over the travel time of a plume past that location
C_c	Cunningham factor
C_o	Initial PM_{10} concentration for a fluid particle before entering vegetation
C_1	PM_{10} concentration for a fluid particle after entering vegetation
DE	Deposition Efficiency
d_e	Characteristic vegetative element size used in deposition models within QUIC
DF	Deposition Fraction
d_p	Particle diameter
F	Horizontal flux of the PM_{10} component of fugitive dust
FB	Fractional Bias
Frac	PM_{10} vertically integrated flux fraction of removal
$F_{roadside}$	Vertically integrated flux along downwind side of road
F_{min}	Minimum, constant value of F, found more than 100 m downwind
g	Gravitation acceleration constant
GUI	Graphic User Interface
H_{can}	Canopy height
H_{ic}	Height of initial cloud at roadside
H_{wb}	Windbreak height
H^*	H_{can}/H_{ic}
ID	Idaho
IOP	Intensive observational period
$K(H_{can})$	Vertical diffusion coefficient at canopy top
L	Monin-Obukhov length scale
LAI	Leaf area index (vegetative surface area per unit ground cover for a canopy)
M	Mesh spacing of turbulence grid
MODIS	Moderate-resolution Imaging Spectroradiometer
NMSE	Normalized Mean Square Error
PDT	Pacific Daylight Time
PM_{10}	Particulate Matter with an aerodynamic diameter smaller than 10 μm
q	Vertical concentration profile constant used to calculate transmitted fraction from field PM_{10} data
QUIC	Quick Urban and Industrial Complex
R_λ	Taylor-scale Reynolds number
RE	Relative Error
RHS	Right Hand Side
S_b	Travel Path within vegetation
s	Shape factor for vertical profiles of concentration.
S_b	Particle travel distance

SERDP   Strategic Environmental Research and Development Program

Stk Stokes number

Stk^* Modified Stokes number

t time

T_m^* Ratio of probability of deposition for a particle within a canopy to the probability of removal from the canopy = $(\gamma u_* H_c^2)/K(H_c)$

u Stream wise velocity component

u_i Turbulence intensity

u' Standard deviation of streamline velocity, u.

$\overline{u'w'}$ Reynolds Stresses

$\overline{u'w'}_{upstream}$ Reynolds Stresses upstream of windbreak

u_o Upstream velocity component for windbreaks

u_{Hwb} Velocity magnitude at H_{wb}

u_{ave} $(1+\alpha)^* u_{Hwb}$

Δu $(1-\alpha)/2^* u_{Hwb}$

U Particle velocity

U_o Mean wind speed for wind tunnel tests

U_s Turbulent velocity scale for windbreak flows

U_s^* Turbulent velocity scale similarity variable that accounts for variation in windbreak porosity and upstream roughness

USDA   United States Department of Agriculture

V_d Deposition Velocity

w Vertical velocity component

WA   Washington

$\bar{z}$ Mean height of PM_{10} plume

Greek Symbols

α Aerodynamic porosity

β Optical porosity

γ Vegetative density (vegetative surface area/ Unit volume occupied by vegetation)

δ_w Shear Zone Width

σ_w Variation in Vertical Velocity Component, w, upstream of windbreaks

λ_g Taylor micro-scale

ε Dissipation rate of turbulent kinetic energy

ν_{air} Kinematic viscosity of air

ρ_p Particle Density

Abstract

Objectives: Fugitive dust from unconfined sources such as unpaved roads and construction areas can impair both health and visibility. In this report, the potential benefits of vegetative windbreaks in reducing vehicle-generated fugitive dust are studied and quantified using a combined experimental and computational approach. The overall hypothesis for this study is that maintaining native vegetation, establishing compatible plantings along roads, or constructing windbreaks could be a useful dust mitigation technique on military training ranges. This work focuses on PM_{10} dust particles with an aerodynamic diameter of 10 μm or less. The overall Objective of this project has been to address important fugitive dust issues for the Resource Conservation and Climate Change program area by developing and validating a proof-of-concept computational model for designing windbreaks for dust mitigation.

Technical Approach: The approach toward achieving this objective has been to utilize laboratory and field experiment data to develop improved models. Model development was accomplished by integrating particle dispersion and atmospheric turbulence theory with wind tunnel and field experiment data. The computational model for simulating near-road fugitive dust transport was integrated into the widely used Quick Urban and Industrial Complex (QUIC) Dispersion Modeling System. Prior to this project, QUIC had been applied to near-source pollutant transport around solid obstructions and this work extends its applicability to incorporate a novel sub-model to simulate the effects of both thin and deep vegetative canopies on wind fields and particle transport.

Results: Results from this project include improved understanding of the importance of turbulence in enhancing deposition of PM_{10} dust particles onto vegetation. The results show that deposition of PM_{10} onto surfaces of all orientations is important. The results indicate that previous estimates of vegetation deposition may have been too low.

Benefits: The benefits from the project include: (i) the development of a simple predictive empirical model that can be used by practitioners/end-users to design vegetative windbreaks for reducing near source fugitive dust particulate, (ii) the development of a validated computation tool (an extension to the QUIC modeling system) for studying and predicting deposition to thin windbreaks and deep vegetative canopies.

1. Objective

This project was designed to address fugitive dust concerns for the Resource Conservation and Climate Change program area of Strategic Environmental Research and Development Program (SERDP) by developing computational algorithms and input data for predicting fugitive dust transport and emission fluxes within a few hundred meters of a road source. The objective of this project was to develop a predictive planning windbreak model for mitigating near-road fugitive dust. This was accomplished through the development of parameterizations using laboratory wind tunnel and field experiment data. These parameterizations were used to achieve improved prediction of transport, dispersion and deposition by modifying the existing Quick Urban and Industrial Complex (QUIC) Dispersion Modeling System (Singh et al. 2008; Singh et al. 2011). QUIC has been co-developed by Los Alamos National Laboratory and University of Utah. A real-time running prototype of the modeling system was demonstrated in the field at Hanford, WA. The proposed computational model for simulation of fugitive dust mitigation by windbreaks addressed two Resource Conservation and Climate Change areas: (a) prediction of fugitive dust transport and emission fluxes and (b) integration of meteorological conditions and local field conditions to quantify the potential transport of dust plumes. This project extended existing computational models to provide a proof-of-concept tool for use in evaluating the potential dust emissions of upcoming training activities based on site-specific terrain and meteorological data. The tool can also be utilized in mitigation strategies.

The parameterizations utilized to improve QUIC as a prediction tool included: a dry-deposition model that incorporated the enhancement of deposition due turbulence (this effect had been neglected in previous models, see e.g. Raupach et al. 2001) and models for the influence of windbreaks on mean and turbulent wind fields. These models are applicable for windbreaks of varying porosities and upstream roughness conditions.

In addition, as part of this project, we used our improved QUIC simulations and field data to develop a simple "empirical equation" predictive model that can be used by practitioners/end-users to estimate how different vegetation configurations can reduce near-source emissions by a specified fraction. This model can be utilized with relatively easy to obtain information about a specific site.

The final major contribution of this project was the implementation of our wind tunnel based parameterization into QUIC. The new results compare well with the experimental data; reproducing the trends and the magnitude of the results (Relative errors in concentration predictions for the two field experiments were 12% and 9.6%). In addition, the new model strongly indicates that the reason previous dispersion studies required such unrealistically small deposition length scales for vegetation to obtain deposition amounts consistent with experimental data was the failure to include turbulence in the deposition parameterization.

2. Background

2.1 Description of the Problem

The focus of this project has been on trying to understand the interaction between vegetation and particulate matter near a fugitive dust source where the dust plume is moving horizontally through vegetation. We have concentrated on the Environmental Protection Agency's criteria pollutant PM_{10} (particulate matter with a diameter of 10μm or smaller). Near-road fugitive dust can interact with thin windbreaks or native vegetation canopies; hence, we have focused our study on these two limiting cases. The thickness of a windbreak is generally the same order of magnitude as the windbreak height, H_w, or less. That is, windbreaks are relatively "thin." Native vegetation generally extends a long distance downwind of a road source and consequently has a fetch depth that is very large. The physics of the flow field governing these two situations is quite different. The contrasting features for a canopy and windbreak are shown in Figure 1. Note that the coordinate system origin is located along the vehicle's path of travel. The distance from the path of travel to the windbreak or native vegetation is taken to be small in this work. The distance between the road and the start of the vegetation is an important parameter that can substantially impact the effectiveness of the vegetation's ability to reduce downwind concentrations. The further from the road the vegetation, the more time the dust has to mix vertically, effectively increasing the "source height". As will shown in the results, the ratio of the source height to the height of the vegetation is an important governing parameter.
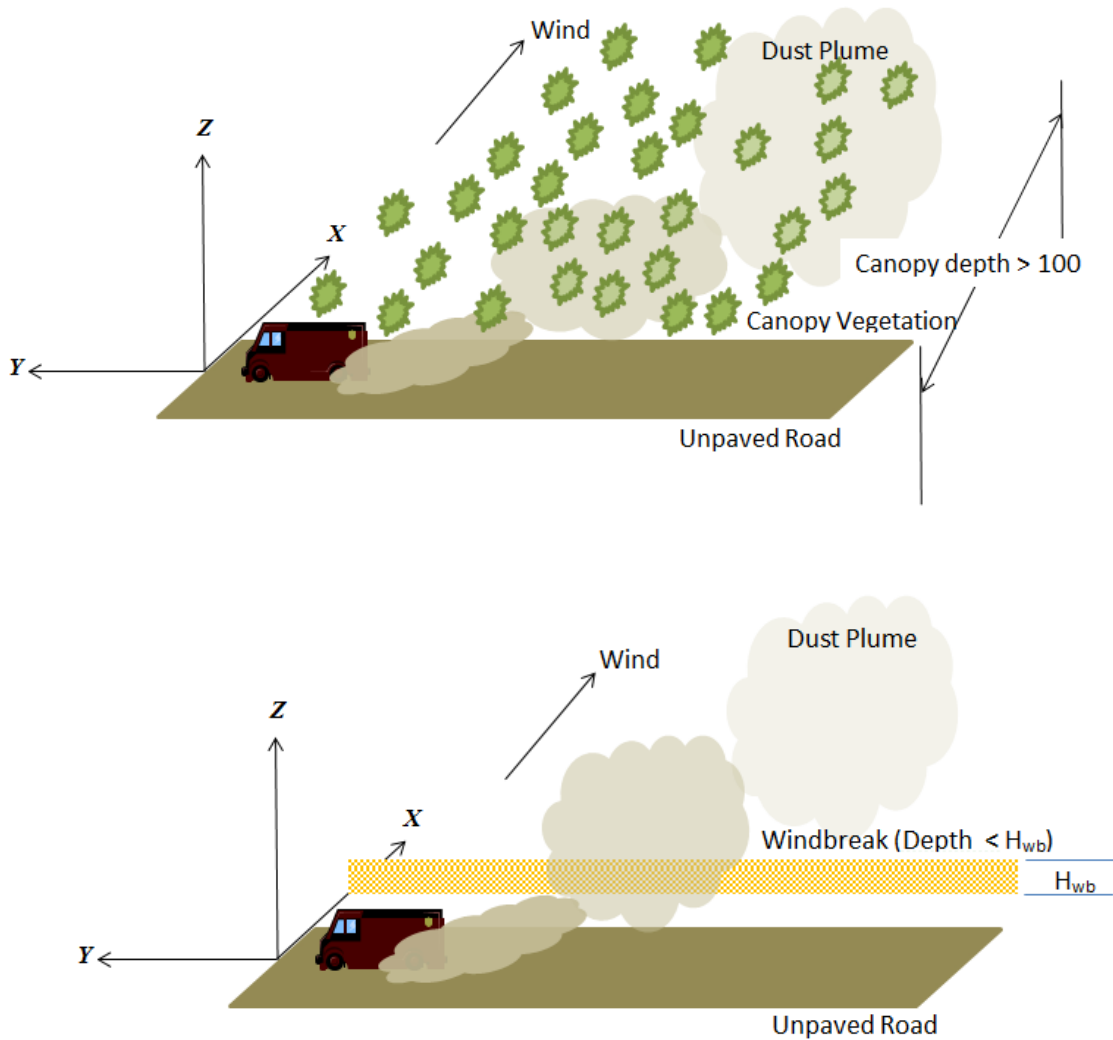
Figure 1: Illustration of the differences between windbreaks and canopies along with the coordinate system used for simulations and field studies involving unpaved roads. Windbreaks are very thin with a fetch depth comparable or less than their height, while canopies have an infinitely deep fetch. Both are shown in the context of the current project downwind of an unpaved road.

Referring to Figure 1, assuming that the road is long and that end effects can be neglected, fugitive dust emissions and concentrations are independent of the y-axis because of the road's length. Hence, fugitive dust emissions depend only upon two directions (height above ground and downwind distance from the road) and the problem can be assumed to be quasi two-dimensional.

As illustrated in Figure 2, away from the leading edge, the flow within a canopy is nearly does not substantially change with increasing downwind distance. Because of this, the flow depends only up the height above the ground, z. In contrast, for a windbreak, the airflow is continually recovering from the disturbance caused by the windbreak. This recovery can be delayed as far

downwind as ~50 H_{wb}. Because of this, a windbreak profile is a function of height, z, and downwind distance, x. In this project, we have used several simplifications to characterize important physical vegetative characteristics that effect both momentum and particle transport. For example, the behavior of the flows for both windbreaks and canopies depend on the amount of vegetative surface area present. For canopies, this can be expressed by Leaf Area Index (LAI). LAI is defined as the vegetative surface area per unit of ground covered by the canopy. In this work we assume that vegetative surface area is distributed uniformly through the canopy (both vertical and horizontally). The density of the vegetative or γ is obtained by dividing the vegetative surface area by the volume of the canopy. It is the surface area per unit volume. For windbreaks optical porosity, β, is the measureable parameter indicating thickness. γ can be obtained from β by using the relationships from the literature (e.g. Raupach et al. 2001).
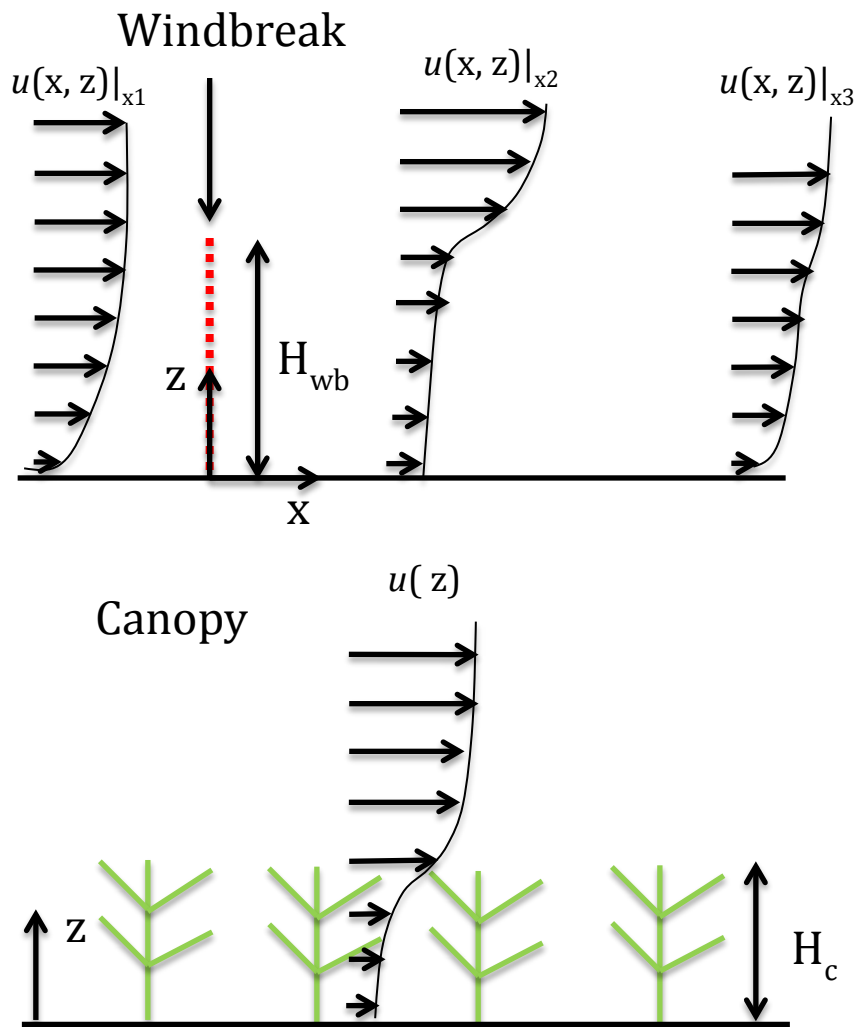
Figure 2: Velocity profiles further illustration of the differences between windbreaks (top panel) and canopies (lower panel). The mean velocity profile downstream of a windbreak is continuously changing and slowly approaches the upstream profile, while a mean canopy profile is relatively independent of position within the canopy.

2.1 Windbreak Literature

There have been many studies focusing on different aspects of windbreaks (or shelterbelts) and their applications in the literature. *Windbreak Technology* from the Proceedings of an International Symposium on Windbreak Technology (Brandle, 1988) provides an excellent overview of the many uses of windbreaks including their role in mitigating wind erosion, snow movement and agricultural spray drift; their role changing crop yield, as well as surface energy balances and evaporation rates. Many field campaigns, wind tunnel experiments, analytical analysis, and numerical modeling activities have been undertaken in this field. Field studies of windbreaks have included the work of: Bradley and Mulhearn (1983), Nord (1991), and Wilson (2004). Wind tunnel studies have included: Plate (1971), Judd et al. (1996), Perrera (1981), and Guan et al. (2003). Numerical modeling studies have included using various forms of the Reynolds Averaged Navier-Stokes equations (Wang et al., 2001; Wilson, 1985; Bourdin and Wilson, 2008; and Santiago, 2007). In addition, high-resolution Large-Eddy Simulations of windbreaks were conducted by Patton et al. (1998). Analytical analysis include: Counihan et al. (1974) and Wilson (1990). A few of these studies develop empirically based expressions for the mean wind and turbulence (some of which have been utilized in the present work). These studies include: Perrera (1981), Bradley and Mulhearn (1983), Counihan et al. (1974), and Guan (2003). In the work conducted for this SERDP project, we have drawn extensively from this literature.

Despite the common need of the current work and other windbreak studies to either model or characterize the mean and turbulence wind fields, there are substantial differences with respect to the particles studied. Tabler (1991 and 1992) examined the mitigation of transport of snow across highways. Other windbreak studies have been concerned with the transport of sand (Musick and Gillette, 1990), which typically has a size range between 60-2000 μm. Another important large particle application is spray drift mitigation of pesticides/insecticides, which have droplet diameters that are several hundred microns (Wood et al., 2001). Such particles are much larger than PM_{10}. Because of the larger particle sizes appearing in this part of the windbreak literature, the relevant removal mechanisms are different from the current work. PM_{10} tends to be impaction dominated rather gravitational settling dominated, which is usually the case for the large particle problems. Gravitational settling is well understood and accurately described by parameterizations in the literature (e.g. Seinfeld and Pandis, 1998). Impaction is much less understood and a significant aspect of the current work is to improve impaction modeling for PM_{10}. Since the primary deposition mechanisms associated with large particle and small particle deposition are fundamentally different (gravitational settling versus impaction), the QUIC simulations for the transport of PM_{10} are not comparable to the transport of larger particles such as sand. There is, however, a need to tie QUIC and the findings from this work to these other large particle problems since many applications may have a wide range of particle sizes. This is discussed further in the recommendations for future work.

In this work, we have attempted to experimentally characterize the critical factors influencing particle transport and deposition in vegetation so that modeling of these processes can be improved. In the following sections we first present our technical approach (methodology and theory) followed by important results from our research. The technical approach and results are organized by basic tasks that needed to be completed. Hence, we begin with a description of the wind-tunnel studies that were used to improve our understanding of turbulence on particle

deposition and to develop a new deposition model. We then transition to numerical model development for the extended QUIC model and the theoretical foundations of the sub-models. Next, a discussion of the new field experiments that were conducted during this project is presented. Finally, a description of the new simple "empirical equation" predictive model is presented.

3. Materials and Methods

The project can be broken up in to three areas: laboratory measurements, field experiments, and model development and prototype demonstration. In the following sections, we begin by describing the laboratory measurements, then the modeling approach, followed by the field experiments.

3.1. Laboratory Wind Tunnel Measurements

3.1.1. Deposition Experiments
Wind tunnel experiments were performed to test our hypothesis that enhanced turbulent mixing from the interaction of a vegetative canopy with vehicle-generated dust will increase total deposition onto vegetative surfaces. More specifically, several existing models are based on laminar flow impaction theory (e.g. Raupach et al., 2001; Aylor and Flesch, 2001) for deposition to vegetative canopies and windbreaks that do not account for the details of the turbulence eddy sizes and strength of the local fluctuations. Previous field studies have reported and observed increased deposition in a vegetative canopy (Veranth et al. 2003). Deposition measurements were accomplished using a fluorimetry measurement technique that measures known amounts of fluorescein ($C_{20}H_{10}Na_2O_5$, Sigma-Aldrich) aerosol particles deposited onto substrates. Three different sizes (0.25 cm^2, 1.00 cm^2, and 1.44 cm^2) of hard plastic polypropylene square substrates (1 mm thick) were attached on a six-axis deposition frame. Small holes were drilled along the centerline of the frame and 24-gauge wire was woven into the frame to create a directional matrix for the substrates to be placed. Substrates were held onto wire using a pressure-sensitive adhesive (Blu-Tack, Bostick Inc.). Figure 3 shows a schematic of the experimental apparatus used.
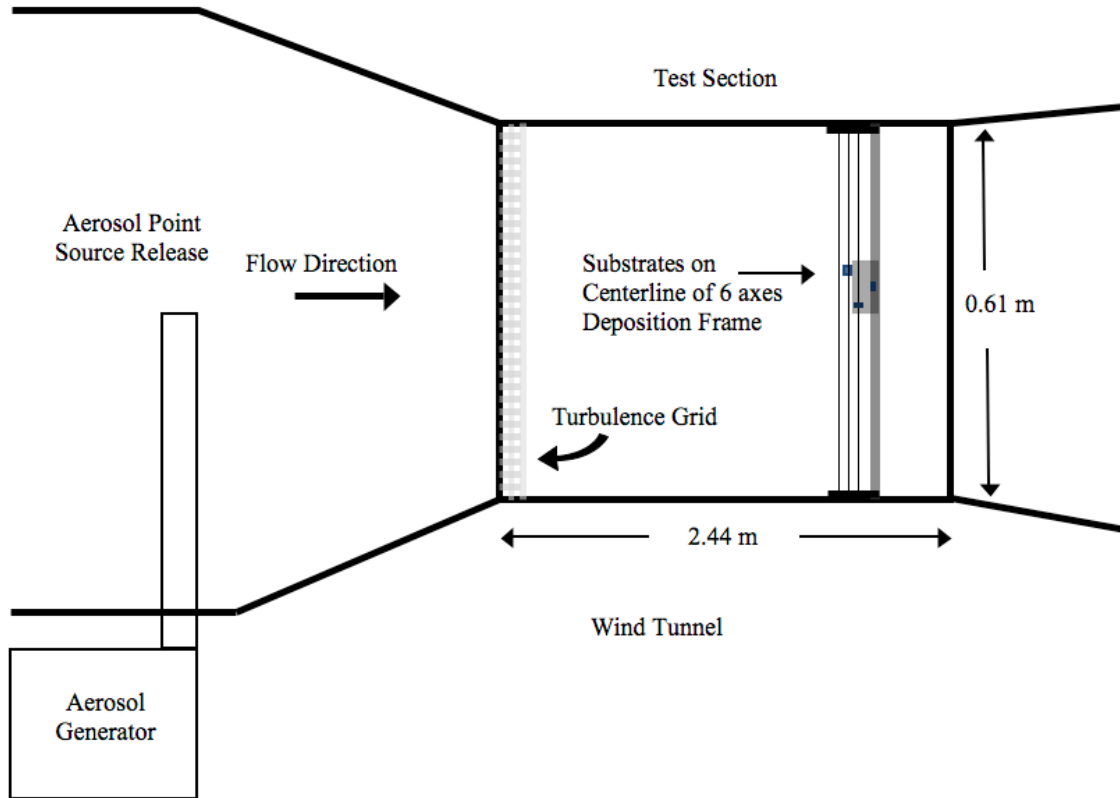
Figure 3: Schematic of the wind tunnel deposition experimental apparatus (not to scale).

To test our hypothesis of deposition enhancement from turbulent motions, a grid designed to generate isotropic turbulence was constructed with a solidity or open area ratio of 0.5 and placed just downstream of the converging section of the wind tunnel upstream of the deposition surfaces. Grid-generated turbulence was selected for these experiments because it may be used as a close approximation to idealized homogenous isotropic turbulence. Since this type of flow has been studied extensively both experimentally and theoretically (see Pope 2000 for a review), it provides an ideal experimental framework for relating various scales of turbulence to deposition characteristics.

The aerosol generator used was an Ultra Sonic Humidifier (Model V5100NS, Kaz Inc.). It was positioned on a stand beneath the wind tunnel and the aerosol was piped up to the centerline of the wind tunnel using polyethylene tubing. The aerosol injected into the wind tunnel was a mixture of 80% distilled water, 20% glycerol, and 0.5 mg of soluble fluorescein per ml of solution. A laser-based aerosol spectrometer (Model 1.109 Grimm Technologies Inc.) was used to analyze the size range and concentration of aerosol being measured at the points of deposition inside the wind tunnel. The aerosol diameter (after initial water evaporation) was relatively evenly distributed over the size range between 1-5 μm.

Regardless of substrate size, location, or mean wind velocity, the aerosol was injected into the test section for one hour to allow for accurate mass deposition measurements. Each experiment was repeated three times as the substrate locations were rotated clockwise after each experiment. The procedure was used to average out any variations or errors that might exist in the concentration amounts at individual substrate locations and to carry out each experiment on all

six axes simultaneously. Figure 4 shows a schematic for how the substrates were placed onto the deposition frame. Substrate
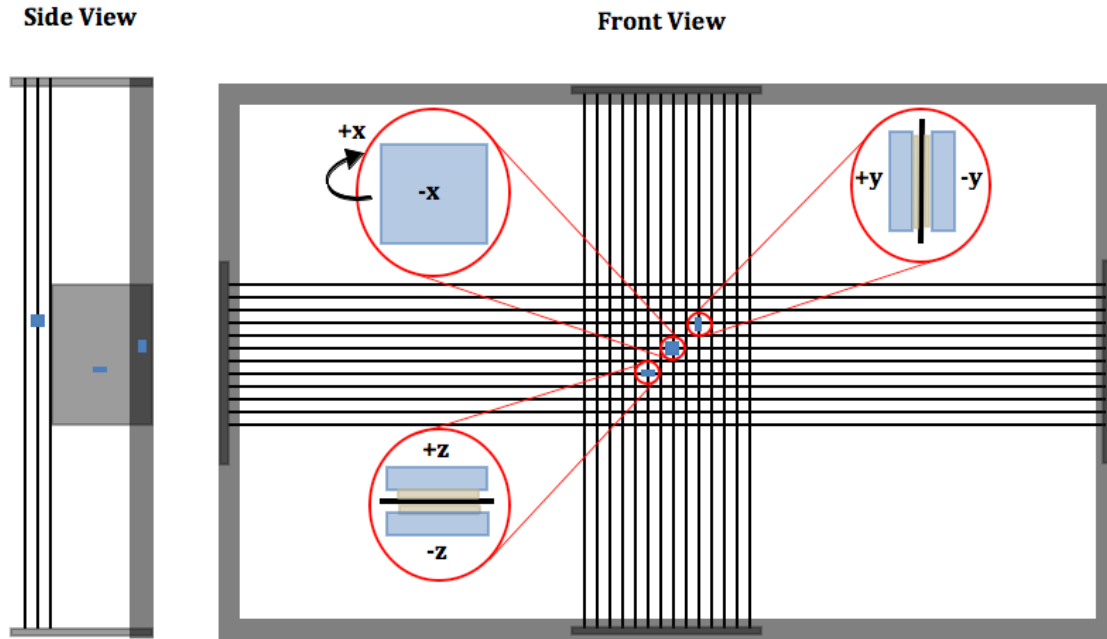
Figure 4: Side view (left) and front view (right) of the deposition frame showing plastic substrates attached to 24-gauge wire. Note in the side view, the flow is from left to right and in the front view flow is directed into the page.

locations were designated in accordance to the right-hand rule facing downstream of the wind tunnel. Since 6 substrates were used (±x, ±y, ±z) for any given experiment, the substrates were sandwiched together using Blu-Tack, while the 24-gauge wire was used as the structure to keep the substrates in a fixed location without substantially modifying the flow field. The amount of fluorescein deposited onto each substrate was measured using a fluorimeter, which enabled quantification of the deposition fraction (*DF*). Here, *DF* is defined as the ratio of the mass of fluorescein deposited on each substrate to the total amount of fluorescein available in the volume of air intercepted by the substrate cross section over one hour. In order to obtain different turbulence intensities and length scales, the deposition frame was placed at 1.80 and 2.13 m downstream of the grid.

After each deposition experiment, the substrates were carefully removed from the wires using surgical clamp forceps, and then washed in a test tube with 2 ml of distilled water. Each substrate was individually washed in distilled water and analyzed in a fluorimeter. The fluorimeter outputs a dimensionless reading of fluorescence intensity. Therefore, in order to quantify the amount of fluorescein that was deposited on each substrate a dilution series was used to develop a calibration curve. A linear regression analysis was used to correlate concentration amounts of fluorescein deposited on individual substrates to the output fluorescence measured by the fluorimeter. A good linear fit (R^2=0.998) was obtained over the range of experimental data. The linear fit was then used to calculate the mass of fluorescein that was deposited. The deposition fraction was determined as follows:

$$DF = \frac{M}{U_o Atc}$$

(1)

where, M is the ratio of fluorescein mass deposited to the total amount of available fluorescein in the airstream over a one hours sampling period, U_o is the mean velocity, A is the area of the substrate used, t is the run time of the experiment, and C is the concentration value measured at the location of deposition. The concentration was determined from optical measurements using a GRIMM 1.109 particle spectrometer instrument. DF was calculated for all six axes.

3.1.2. Vegetation Deposition Experiments

Wind tunnel deposition experiments were also conducted on various vegetative elements including artificial broad leaf, branch, grass, and metal welding rod elements (see Table 1 for a summary of experiments). The experimental procedure was very similar to the above artificial substrate deposition experiments using the same wind tunnel, aerosol generator, fluorescein mixture, and fluorimeter. However, unlike the artificial substrate experiments, the deposition experiments were only conducted at 1.80 m downstream and only with the turbulence grid in place. The purpose of these experiments was to verify that the turbulence enhanced deposition parameterizations found for the artificial substrates were valid for more realistic vegetative elements. The primary difference between the vegetation experiments and the artificial substrate experiments is that the resulting deposition fraction is an *integral* quantity over the entire area of the vegetative element. The fluorescein mass deposited was measured for the entire element rather than isolating for each surface and orientation. It is believed that this better matches what would be required for a real-world vegetative deposition efficiency model.

The area of the irregular leaf, grass, and twig elements was required to calculate the deposition efficiency (Eq. 1). In the case of the broad leaf and grass samples, direct measurement of the area was impractical. A pixel counting technique was used to measure the frontal area. Each of the samples was photographed with a Canon XSi DSLR camera on grid paper and the photo was loaded into Adobe Photoshop CS5.5. Using the "Magnetic Lasso" tool, the perimeter was traced via contrast detection methods. The number of pixels in the leaf area and known area of grid cells on the paper were recorded. The area of the leaf was then calculated by Eq. 2.

$$Leaf\ Area = \frac{Control\ Area}{No.Pixels\ in\ Control\ Area} \times No.of\ Leaf\ Pixels\ .$$

(2)

Substrate	Orientation	Average Max Width or Diameter (mm)	Average Area (mm²)
Square Polypropylene	± X, Y, Z	5, 10, 12	25, 100, 144
Broad Leaf	0°, +45°, -45°, Edge-On	26.3	1279.6
Onion Grass	0°	1.0	47.0
Twig	0°	2.5	192.0
Welding Rods	0°	0.89, 1.57, 2.39	44.45, 78.74, 119.38

Table 1: Summary table of the various deposition experiments run in the wind tunnel. Note that a 0° orientation indicates that vegetative surface of greatest area was oriented normal to the incoming wind.

Broad leaf and grass area were calculated with this method and it was found to be very repeatable with < 1% error. The area of the twigs was performed with a statistical sampling technique where the diameter was measured at 6 positions along the length and the area was calculated using the average diameter measurement and the length. The projected frontal area for the welding rods was calculated by simply measuring the diameter and multiplying by the length.

In addition to taking photographs to calculate the area of the leaves and grass samples, pictures were taken of the samples before, during, and after the wind tunnel deposition experiments. Photographs were taken of the leaf (or grass) in position without any air flow, just after initial startup, near the end of the test, and after the tunnel had completely stopped. The purpose of these pictures was to quantify the streamlining of the leaf in the wind and any permanent relaxation after the test was finished.

Due to the various shapes and deposition regimes tested in the wind tunnel, the run time required for each element type to achieve sufficient fluorescence signal without over saturating the surface varied according to element width and the tunnel wind speed. Also, the volume of the washing fluid varied from 1-10 mL based on the physical size of the element.

3.1.3. Hot-wire Turbulence Quantification Experiments

A single-sensor straight-wire hot-wire probe (55P16 Probe, Dantec Dynamic Inc.) was placed in the wind tunnel to gather turbulence data to correlate deposition enhancement to the proper scales of turbulence in the wind tunnel. Traditionally, the Taylor-scale Reynolds (R_λ) number is used to characterize grid turbulence (Pope 2000), therefore, hot-wire probes were used to accurately determine the streamwise r.m.s. of the streamwise velocity (u') and the Taylor micro-scale (λ_g):

$$R_\lambda = \frac{u' \lambda_g}{\nu_{air}}.$$ (3)

We hypothesize that the Taylor micro-scale (λ_g) is the turbulence scale most responsible for enhanced deposition because this length scale is shown to have the smallest dynamic eddies (Tennekes and Lumley 1972). At these smaller scales, we expect the eddy-sizes of the micro-scale to interact with the aerosol particles and contribute in actively depositing these particles onto the substrate surfaces. These eddies are still capable of transferring energy to much smaller

dissipative scales. Therefore, we believe λ_g should play an important role in characterizing deposition onto known surfaces. This is shown in Figure 5.
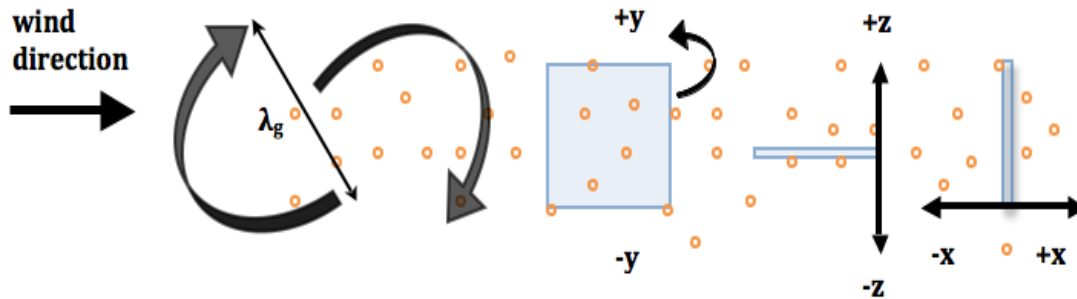
Figure 5: Schematic showing the interaction of turbulent eddies with a size on the order of the Taylor micro-scale with the particles that deposit onto the surface of the substrates.

The hot-wire probe was calibrated using the University of Utah portable hot-wire calibration test facility before each experiment. Data were sampled at 25kHz using an AN-1003 Anemometry system (AA Lab Systems Ltd), BNC 2110 I/O ADC (National Instruments), NI-6122 DAQ (National Instruments), and Labview 10. A differential pressure transducer (10 Torr MKS Baratron) and hot-wire probe were colocated at the exit of the converging calibration facility. A third-order polynomial fit was applied in order to develop a calibration curve and equation for the wind tunnel measurements (Bruun 1995; Tennekes and Lumley 1972). Hot-wire calibration was performed both before and after the data were acquired in the wind tunnel and the average of the two calibration equations was used in the final data analysis. The calibration is shown below in Figure 6. Data were then taken at four separate locations in the test section of the wind tunnel. These locations were identical to those of the deposition measurements.
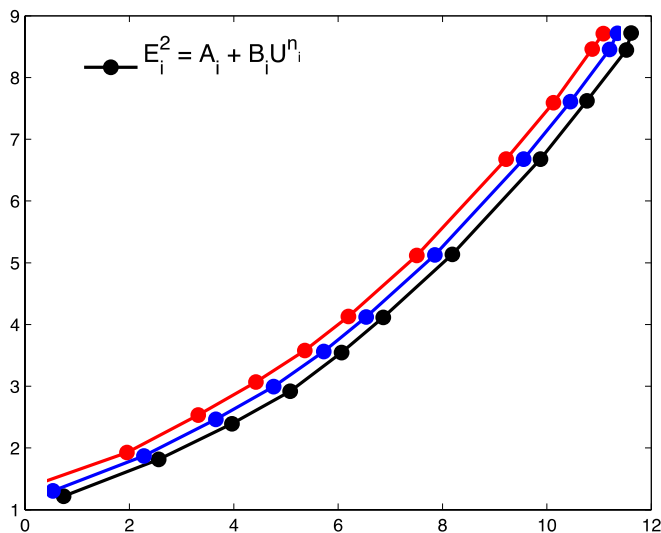
Figure 6: Hot-wire probe velocity (U) – voltage (E) calibration curve. Calibration was performed both before (subscript i) and after (subscript f) data collection in the wind tunnel. The average curve (subscript ave) was used to process the data. A, B and n represent best-fit coefficients.

3.2. QUIC Model Development

An important aspect of this project has been the development of new models for predicting deposition onto vegetative windbreaks. In particular, added the new models to an existing software system maintained at Los Alamos National Laboratory called the QUIC (Quick Urban and Industrial Complex) Dispersion Modeling System- (Pardyjak and Brown 2001; Williams et al. 2004; Singh et al. 2008; Singh et al. 2011). QUIC has been co-developed by researchers at the University of Utah and Los Alamos National Laboratory over the past decade and computes 3D high-resolution flow fields and particle dispersion around building in urban areas. QUIC is composed of a wind solver (QUIC-URB), which computes wind fields based using initialized wind fields based on simple experimental parameterizations and then forces the flow field to be mass conservative (Singh et al. 2008). For dispersion modeling the system uses QUIC-PLUME, a random walk or Lagrangian particle dispersion model (Williams et al. 2004). QUIC also has an easy to use Graphic User Interface (GUI) that allows for building the simulation domain and visualizing results. Prior to this project, QUIC did have not vegetative windbreak capabilities, however, because of its ability to simulate urban and other complex flow and dispersion problems and its free availability, it represented an excellent base to build upon. Figure 7 below shows an illustrative example of the type of results that are easily obtained using the QUIC model.
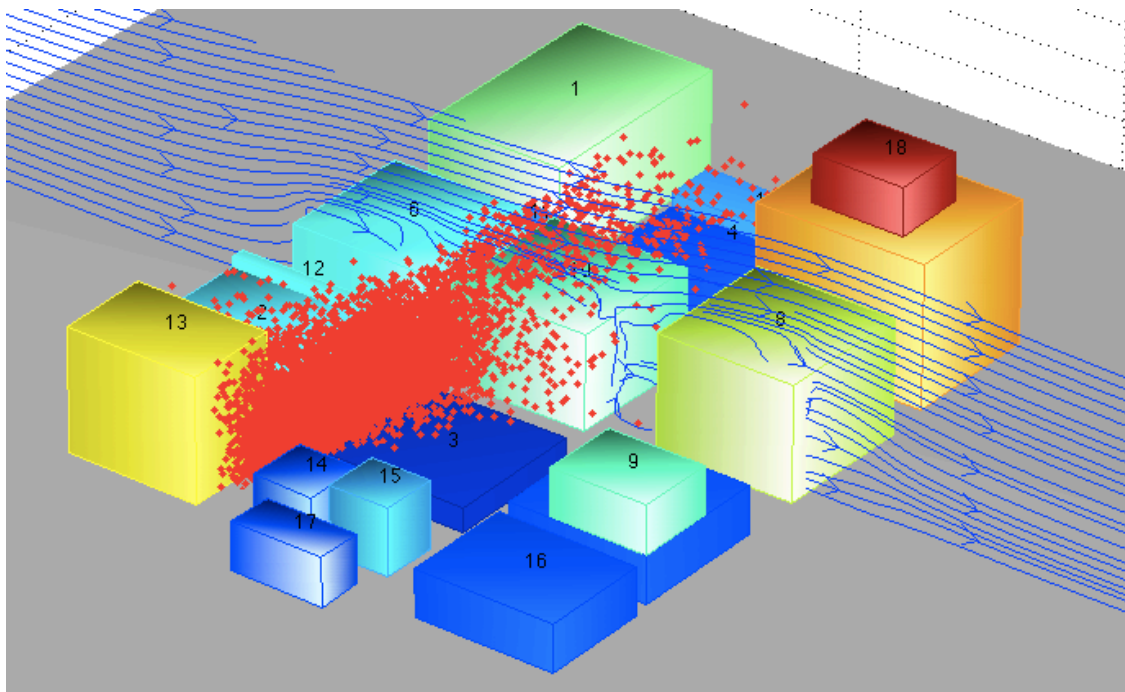
Figure 7: Illustration of an urban flow and dispersion simulation using QUIC. QUIC is the based model that was built upon in this project.

3.3.1 Improved Mean Wind and Turbulence Modeling for Windbreaks

Windbreaks, such as a single or few rows of trees or fences are common roughness features found alongside roads (Judd et al. 1996). A goal of the current SERDP project is to successfully model horizontal advection and turbulent diffusion, along with deposition within single and arrays of windbreaks within the QUIC platform.

A qualitative description of flow resulting from the placement of windbreaks is shown in Figure 8 and is documented in Judd et al. (1996). Starting on the left of the figure, one finds the typical upwind approach profile found in the atmospheric surface layer. The letter A indicates this. As the flow approaches the windbreak, the flow slows down in the streamwise, or x direction, and as a consequence of mass conservation, the vertical velocity component increases. On the leeward side of the windbreak the flow is divided into two regions dependent upon height: for $z>H_{wb}$ there is an accelerated displaced flow, denoted by the letter C. For $z<H_{wb}$ flow velocities and turbulence intensities are lower than in the approach profile. The flow for $z<H_{wb}$ is divided into the bleed flow region directly leeward of the windbreak, and the quiet zone located downwind of the bleed flow region. These zones are denoted by the letters B and D respectively. In the red cone shaped region (shear zone denoted by letter E), the displaced flow interacts with the quiet zone in an area containing relatively high shear. As the shear zone entrains fluid, it decreases in intensity and eventually contacts the ground and develops into a re-equilibrium zone denoted by the letter F. In the re-equilibrium zone the profile slowly develops back into the approach profile.
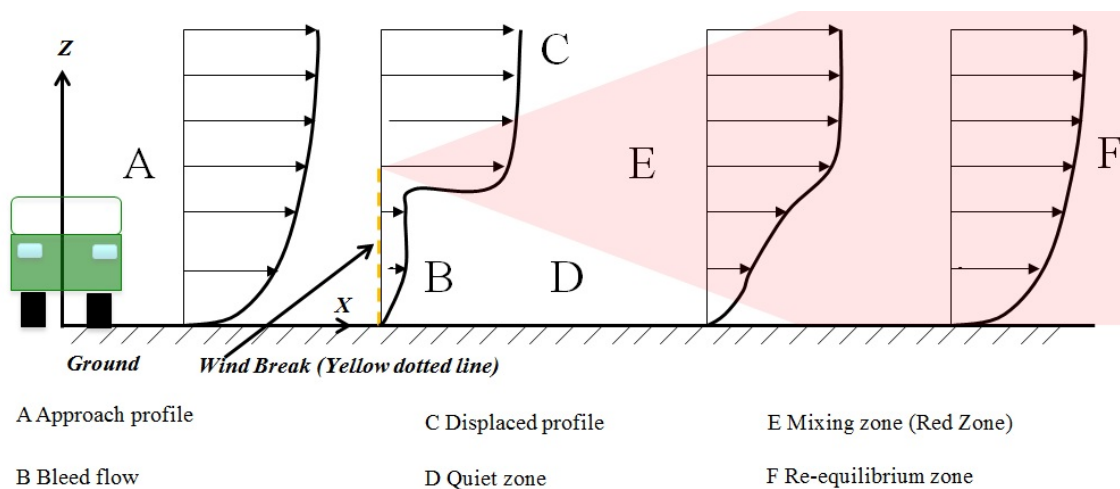
Figure 8: Flow zones and velocity profiles downwind of a windbreak as defined in Judd et al. (1996) together with the road orientation utilized in the current simulations and field studies.

Mean Wind

This section details the methods utilized to implement the fast response windbreak model within the constructs of the QUIC dispersion modeling tool platform. To summarize, the QUIC platform utilizes an empirically based initial wind field. This initial wind field will, in general, not be mass conservative. QUIC utilizes a basic variational analysis procedure to modify the

initial wind field into a mass conservative wind field. The majority of the research effort in the current project is to define this empirically based initial wind field (Singh et al. 2008).

The basic modeling procedure used here utilizes existing high-resolution wind tunnel data sets. Judd et al. (1996) and Guan et al. (2003) performed wind tunnel studies of windbreaks with varying optical porosities and proposed some simple models that we are utilizing for the initial non-mass conservative velocity field in QUIC. The basic methodology is illustrated in Figure 9. The physical region upwind and downwind of an infinitely thin windbreak is sub-divided. A different parameterization is utilized in each region for the initial non- mass conserved velocity field. For Region 3, shown in red, we adopt the similarity solution parameterization proposed by Perera (1981). This solution is a function of the optical porosity, windbreak height, downwind distance, height, upstream surface roughness and displacement height. It is a similarity solution that is not applicable directly downwind of the windbreak. It is applicable at distances at least 7.5 times the windbreak height (7.5 H_{wb}) downwind.
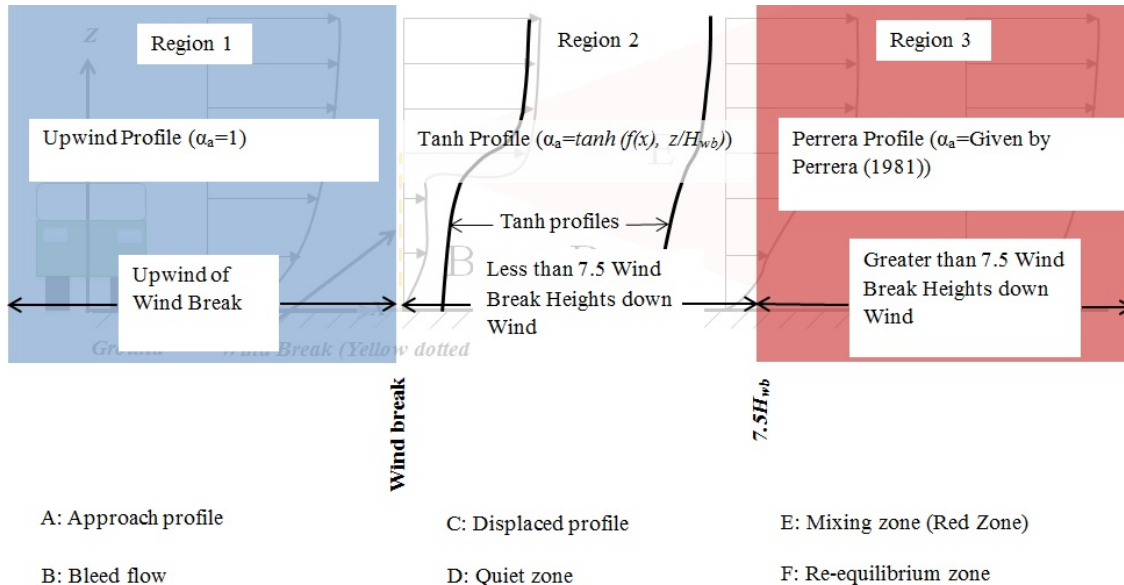
Figure 9: Illustration of division of windbreak flow geometry into three regions that extend from the ground to an infinite height vertically. The border between Region 1 and 2 (the blue and white regions) is the location of the windbreak. The border of Region 2 and Region 3 (the white and red regions) is a line extending from the ground vertically to the top of the simulation domain located 7.5H_{wb} downwind of the windbreak.

In Region 1 (shown in blue), upwind of the windbreak, changes in the upstream profile are minimal. However, as previously noted there is a deceleration in the profile as it approaches the windbreak, as well as acceleration over the top of the windbreak. It is assumed that the variational procedure in QUIC will be sufficient to model these components. Hence, all locations upwind showed in blue use a simple boundary layer profile for the initial non-mass conserved field. For Region 2, shown in white, the aerodynamic porosity as defined by Guan et al. (2003) is helpful. It is defined in Eq. 4, as:

$$\alpha(x,z) = \frac{u(x,z)}{u_o(x,z)}.$$

(4)

Where $\alpha(x,z)$ is the aerodynamic porosity, $u_o(z)$ is the upstream velocity at height z, and $u(x,z)$ is the local velocity. α is 1 when the local velocity and the upstream velocity are identical. Any reduction in momentum will decrease α.

In Region 2, we propose to model α and then multiply α by the upstream velocity at the given height to determine the velocity, rather than directly estimating the velocity. The reason for this indirect method is that α is generally easier to model than the wind velocity. To illustrate this point, take for example, the upwind profile. It can be many different relatively complex curves. However, the upwind aerodynamic porosity is always a very simple constant function equal to 1.

In Region 2, a one-dimensional vertical function is implemented. The inputs for this vertical function vary with increasing distance downwind from the windbreak. The behavior of the function needed in the direct downwind zone is as follows: at heights much greater than the windbreak, for example 2 to 3 times H_{wb} α is 1. At heights just behind the fence, for $z < H_{wb}$, α is a function of the windbreak's optical porosity. Also, there is a similarity of the flow directly downwind of the windbreak to that of a classical mixed layer. These properties suggest that a hyperbolic tangent function, *tanh*, would be appropriate to model α in Region 2 just downwind of the windbreak. The *tanh* function is a well-behaved function with limits of 1 and -1 that are approached as the function inputs approach ∞ and $-\infty$ respectively. High above the windbreak the function naturally approaches the limit for α, of 1. Near the ground, behind the windbreak, the function may be modified to approach the aerodynamic porosity of the windbreak. Visually this is shown in Figure 9. With the mathematical function defined, two sub models are needed to complete the zone and are described in following section.

Windbreak Bleed Flow Model
Guan et al. (2003) propose a model for the flow through a windbreak, the so-called "bleed flow." A bleed flow model relates a windbreak's optical porosity, β, to the value of α directly behind the fence. Guan et al. (2003) propose two different models: 1) for thin windbreaks such as fences and 2) for relatively thick fences such as rows of trees. The models are presented respectively as:

$\alpha = \beta$ (thin windbreaks)   (5)

$\alpha = \beta^{0.4}$ (thick windbreaks)   (6)

The value of α then replaces the lower limit of -1 for *tanh* as the ground is approached.
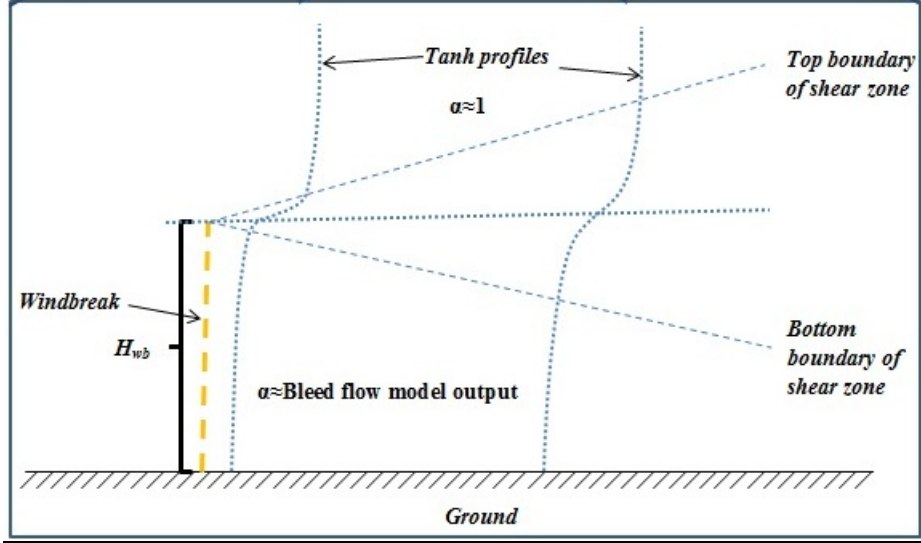
Figure 10: A detailed view of Region 2. Illustrations of the use of the *tanh* function in vertical velocity profiles on the leeward side of the windbreak. Note the origin of the *tanh* function, the dotted horizontal line originating at the top of the windbreak. Note also the top and bottom boundaries of the shear zone. The difference between these two lines is the shear zone depth δ.

Windbreak Shear Wake Model
An additional step in defining the zone adjacent and downwind of the windbreak is the rate of spread of a zone of relatively high shear just downwind of the top of the windbreak. These are shown in Figure 10 by the blue dotted lines than run diagonally downwind of the top of the windbreak and are labeled "top boundary of shear zone" and "bottom boundary of shear zone." Judd et al. (1996) present the following model to estimate the rate of spread of this high shear zone in the stream wise direction:

$$\frac{d\delta}{dx} = \left(\left(0.14 \frac{\Delta u}{u_{ave}} \right)^2 + \left(\frac{2\sigma_w}{u_{Hwb}} \right)^2 \right)^{1/2} . \tag{7}$$

Where, u_{Hwb} is the upwind velocity at the windbreak height, σ_w is the variation of the vertical velocity component, w, Δu is $u_{Hwb}*(1-\alpha)$, and u_{ave} is $u_{Hwb}*(1+\alpha)/2$. This model defines the rate of spread of the shear zone. The thickness of the shear zone is 0 at the top of the windbreak. It then increases as the Judd et al. (1996) model dictates. To relate the rate of spread to the *tanh* function, a definition utilized by researchers of classical mixing layers is needed: the thickness of this shear zone accounts for 90% of the difference between the two velocity streams. This 90% criterion corresponds to inputs of 1.5 and -1.5 in the *tanh* function.

Lastly, the origin of the *tanh* function must be determined. This is shown as a horizontal dotted line originating at the top of the fence and continuing on the leeward side in Figure 10. Judd et al. (1996) note that the inflection point of the velocity profile, the origin of the *tanh* system, is nearly located on one streamline that passes through the pointed located at the windbreak height in the upwind profile. Because the vertical velocities, w, needed to determine stream lines are incorrectly assumed to be zero before QUIC performs the variational procedure, this streamline

is incorrectly assumed to be the horizontal dotted line. To correct this, a second execution of the variational procedure is performed. After the second variational procedure, the streamline is correctly modeled by taking into account the non-zero w values. Graphically, this is shown in Figure 11 with the modified streamline after the second variational procedure shown in red. It is found that additional runs of the variational procedure produce no changes in the origin of the *tanh* coordinate system, thus the variational procedure is performed only twice. The procedure is shown in Figure 12.
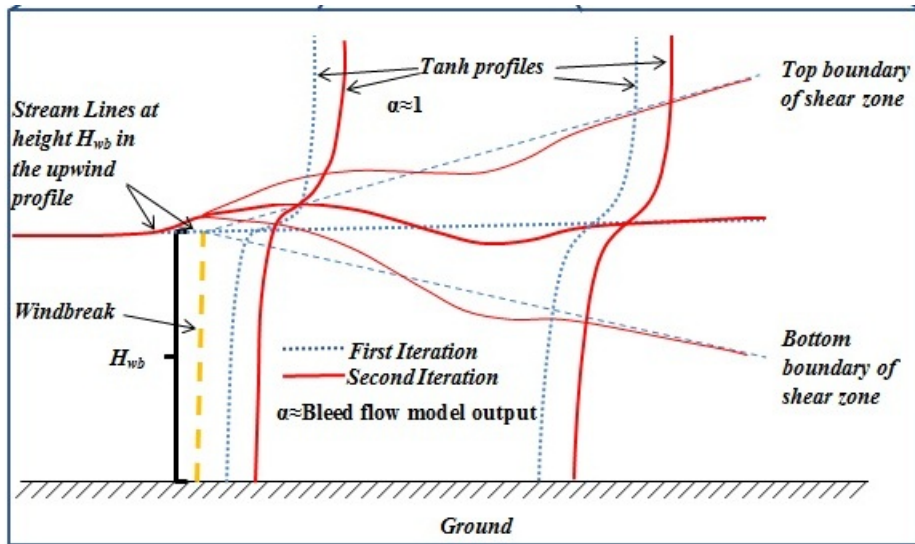
Figure 11: Illustration of the results from the second (correctional) variational procedure for the mixed layer at the top of the windbreak. The second variational procedure, or iteration, accounts for vertical velocities present over windbreaks, and as a consequence more accurately places the origin of the *tanh* function along the streamline originating at the windbreak height in the upwind profile.
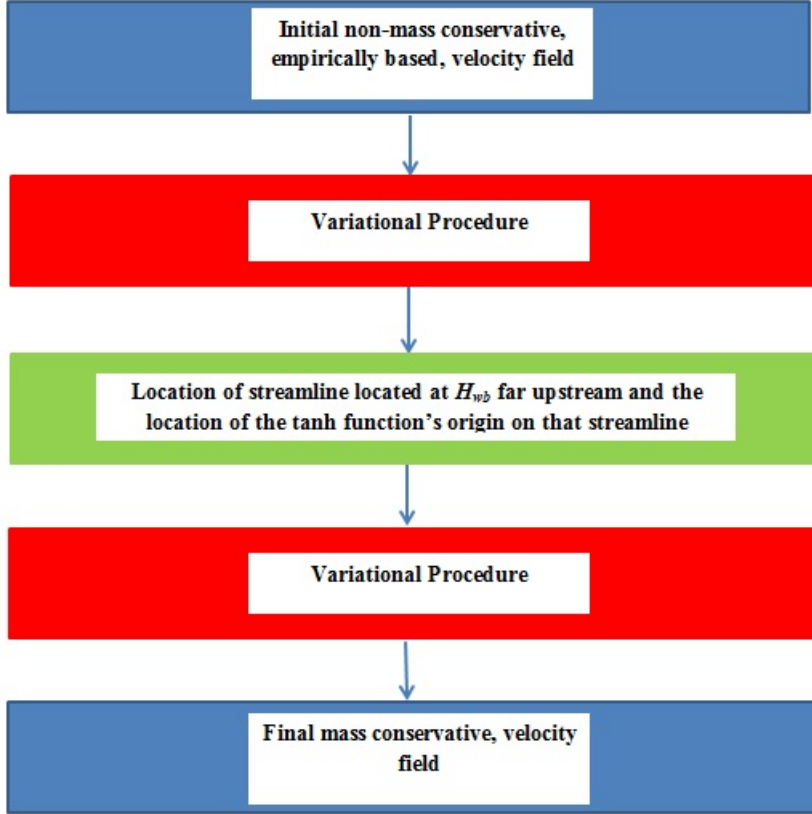
Figure 12: Flow chart of procedure utilized to simulate a windbreak velocity field. Note that the variational procedure is performed twice in QUIC.

Turbulent Field

Similarity solutions for windbreak turbulence have been explored by Judd et al. (1996) and Perera (1981). In the general form of these solutions, the mean turbulence quantities are normalized by a turbulent velocity scale, U_s. The vertical dimension is normalized by 2δ, the thickness of the shear zone downwind of the top of the windbreak, and the origin of vertical axis is translated from the ground to H. Mathematically this is expressed as:

$$\frac{\overline{u'w'}}{U_s^2} = f_{uw}(\xi) \qquad \frac{\overline{u'^2}}{U_s^2} = f_{uu}(\xi) \qquad \frac{\overline{w'^2}}{U_s^2} = f_{ww}(\xi) \tag{8}$$

where

$$\xi = (z - H)/2\delta. \tag{9}$$

Judd et al. (1996) took U_s^2 to be the magnitude of the maximum Reynolds stresses, $\overline{u'w'}$ at a given downwind distance of the windbreak. The resulting scaling is quite good and shown in Figure 13.
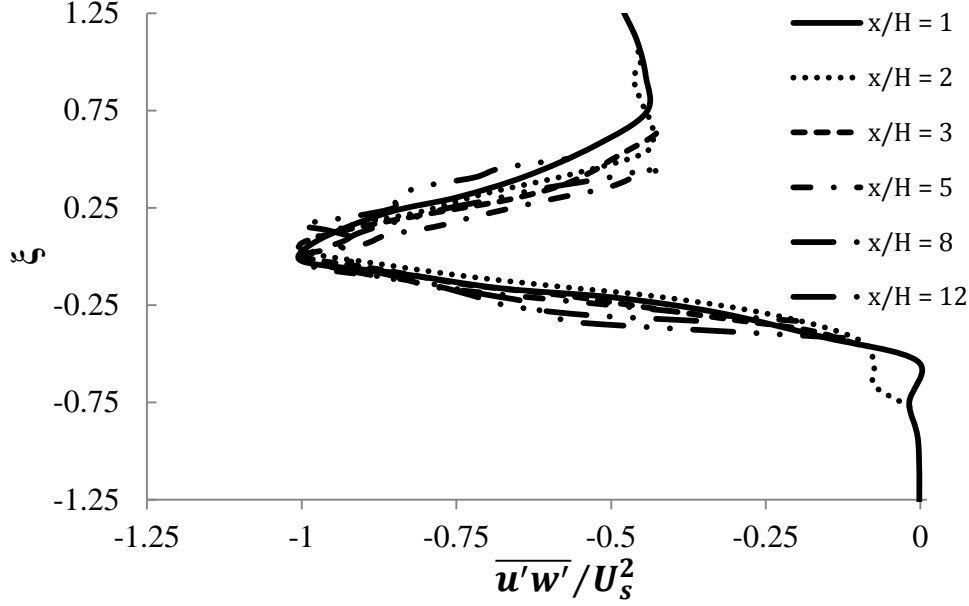
Figure 13: The turbulence similarity solution proposed by Judd et al. (1996).

There are three steps to parameterizing the turbulence similarity solution: 1) producing the mathematical description of the vertical profile given in Figure 13, 2) specifying U_s, the turbulent velocity scale, at all downwind locations and 3) relating all turbulent quantities, $\overline{u'^2}$ and $\overline{w'^2}$ to the Reynolds stresses, $\overline{u'w'}$.

For the first step, the functional description of the vertical dependence of $\overline{u'w'}/U_s^2$ on ξ was chosen to be:

$$f(\xi)_{uw} = A\tanh(\xi - c(A,B)) + B\cosh^{-2}(\xi - c(A,B)) + C. \tag{10}$$

Equation 10 includes *tanh,* used in the windbreak mean velocity profile, and its first derivative, *cosh*$^{-2}$. The constant *c(A,B)* ensures the maximum of Eq. 10 occurs at ξ =0. Its value, *c(A,B)* *=atanh(A/(2B)),* may be found by equating the vertical derivative of Eq. 10 to zero. The parameters *A*, *B*, and *C* subject the Eq. 10 profile to three constraints.

$$A\tanh(\infty) + B\cosh^{-2}(\infty) + C = \overline{u'w'}_{upstream} \quad (\xi \to \infty) \tag{11}$$

$$A\tanh(-\infty) + B\cosh^{-2}(-\infty) + C = \overline{u'w'}_{min} \quad (\xi \to -\infty) \tag{12}$$

$$A\tanh(c(A,B)) + B\cosh^{-2}(c(A,B)) + C = U_s^2 \quad (\xi = 0) \tag{13}$$

Where $\overline{u'w'}_{upstream}$ is the upstream surface layer value of $\overline{u'w'}$ and $\overline{u'w'}_{min}$ is the Reynolds shear stress in the bleed flow. It is assumed: $\overline{u'w'}_{min} = \alpha^2_{bleed\ flow} * \overline{u'w'}_{upstream}$. Also Eq. 10 assumes that $\overline{u'w'}$ is a small non-zero value at the ground instead of its true value, zero. The consequences of this discrepancy are negligible for the resolution of data examined in this work. Using the relations *tanh(c(A,B)) = A/(2B), 1-tanh*^{2}*=cosh*$^{-2}$ and *c(A,B) > 0* together with the limits,

$cosh^{-2}(\infty) \rightarrow 0$, $cosh^{-2}(-\infty) \rightarrow 0$, $tanh(\infty) \rightarrow 1$, $tanh(-\infty) \rightarrow -1$ yield the values for the constants which are: $A = (1 - \overline{u'w'}_{min})/2$; $C = (1 + \overline{u'w'}_{min})/2$; $B = ((-C + U_s) + ((C - U_s)^2 - A^2)^{0.5})/2$.

For the second step, parameterizing U_s, the turbulent velocity scale, at all downwind locations, x/H, we hypothesize that there is a similarity solution $U_s^* = f(x^*)$. A model of this solution is shown in Figure 14. U_s^* and x^* are similarity parameters that account for variation of windbreak aerodynamic porosity α_{obf}, and windbreak height compared to upstream roughness $(H-d)/z_o$. U_s^* is the difference of U_s and its undisturbed upstream value, $\overline{u'w'}_{upstream}^{0.5}$, normalized by the difference of $U_{s\,max}$ (the maximum value of U_s located in the high shear zone just downwind of the windbreak top) and $\overline{u'w'}_{upstream}^{0.5}$. We can then write this normalized scaling velocity as:

$$U_s^* = \frac{U_s - \overline{u'w'}_{upstream}^{0.5}}{U_{s\,max} - \overline{u'w'}_{upstream}^{0.5}},$$

and the normalized downwind distance, x^* as:

$$x^* = \left(D\alpha_{obf}^{2.5}(z_o/(H-d))^{.75} + E\right) * (x/H - Fln((H-d)/z_o) + G).$$

The variables: D, E, F, and G are coefficients to be determined by a least squares fit to data.

This parameterization is based upon the data sets of: Perera (1981), Bradley and Mulhearn (1983), and Judd et al. (1996) all which have 1) of the relatively high spatial resolution of turbulence measurements, 2) the span in range of windbreak heights normalized by upwind roughness $(H-d)/z_o = 30$ to $(H-d)/z_o = 600$ 3) and 3) the large range of optical porosities $\beta=0$ to $\beta=0.7$. Similar relationships have been developed previously (Perera 1981) but are valid only at distances far downstream of windbreaks, $x/H>7.5$ and are validated with a single dataset instead of multiple data sets as is done in this work. The result of the least squares fit of x^* and U_s^* is shown in Fig.15.
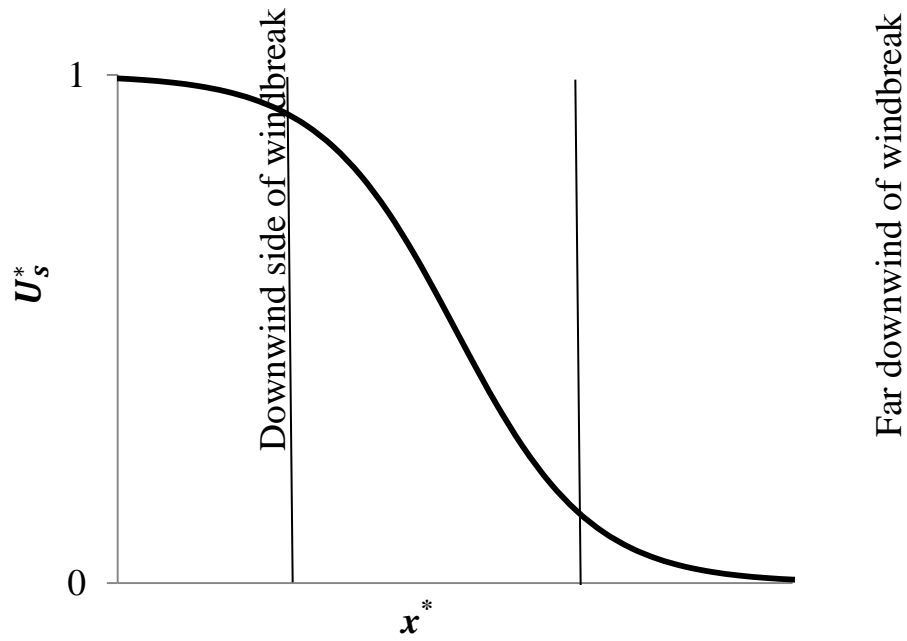
Figure 14: The variables x^* and U_s^* illustrating the recovery of U_s, the turbulent velocity scale, from its maximum value, $U_{s\,max}$, (occurring on the downwind side of the windbreak on the left) to its upstream value, $\overline{u'w'}^{0.5}_{upstream}$ far downwind on the right. The recovery is divided into three regimes: the first regime exhibits asymptotic decay from $U_s^* = 1$, the second exhibits rapid decay of U_s^*, and the final exhibits U_s^* approaching 0 asymptotically.

1.2

U_s^*

1

0.8

0.6

0.4

0.2

0

◆ Judd Shd (β=0.3)

⊿ Judd Smd (β=0.43)

+ Bradley β=0.5

○ Perera β=0.0

——-0.5*tanh+0.5

-3   -2   -1   0   1   2   3

x^*
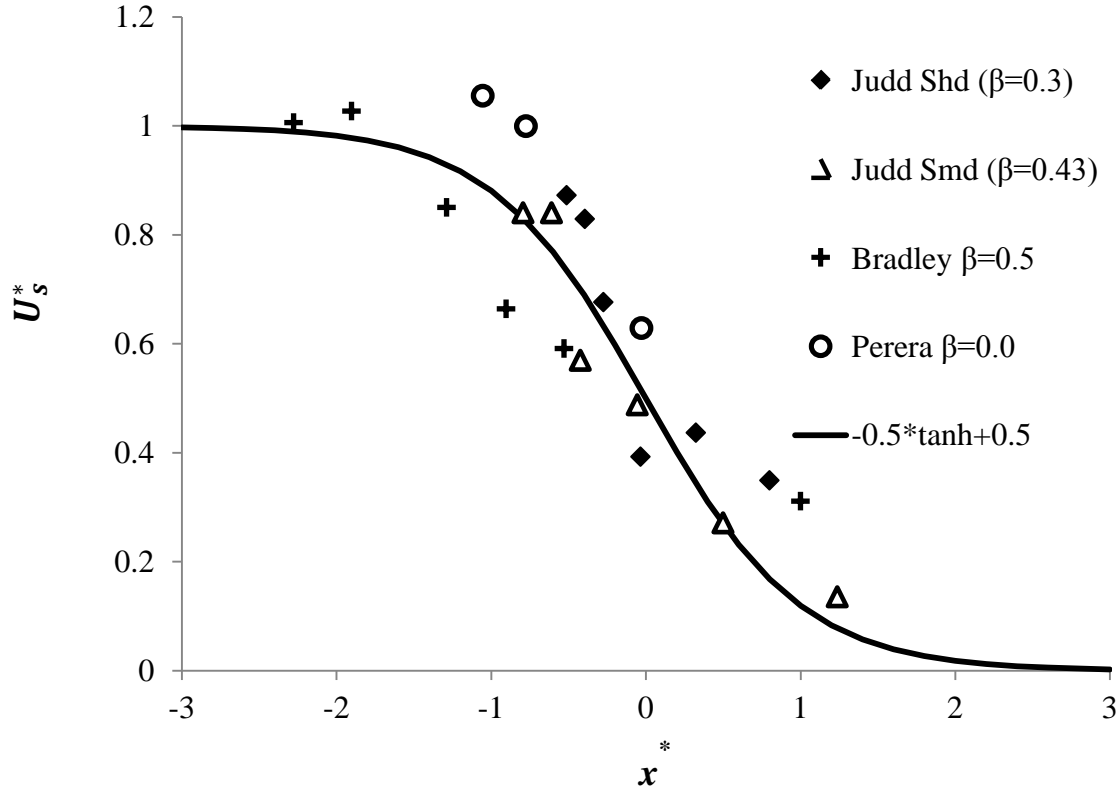
Figure 15: The calculation of the turbulent velocity scale, U_s, utilizing two dimensionless parameters: U_s^* and x^*. $x^* = \left(11.6\alpha_{obf}^{2.5}(z_o/(H-d))^{.75} + 0.074\right) * (x/H - 7.9 ln((H-d)/z_o) + 21)$ and $U_s^* = (U_s/\overline{u'w'}_{upstream}^{-0.5} - 1)/(0.22\,ln((1-\alpha_{obf})^2 * z_o/(H-d)) - 0.13)$, where α_{obf} is the aerodynamic porosity of the bleed flow through the windbreak. The coefficients are obtained from least square fits to data from Judd et al. (1996), Bradley and Mulhearn (1983), and Perrera (1981). U_s^* and x^* are related by: $U_s^* = -0.5 * \tanh(x^*) + 0.5$.

Once U_s has been parameterized, the mathematical description of $\overline{u'w'}$ is complete and the remaining elements of the Reynolds stress tensor, $\overline{u'^2}$ and $\overline{w'^2}$, can also be parameterized. The following relations are used by Counihan et al. (1974) for this purpose and are valid for the surface layer:

$$\overline{u'^2} = 5.0\overline{u'w'}, \tag{14}$$
$$\overline{w'^2} = 1.5\overline{u'w'}. \tag{15}$$

3.2.2. Improved Deposition Modeling
The wind tunnel research outlined in this report was designed to help develop a model for particle deposition with improved physics compared to current models. While the model form is presented here, the basis for the model is described in Section 3.1.1 in the results section of the wind tunnel testing. This section now details the method of incorporating the resulting model into QUIC.

Particle deposition is often quantified by the deposition velocity; V_d. A model for V_d that is commonly utilized is that of Raupach et al. (2001). In this model, a particle of a given diameter, d_p and traveling at a velocity of U interacts with a vegetative element of size d_e. Vegetative orientation is neglected. The Stokes number, Stk, for the particle element pair is calculated as:

$$Stk = (\rho_p d_p^2)/(18\rho_a v_a)[d_e/2U], \tag{16}$$

where ρ_p is the density of the particle (assumed 1000 kg/m^3), ρ_a is the density of the air, and v_a is the kinematic viscosity of the air. Once St is calculated, V_d can be calculated by

$$DF=(Stk/(St + p))^q \tag{17}$$

$$V_d = U \cdot DF, \tag{18}$$

where DF is the deposition fraction originally called deposition efficiency by Raupach et al. (2001), p and q are constants and Raupach et al. (2001) utilized 0.8 and 2 respectively. In a Lagrangian reference frame the concentration, C, decreases as:

$$dc/dt = -V_d \gamma C. \tag{19}$$

where γ is the vegetative surface density (vegetative surface area/unit volume of vegetation) his can be integrated along the particle path assuming V_d, , and U to be constant. This yields:

$$\sigma = C_1/C_o = \exp((-V_d \gamma S_b/U), \tag{20}$$

Where S_b is the distance traveled by the particle within the vegetative canopy during the time of integration and C_1 and C_o are the concentrations at the beginning and end of the period of integration respectively. The details of this model are presented in Amatul (2006).

An important deliverable from the wind-tunnel research was an improved parameterization for deposition fraction, DF, that accounts for deposition enhancement by turbulence (see results in section 3.1). DF is a function of the turbulence and the Taylor micro-scale (λ), which is an important parameter for quantifying the turbulence occurring within vegetation. It is very difficult to directly compute a general Taylor micro-scale. However, if one assumes that the turbulence is locally isotropic, following Tennekes and Lumley (1972) λ can be calculated within QUIC's existing turbulence framework via the following relationship:

$$\lambda = \left(\frac{\varepsilon}{15 v_a u_i^2}\right)^{\frac{1}{2}}. \tag{21}$$

In Eq. 21, ε is the dissipation rate of turbulent kinetic energy and u_i^2 is the squared local turbulence intensity.

The final step is to use the wind-tunnel developed expression (Eq. 47) for DF instead of the traditional Eq. 17. This is described below.

3.3. Full-scale Deposition Field Experiments

To better understand transport and deposition in vegetative canopies and windbreak two field experiments were conducted. The first was at Hanford, Washington (WA). This site featured native vegetation in form of a canopy. The second utilized the Raft River Windbreak near Malta, Idaho (ID). Both experiments included high-resolution measurements of the flow field as well as concentrations fields of particulate matter.

3.3.1. Hanford, Washington Semi-arid Vegetation Experiment

A field study was performed at the Pacific Northwest National Laboratories Hanford site (46°34'3.53"N and 119°36'5.44"W, ~220 m above sea level). The dates of the campaign were from June 6 to June 13, 2011. During the field campaign, two Intensive Observation Periods (IOPs) were conducted with simulated road traffic. Table 2 summarizes the IOPs. The study was conducted in conjunction with J. Gillies and V. Etyemezian's group from the Desert Research Institute (RC-1729). The region around the measurement site contained native vegetation in all directions of about 1.4 m in height. The road was oriented due east-west and was unpaved.

The two objectives for the field study were:
1) Objective 1: To verify the ability of QUIC to estimate PM_{10} transport and deposition within a vegetative canopy typical of many military facilities. The QUIC simulation was performed in real time during an IOP on June 7, 2013 where the aerosol sensors were located based on the results of the QUIC simulation of the PM_{10} dispersion and removal at the site in real-time. This represented a demonstration of the prototype field model for planning and prediction.
2) Objective 2: To better understand the behavior with PM_{10} within vegetative canopies.

Fugitive dust was generated by vehicular traffic, a large van or truck, making discrete separate trips on the unpaved road. In between trips, time was allowed to pass so the dust cloud resulting from one trip could clear all the equipment before the cloud resulting from the next trip entered the equipment array.

Supporting Activities
To relate the fugitive emissions to models and other field studies, a number of site dependent measurements were necessary. These included site-specific vegetative measurements and meteorology measurements. The methodology utilized to document the roughness and meteorology conditions, are now presented.

IOP	Purpose	IOP Date/ Time	Atmospheric Conditions $z_{ref} = 3.9$ m

1	Use QUIC to design field study and make real-time sensor position adaption	June 7, 2011/12:50 to 14:50 Pacific Daylight Savings time (PDT).	u_{ref} = 5.4 m s^{-1} L= -47.4 m u_* = 0.61 m s^{-1} tke = 0.4 m^2 s^{-2} z_o = 0.07 m
2	Validate QUIC with high resolution canopy PM$_{10}$ profile	June 13, 2011/ 16:30 to 17:30 PDT.	u_{ref} = 6.8 m s^{-1} L= -117 m u_* = 0.71 m s^{-1} tke = 0.3 m^2 s^{-2} z_o = 0.07 m

Table 2: Summary IOP table for the Handford, WA experiment. Averages were taken over the IOP duration.

Meteorology

For the field study, it was important to carefully characterize the basic transport mechanisms, in particular: horizontal advection and vertical transport. To characterize these processes meteorological data were taken within and above the vegetative canopy at one tower using four Campbell Scientific 3D anemometers (CSTA3). The 3D sonic anemometers measured the three velocity components and virtual temperature at a rate of 10 Hz. A Campbell Scientific CR5000 data logger was utilized to record and process the data. In order to ensure reliability of the measurements, all of the anemometers and data loggers were within the recommended manufacture's calibration period. The tower location and anemometer heights are noted in Table 3. The anemometers are shown in Figure 16. The location of the sonic anemometers, 37 m downwind of the road, was chosen to allow the airflow to recover from the transition of the exposed ground, characteristic of the road, to the vegetation, which was about 1.4 m in height. The data utilized in making this choice are found in Arya (2001).

The sonic anemometers make possible a characterization of the transport mechanisms within and above the vegetation. Parameters needed to perform QUIC simulations were calculated from the sonic anemometer data in real time during the experiment. This enabled fast computer simulations to optimize sensor placement for IOPs involving *Objective 1*.

Equipment (Number of Sensors)	Downwind Distance (m)	Sensor Heights (m)

| 3D Sonic Anemometers (4) | 37.0 | 0.68, 1.40, 2.00, 3.90 |

Table 3: Location of anemometers that characterized meteorological conditions during the Handford WA field study.

Figure 16: Photo of the 3D Sonic Anemometer Tower at the Hanford field study site.

Site Vegetation

The density of vegetation was characterized using the Leaf Area Index (LAI). LAI is the ratio of plant surface area to ground surface area and is dimensionless (Bréda, 2003). The current project utilized two methods for estimating LAI at the field site. The first was remote sensing based, utilizing the United States Geological Survey (USGS) MODIS database. This is located online at the URL of: http://daac.ornl.gov/cgibin/MODIS/GLBVIZ_1_Glb/modis_subset_order_global_col5.pl. (Last accessed in 2011) The second method was an indirect optical method to determine LAI using a Licor LAI-2000®.

In-field calibration of the LAI-2000 included a diffuse shortwave radiation measurement to be made at sunrise, sunset, or on a cloudy day. The vertical profile of LAI was measured at multiple locations. This was performed by dividing the height of the vegetation canopy into four approximately equal vertical intervals defined by the points: $0H_c$, $0.25H_c$, $0.5H_c$, $0.75H_c$. An advantage of these onsite measurements was that the distribution of LAI, or vegetative density with height could be determined. Using the MODIS satellite imagery database method, the distribution with height was unknown. The variation of LAI with height may be important for simulation purposes. These LAI profile measurements were performed at locations along the x-axis in Figure 19 in 2 m intervals from the roadside to the distance of the farthest downwind measurement (~60 m downwind of the road). Also, a number of measurements were performed parallel to the road direction at 37 m downwind of the road the location to ensure that the LAI calculations include vegetation that may have influenced fugitive dust emissions if the wind was not perfectly perpendicular to the road direction. In total, 48 measurements were made. The total distance from the sonic tower the measurements covered was dictated by the experimental results of Cheng-I et al. (2000). This distance included all the vegetation that influenced the sonic measurements.

Fugitive Dust Concentration Measurements
Measurements of dust concentrations were made using TSI DustTrak® 8520 Aerosol Particulate Monitor optical sensing devices sampling at 1 Hz. The DustTrak is a rugged portable device that uses light scattering of dust to measure concentrations. It is capable of measuring concentrations ranging from 0.001 to 100 mg/m^3 and has been utilized in previous studies of road dust emissions (Veranth et al., 2003). PM$_{10}$, inlets were utilized in this experiment. The DustTrak sensors were rented from Galson Labs (http://galsonlabs.com/) and Argus-Hazco (http://argus-hazco.com/). The companies calibrate the instruments prior to shipment. The standard calibration procedure used to calibrate the instruments is found in the TSI 8520 DustTrak Manual. Further, colocation tests were performed. The data from are shown in Appendix A. Typical inter-instrument variability characterized by the standard deviation of mean concentration measurements was 0.06 mg/m^3 compared to typical maximum concentrations of 40 mg/m^3.

Objective 1
As previously noted, QUIC was previously capable of modeling the dispersion of PM$_{10}$ that occurs in vegetative canopies and has a model for vegetative deposition (Amatul 2006). The dispersion parameterizations are an enhancement of the work of Cionco (1965) and utilize his

vertical velocity profile for the removal of momentum from the wind field. This new vertical profile is used in conjunction with a mixing length turbulence model to estimate dispersion.

In field studies, the dispersion of PM_{10} was measured utilizing a flux methodology. Horizontal fluxes of the PM_{10} component of fugitive dust, denoted by F, are common in estimating the transport of fugitive dust (Veranth et. al 2003; Etyemezian et al. 2004; Speckart et al. 2013). Differences in F at two points are equal to the removal of the PM_{10} between the two points. F is the integrated product of the local concentration and horizontal wind speed. The integration is performed from the ground to the cloud top, and then summed over the time of travel for the plume to travel past the downwind PM_{10} sensors. Both wind speed and concentration have been measured experimentally during all the IOPs for this current work. Owing to the discrete nature of the measurements in section field studies, modeling assumptions are needed to estimate fluxes. This project utilizes the method proposed by Speckart et al. (2013) (This method is described later in this section.) All of the methods yield the same result when a sufficiently large number of sensors are utilized. When fewer sensors are used, the proposed method is more robust than previously utilized methods.

In the absence of sources, the horizontal flux will be a non-increasing function with increasing downwind distance from a road. Mechanisms such as vegetative deposition and gravitational settling can remove fugitive dust and consequently, reduce horizontal fluxes. This reduction can be modeled in QUIC as illustrated in Figure 17.
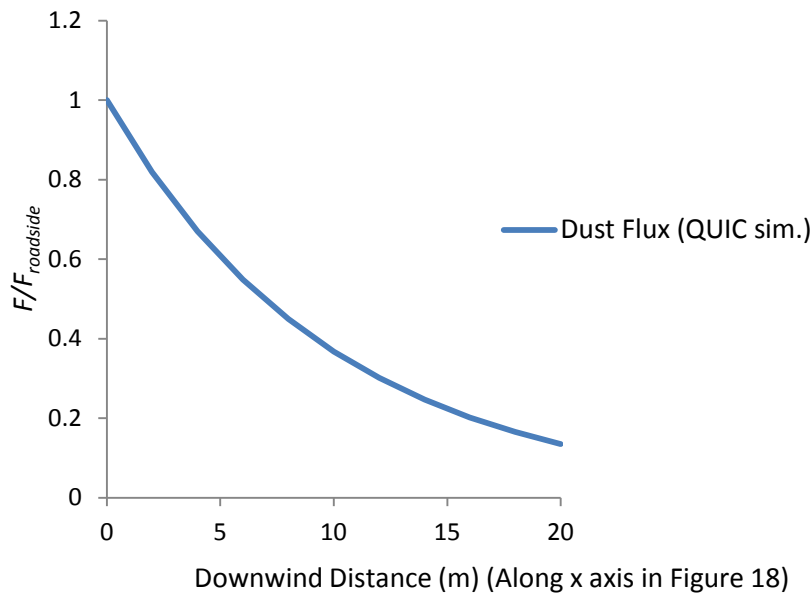
Figure 17: Illustration of a QUIC Dispersion model simulation of the reduction of roadside horizontal flux $F/F_{roadside}$ for the Hanford experiment.

To facilitate field and simulation comparison, the horizontal flux is generally normalized by the roadside flux, $F_{roadside}$. As one may deduce from Figure 17, the majority of the removal occurs near the road where the majority of the dust cloud interacts with vegetation and the ground. As downwind distance increases, the removal mechanisms become less important and the flux

becomes nearly constant at a value denoted as F_{min}. Owing to this behavior, a new quantity, the fraction removal, *Frac*, can be defined as:

$$Frac(x) = \frac{F(x) - F_{min}}{F_{roadside} - F_{min}}.$$

(22)

Frac has a maximum of 1 at the roadside and a minimum of 0 far downwind from the road. The behavior of this fraction of removal is illustrated in Figure 18. *Frac* may be physically interpreted as the remaining fraction of removal that will occur as one travels downwind. At the roadside, all removal mechanisms are located downwind, hence *Frac*=1. At a position where *Frac*=0.5, half of the removal is located upwind and half is located downwind, and when *Frac*=0, all of the removal mechanisms are located upwind.
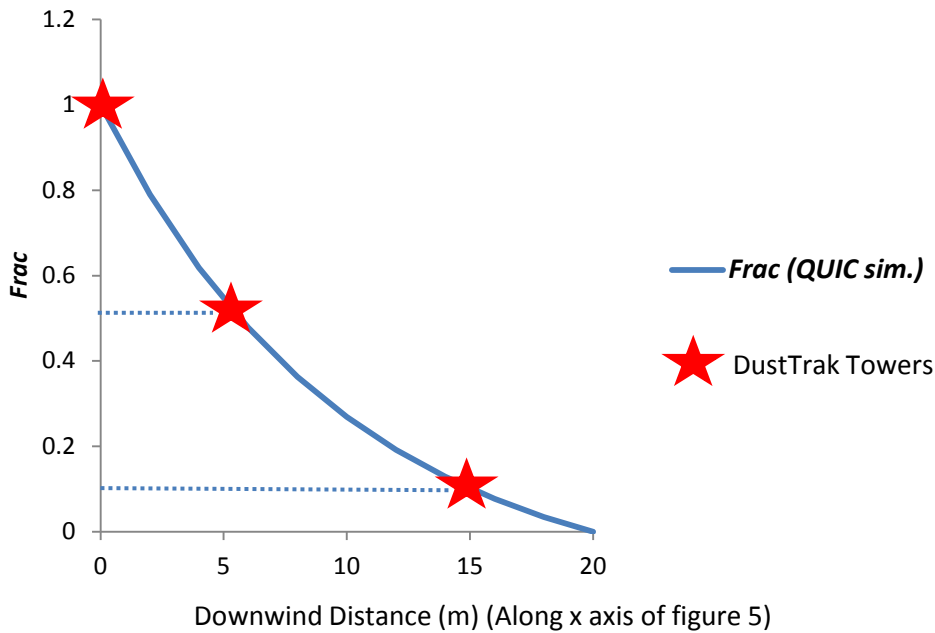
Figure 18: Reduction in normalized dust concentration (*Frac*) with increasing downwind distance from a QUIC simulation. DustTrak tower locations for the Hanford experiment were determined in *real-time* using the *Frac* curve as predicted by the QUIC. Values of 1, 0.5, 0.1, were chosen for comparison between QUIC simulation and the field study. These values indicate the fraction of the total removal that is predicted to occur as the cloud advects further downwind. The total removal may be significant or insignificant, *Frac*, indicates the distribution of the total removal with downwind distance.

The placement of the three DustTrak towers during the experiment was determined using QUIC simulations such that the first tower was placed roadside where *Frac* = 1, the second tower where *Frac*=0.50, and the third tower was located where *Frac* = 0.10. The experimental set-up is summarized in Figure 19. The physical locations for the placement of the sensors during the IOPs is shown in Table 4 along with the date, number of runs, and atmospheric stability.
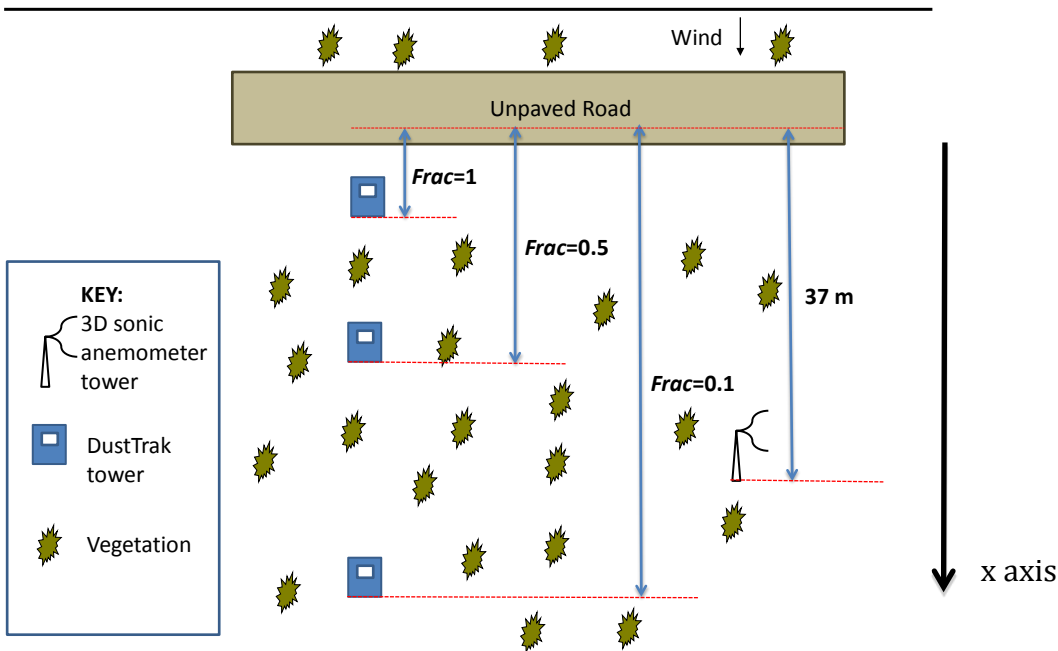
Figure 19: Schematic of equipment deployment for Objective 1 IOPs. The DustTrak towers are dimensioned by the placement criteria, DustTrak towers located at the physical locations where F*rac* =1, 0.5, and 0.1 according to QUIC simulations.

IOP DATE	Atmospheric Stability	Number of Vehicle Runs	Downwind Distance (m) (Along x axis of Fig. 1) of DustTrak monitor towers. All towers employ sensors at heights of 0.58, 1.20, 1.70 m.
June 7, 2011	Unstable	32	10.0, 16.4, 66.4

Table 4: The placement of DustTrak Sensors for objective 1 IOP during the Hanford canopy deposition study. Note that the downwind DustTrak tower location, right most column, moves according to QUIC simulation results.

QUIC dispersion and deposition simulations were run in order to field test the QUIC model and optimize field sensor locations using real time monitored variables from sonic anemometer. The needed data included: horizontal mean wind at the four heights, the friction velocity (u_*), the absolute near surface temperature T_o, the kinematic heat fluxes $Q_o = \overline{w'T_v'}$ (computed from the sonic temperature and vertical velocity correlation), the Monin-Obukhov length scale $L = u_*^3 / [\kappa Q_o (g/T_o)]$, vegetative height, and LAI. These meteorological variables are described in Arya (2001). With the experiment configuration utilized in Hanford, these variables were obtainable just before the first vehicle trip over the unpaved road. The meteorological data were based on 5 min averages.

To estimate the robustness of the QUIC simulation results, Eq. 22 can be solved for F_{min}. This yields:

$$F_{min} = \frac{FracF_{roadside} - F}{Frac - 1}.$$

(23)

An estimate for F_{min} was computed using the IOP data obtained from the second and third towers. Another estimate for F_{min} was obtained from the QUIC simulation of the IOP, with identical meteorological and roughness conditions. The estimated accuracy of the QUIC model increases as the difference of the two estimates for F_{min} decrease.

Objective 2
Past studies have focused on fugitive dust emissions by examining PM_{10} concentrations at all heights, from the ground to the cloud top (Veranth et al. 2003; Etyemezian et al. 2004; Speckart and Pardyjak 2011). As a consequence of limited resources, a limited number of sensors have been used to measure vertical profiles of PM_{10} concentrations within vegetative canopies. Models for fugitive dust concentrations resulting from emissions have been implemented above vegetative canopies with success, such as exponential and step profiles (Veranth et al. 2003) but may be inappropriate within the canopies. Issues such as the boundary condition for PM_{10} concentration at the ground are important for simulation but to-date are relatively poorly understood.

Concentrations within vegetative canopies are generally assumed to decrease with increasing height for near ground sources (Veranth et al. 2003). This is a common assumption in the calculation of F (e.g. Veranth et al. (2003)). This is the case despite that Lagrangian dispersion models that suggest otherwise (Aylor and Flesch 2001). Currently, there is a lack of high-resolution concentration data measured in the field (e.g. more than 3 points to estimate concentration profiles within canopies). Hence, we designed an experiment to measure the vertical profile of PM_{10} with a tower consisting of nine DustTrak monitors. Their heights and downwind distance are shown in Table 5.

Date	Number of Vehicle Runs	Downwind Distance (m)	Sensor Heights (m)
June 13, 2011	50	32	0.04, 0.28, 0.58, 0.71, 0.89, 1.17, 1.48, 1.78

Table 5: 3D Sonic and DustTrak Sensor placement for the canopy concentration, objective 2 IOP measured during 16:00 to 18:00 PDT and featuring unstable atmospheric conditions.

A photograph of the tower with DustTraks is shown in Figure 20. Utilizing the DustTrak concentration data, a detailed vertical concentration profile can be produced.

Figure 20: Photograph of DustTraks during the high-resolution vertical profile concentration, objective two IOP on June 13, 2012 at Handford, WA.

Method for Calculating Horizontal Flux, F for Handford, WA Field Study

PM$_{10}$ concentration and wind data can be used in multiple ways to calculate the horizontal flux. Horizontal flux at *x* was calculated as:

$$F_x = \int_{z=0}^{z=\infty} \int_{t=0}^{t=t_{max}} C(x,z,t)u(x,z,t)dtdz. \tag{24}$$

t$_{max}$ is the time for the plume to travel more than 100 m down wind. In the subsequent discussion, $\bar{c}_{int}(x,z) = \int_{t=0}^{t=t_{max}} C(x,z,t)dt$, and is utilized to apply a continuous dispersion, such as a Gaussian Plume model, to data obtained from discrete vehicle trips. The new method incorporates additional physics and complexity to substitute for large amounts of concentration data. In addition to wind and PM$_{10}$ concentration data, it requires an estimate of atmospheric stability through the Monin-Obukhov length scale, *L* (Ayra 2001). *L* can be calculated using eddy covariance methods (see section 2.3.1), profiles of mean velocity and temperature (Ayra, 2001) or the Pasquill stability chart (Seinfield and Pandis, 1998). For the work presented here, the eddy covariance method was used. The new method utilized the Gaussian-plume model proposed by Van Olden (1978):

$$\bar{c}_{int}(x,z)/Q = (A(x) \exp \left[(-B\,z/\bar{z}(x))^s\right]), \tag{25}$$

where *Q* is the source strength (kg m^{-1}), *A(x)* is a coefficient quantifying the downwind decrease of $\bar{c}_{int}(x,z)$, *s*, the shape factor, was a constant that varied from 1 to 2 (Venkatram 2004). If *s=1* the profile is exponential, if *s=2* the profile is Gaussian. Venkatram (2004) assumed *s=1.5* as suggested by Van Olden and this work utilized that assumption. *B* is a constant defined as:

$$B = \Gamma(2/s)/\Gamma(1/s), \tag{26}$$

where Γ was the gamma function.

The height, $\bar{z}(x)$, is the vertical center of mass of the PM_{10} plume. Its definition is:

$$\bar{z}(x) = \frac{\int_0^\infty z\bar{c}_{int}(x,z)dz}{\int_0^\infty \bar{c}_{int}(x,z)dz}. \tag{27}$$

Eq. 27 suggests that the vertical profile of $\ln(\bar{c}_{int}(x,z))$ and z^s is linear and consequently its characterization is simpler than the non-linear profile of $\bar{c}_{int}(x,z)$ and z. As a result, the new method estimates the profile of $\bar{c}_{int}(x,z)$ and z indirectly by first calculating the profile of $\ln(\bar{c}_{int}(x,z))$ and z^s and subsequently computing the profile of $\bar{c}_{int}(x,z)$ and z by taking exponentials and roots of the respective variables.

The new method divides the integrated concentration profile into three zones: 1) the zone below the lowest DustTrak 2) the zone between the lowest and highest DustTrak monitor 3) the zone above the highest DustTrak monitor. This is shown in Figure 21. For the lowest zone, $\ln(\bar{c}_{int}(x,z))$ is assumed to be constant from the ground to the bottom DustTrak monitor. For the intermediate zone, within the DustTrak monitors, $\ln(\bar{c}_{int}(x,z))$ is assumed to vary linearly as a function of z^s between adjacent DustTrak monitors. Above the topmost DustTrak monitor, $\ln(\bar{c}_{int})$ is assumed to decrease linearly with increasing z^s.

Linear decrease of $ln\ \bar{c}_{int}$ with increasing z^s above top DustTrak monitor as indicated by the Van Olden (1978) model.

Linear interpolation of $ln\ \bar{c}_{int}$ with z^s between adjacent DustTrak monitors.

Constant $ln\ \bar{c}_{int}$ below bottom DustTrak monitor.
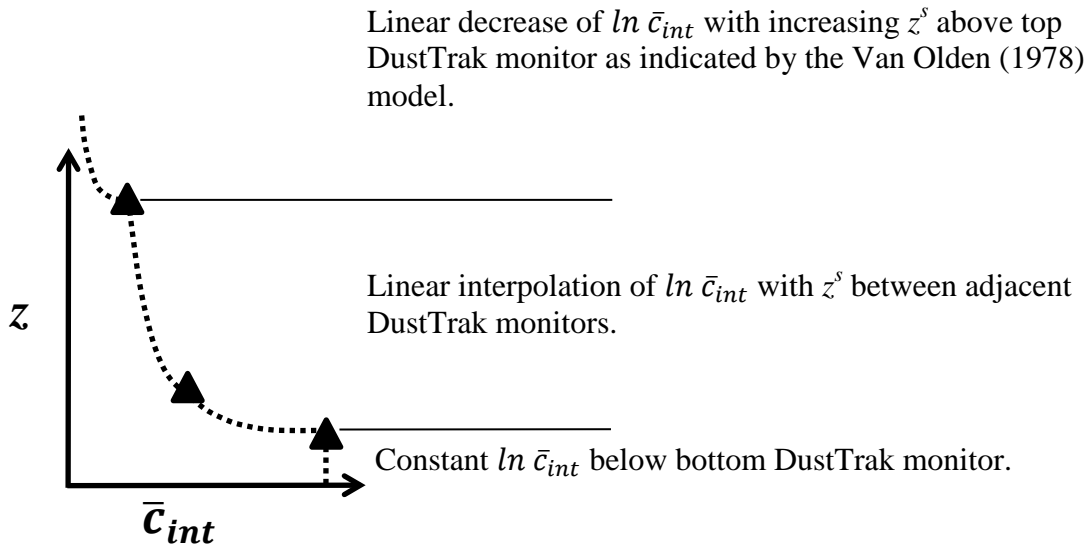
Figure 21: Conceptual illustration of the methodology used to calculate the horizontal flux, F from DustTrak data   . ▲

Above the top DustTrak monitor, we had to calculate the rate of decrease of $\ln(\bar{c}_{int})$ with increasing z^s (denoted as: $\partial \ln(\bar{c}_{int})/\partial z^s$). For a given downwind distance, $\partial \ln(\bar{c}_{int})/\partial z^s$ is a constant. In other words, the vertical decrease of $\ln(\bar{c}_{int})$ with increasing z^s is linear.

$\partial \ln(\bar{c}_{int})/\partial z^s$ can be calculated by taking logarithms and then derivatives of both sides of Eq. 25.

$$\partial \ln \bar{c}_{int}/\partial z^s = -\left[\frac{B}{\bar{z}(x)}\right]^s. \tag{28}$$

After deriving Eq. 28 it remained to calculate $\bar{z}(x)$. The downwind dependence of $\bar{z}(x)$ is modeled by the ordinary differential equation (ODE) (Venkatram 2004):

$$\frac{d\bar{z}}{dx} = K(q\bar{z})/(\bar{u}(q\bar{z})q\bar{z}), \tag{29}$$

where K was the vertical turbulent diffusion coefficient and q is defined by:

$$q = [s\{\Gamma(2/s)/\Gamma(1/s)\}^s]^{1/(1-s)}. \tag{30}$$

In Eq. 28, q was a constant that relates the vertical dispersion to distance traveled downwind. The initial condition assumed for Eq. 29 was $\bar{z}(0) = 1$ m. Vertical profiles for $K(q\bar{z})$ and $\bar{u}(q\bar{z})$ are needed as inputs for Eq. 29. Venkatram (2004) inserted, $K(qz) = \kappa u_* qz$, for a neutral surface layer and a power law wind profile for $\bar{u}(z)$ yielding:

$$\bar{z} = (1/q)\left[(p+1)\kappa q \frac{u_*}{\bar{u}_r} xz_r^p\right]^{1/(p+1)}. \tag{31}$$

This was extended to stable atmospheric conditions using, $K(qz) = (\kappa u_* qz)/(1 + 4.7(q\,z/L))$:

$$\frac{\bar{z}^{p+1}}{p+1} + \frac{4.7\,q\bar{z}^{p+2}}{(p+2)L} = \frac{\kappa u_* z_r^p}{u_r q^p}x. \tag{32}$$

Eq. 32 can be solved by a simple bisection root finding technique (Chapra and Canale, 2006). For unstable conditions, $K(qz) = (\kappa u_* qz)/(1 - 15(q\,z/L))^{1/4}$, would have yielded:

$$\frac{\partial \bar{z}}{\partial x} = \frac{\kappa u_* z_r^p}{u_r q^p}\left(1 - 15(qz/L)\right)^{1/4}. \tag{33}$$

Eq. 32 can be solved with a typical integration technique such as a fourth order Runge-Kutta method (Chapra and Canale, 2006).

The vertical profiles of $\bar{c}_{int}(z)$ were obtained by taking the exponent of $ln(\bar{c}_{int}(z))$ and the root of z^s .

3.3.2. Raft River Windbreak Experiment - Malta, Idaho

To validate the new models implemented in QUIC a field study was performed during July of 2012 at the Brigham Young University Skaggs Research Ranch, Cassia County, Idaho located in the Raft River valley of southern Idaho (42°30'05.28" N 113°24'29.92" W) near Malta ID. This site was selected because in 1994 the United States Department of Agriculture (USDA) Soil Conservation Service, Brigham Young University, and the Idaho Department of Transportation partnered together to plant several sections of living snow fences near the intersection of Idaho Hwy 81 and US Interstate 84 to mitigate the effects of dust storms in the summer and snow drifts in the winter on the nearby highways. The windbreaks are composed of two sections of two rows each of Rocky Mountain Juniper (*Juniperus scopulorum*) and Siberian Pea (*Caragana arborescens*). Supported by irrigation, the living snow fences have grown to ~4.0 m in height as shown in Figure 23.

The same types of instruments were from measuring wind speed and PM_{10} as described above for Handford. Again, all CSAT3 anemometers were within the manufacturers recommend calibration period. The DustTrak sensors were rented from Galson Labs (http://galsonlabs.com/) and Argus-Hazco (http://argus-hazco.com/). The companies calibrate the instruments prior to shipment. The standard calibration procedure used to calibrate the instruments is found in the TSI 8520 DustTrak Manual. Further, colocation tests were performed. The data from are shown in Appendix A. Typical inter-instrument variability characterized by the standard deviation of mean concentration measurements was 0.06 mg/m^3 compared to typical maximum concentrations of 40 mg/m^3. Wind data were taken from 21:15 to 22:30 MDT during the evening of July 12, 2012. Due to equipment malfunction, PM_{10} data was not collected during this period and only turbulence data were recorded. PM_{10} data were taken on July 27, 2012 from 12:00 to 17:00 MDT.

To measure the mean wind and turbulence field upstream, within, and downstream of the windbreak, five towers were erected with Campbell Scientific CSAT3 sonic anemometers (Campbell Scientific, Logan, Utah). Tower A was placed *25* m upstream to measure free-stream turbulence and Tower C was placed in between the two windbreaks to measure this sheltered area. Towers D, E, and F were placed successively downwind of the windbreak to measure the start of flow recovery to upstream conditions. Table 6 gives specific coordinates for each sonic anemometer, DustTrak and windbreak. Tower B had no 3D sonic anemometers.

PM_{10} data were taken on all towers except tower F. Locations are documented in Figure 22 and Table 6. The objective in choosing the sensor locations was to characterize as much as possible the approach flow, shelter zone, displaced flow, and recovery zones that are noted in Figure 8. Both fields provide verification to the flow models developed and implemented in QUIC for this project.
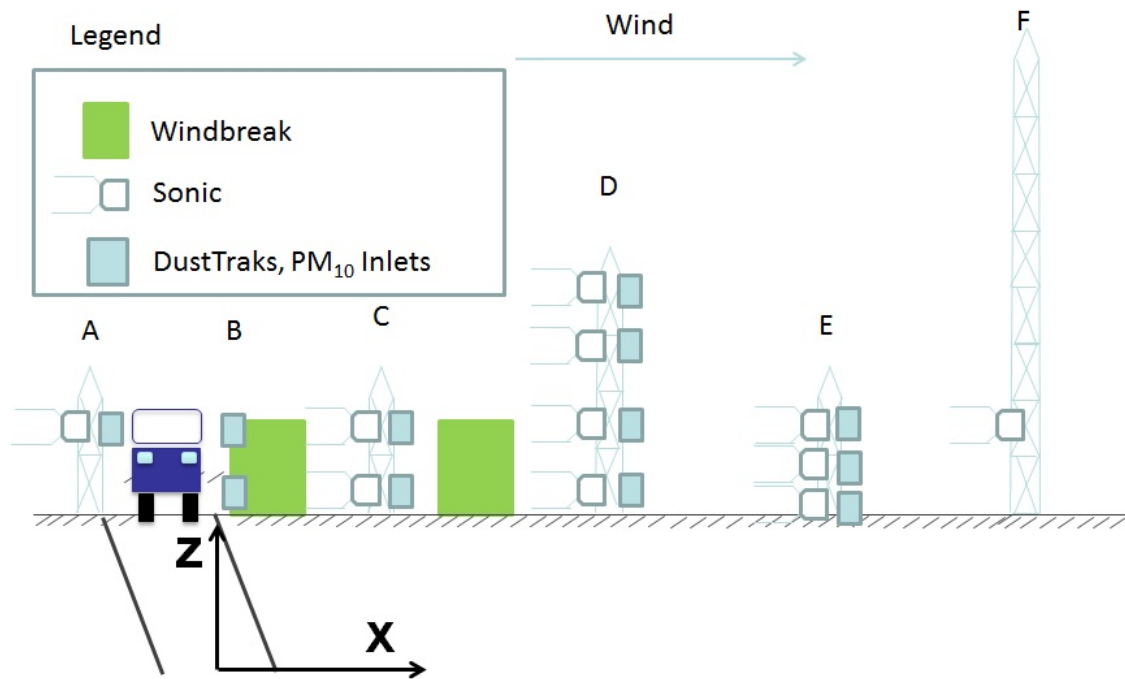
Figure 22: The configuration of 3D sonic anemometers (Sonic) and DustTraks for the Malta, ID Raft River Windbreak field study.

Tower A (-34.1 m)	Heights
Sonic	3.25 m
DT	3.15 m
Tower B (1 m)	**Heights**
DT	0.78 m
DT	1.39 m
Tower C (13.8 m)	**Heights**
DT	0.8 m
Sonic	1.03 m
DT	3.21 m
Sonic	3.31 m
Tower D (27.8 m)	**Heights**
DT	1.1 m
Sonic	1.25 m
DT	3.1 m
Sonic	3.25 m
DT	5.5 m
Sonic	5.6 m
DT	8.55 m
Sonic	8.7 m
Tower E (41.1 m)	**Heights**
DT	1.17 m
Sonic	1.09 m
DT	3.08 m
Sonic	3.28 m
Tower F (55.4 m)	Heights
Sonic	3.25 m

Table 6: Location of equipment deployed for the Raft River Windbreak field study. Experiment schematic shown in Figure 22.

Figure 23: Photos of the Raft River Windbreak at the field site near Malta ID: (left) upstream side with unpaved road shown and (right) downstream side of the windbreak.

3.4. Development of Simple Empirical Formula for Native Vegetative Removal

Prior to the start of this project, Pace (2005) developed the simple conceptual model of the removal of dust by vegetation shown in Figure 24. This qualitative model indicates that increases in native vegetative height and thickness increase PM_{10} removal. In this model captured fraction and transmitted fractions, (*CF* and *TF* respectively *TF* = (1-*CF*)) of vehicle generated PM_{10} traveling from the road to 100 m downwind depends upon native vegetative height and thickness. *CF* increases with increasing height and density of downwind vegetation. In this section, we present a simple model using our simulation and field results that provides quantitative estimates consistent with Fig. 24, and can be easily used for planning purposes.
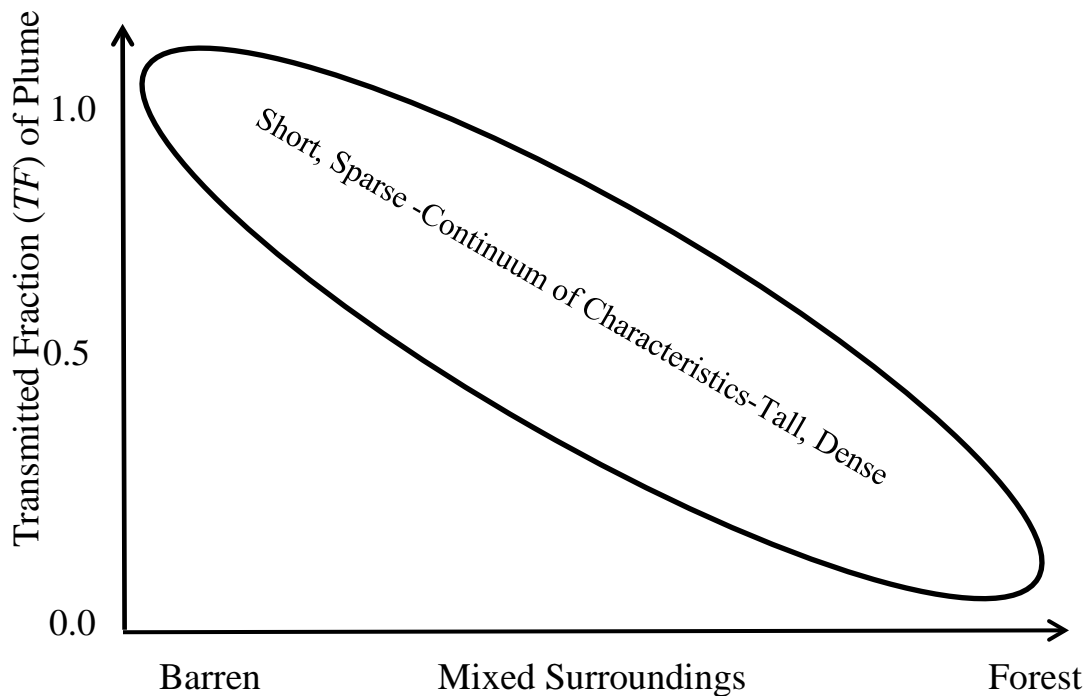
Figure 24: Recapitulation of the conceptual model of Pace (2005) that indicates that the transmitted fraction of a vehicle-generated plume is a function of the height and density of downwind roughness elements.

We utilized a simple canopy model for the native vegetation in which the canopy height is horizontally homogeneous, and vegetative density is assumed constant with height. For such a canopy *TF* and *CF,* can be calculated by the following simple equation:

$$TF = (1 - CF) = IF * (1 - \text{canopy removal efficiency}) + (1 - IF) \qquad (34)$$

Where, *IF* is the fraction of the initial dust cloud that interacts with the canopy (the interactive fraction) and the canopy removal efficiency defined as the fraction of *IF* that is removed by the canopy. The first term on the far right hand side (RHS) is the fraction of the initial plume that interacts with the canopy and is subject to removal and the second term on the RHS indicates the fraction of the initial plume that is not influenced by the canopy. As the canopy height is increased a larger and larger fraction of the roadside plume interacts with the canopy, i.e. the first term on the RHS increases. As the canopy becomes denser, the canopy removal efficiency generally becomes higher.

To quantify Eq. 34, two canopy parameters, *H** and *T**, were introduced in Pardyjak et al. (2008) that govern transmitted fraction in a canopy:

$$H^* = \frac{H_c}{H_{dc}} \qquad\qquad (35)$$

and

$$T^* = \alpha V_d H_{can}^2 \Big/ K(H_c) = \tau_t / \tau_d. \qquad\qquad (36)$$

In Eqs. 35 and 36, H_c is the height of the canopy and H_{dc} is the initial height of the dust cloud at the roadside, assumed to be 2 m in this work. A height of 2 m was selected as the typical height of an initial vehicle plume based on the previous work of Veranth et al. (2003). The sensitivity of the deposition results on the choice of H^* is shown in Fig. 7 in Pardyjak et al. (2008). For H* values less than about 4, the results are quite sensitive to this choice, however the simple model described here allows one to determine a range of potential deposition values (based on a range of H* values) quickly and easily. $K(H_c)$ is the vertical turbulent diffusivity at the top of the canopy and is a function of atmospheric stability; α is the vegetative surface area per unit volume, τ_t and τ_d are the time scales of vertical turbulent diffusion and of particle deposition respectively. *H** determines *IF* and T^* determines the canopy removal efficiency. Here, we propose to parameterize *IF* as a function of H^*

$$IF = 1 - \exp(-bH^*), \qquad\qquad (37)$$

where *b* is a positive constant. It is assumed that the vegetative canopy is located at the roadside close to the initial plume because the greatest particle filtering should occur with this configuration. As the distance is increased between the road and vegetation, the plume can mix vertically and the effective height of the plume compared to the height of the vegetation will increase. A discussion of the importance of the distance from the roadside to the vegetation can be found in Pardyjak et al. (2008) and Mao et al. (2013). The form of Eq. 37 was chosen considering the simulation results of Pardyjak et al. (2008). Pardyjak et al. (2008) also indicates that the canopy removal efficiency approaches 1 as T^* becomes large. For these conditions Eq. 37 reduces to *TF =(1-IF)*. Substituting *TF* = exp(-bH^*) into the equation and solving for *IF* yields Eq. 37.

The canopy removal efficiency depends upon T^*. To calculate T^* parameterizations for α, $K_{zz}(H_{can})$, and V_d are needed. γ=LAI/H_{can} where LAI is the leaf area index and is physically

interpreted as the vegetative surface area per ground area. For many locations, LAI can be obtained from the MODIS satellite database: (http://daac.ornl.gov/cgibin/MODIS/GLBVIZ_1_Glb/modis_subset_order_global_col5.pl last accessed March 2013) or it can be calculated from the aerodynamic roughness according to Eq. 4.6 (Choudhury and Monteith 1988)

$$LAI = (z_o/(0.28H_c))^2/0.2. \qquad (38)$$

In Eq. 38, the roughness due to larger scale surface irregularities, such as sand dunes, is assumed to have negligible effect upon z_o compared to the vegetation. To calculate $K_{zz}(H_{can})$ surface layer similarity is assumed, namely,

$$K_{zz}(H_c) = \kappa u_*(H_c - d)/\phi((H_c - d)/L), \qquad (39)$$

where κ is the von Karman constant $=0.4$, L is the Monin-Obukhov length scale defined as $L = u_*^3/[\kappa Q_o(g/T_o)]$. T_o and Q_o are the absolute surface temperature and kinematic heat fluxes respectively, u_* (the friction velocity) is the turbulent velocity scale, and $\phi(H-d)/L$ is the universal stability function are given by Arya (2001) as:

$$\phi\left(\frac{H_c - d}{L}\right) = 1 + 5\left(\frac{H_c - d}{L}\right) \quad \text{for} \quad H/L \ge 0 \qquad \text{Neutral and Stable} \qquad (40)$$

$$\phi\left(\frac{H_c - d}{L}\right) = \left(1 - 15\frac{H_c - d}{L}\right)^{-1/4} \quad \text{for} \quad H/L < 0 \quad \text{Unstable} \qquad (41)$$

where d is the displacement height of the canopy. It can be determined from the vertical profile of u (the temporally averaged velocity) or modeled (Pardyjak et al. 2008). The deposition velocity, V_d, is a parameter to quantify removal of particles by impaction (Seinfeld and Pandis 1998). It has been measured experimentally by Zhu et al. (2011) and is, in general, a function of the modes of particle removal: sedimentation (due to gravitational settling), interception (a result of when flow streamlines transport a particle into contact with a vegetative surface), Brownian motion, and impaction (a result of when the time scale of the flow disturbances resulting from a vegetative element is much smaller than the time scale of the particle's response to the changing flow) (Seinfield and Pandis 1998). It is difficult to parameterize V_d; many impaction models require estimates for the size and orientations of vegetative elements (e.g. Aylor and Flesh 2001; Slinn 1982), which are unknown for the three field studies and are difficult to parameterize. Because of the difficulty of estimating V_d, an approximation for V_d is utilized in this work to parameterize T^*. It is assumed that V_d is proportional to the turbulent velocity scale u_*. The basis for this assumption is found by examining the Stokes number, Stk. The Stokes number describes the ability of a particle to faithfully follow a streamline in a flow, and may be thought of as a dimensionless time scale that describes the likelihood of a particle to deposit onto an impaction surface (Hinds 1982). A common parameterization used in field studies is (Seinfeld and Pandis 1998):

$$Stk = (u_* v_s)/(gR), \tag{42}$$

where v_s is the gravitational settling, g is the acceleration due to gravity, and R is the collector radius. Assuming that V_d is proportional to Stk and that v_s and R are constant for the three field studies, the conclusion that V_d is directly proportional to u_* results. This is expressed as the new parameter T_m^*

$$T_m^* = \left. \frac{\alpha u_* H_{can}^2}{K(H_{can})} \right. \tag{43}$$

Because field measurements of V_d indicate that it is smaller than u_* (Zhu et al. 2011) it is assumed that $T_m^* \neq T^*$. However, for canopies of identical mean vegetative element size and PM_{10} plumes of identical size distributions T_m^* and T^* are proportional to each other.

T_m^* can be calculated based on field or model data. For situations in which neither is available, the following methodology can be used:

1. Use Table 10.5 in Arya (2001) to determine z_o for the land type (grass, forest).
2. Use the equation $\gamma = (z_o/(0.28 H_c^{1.5})^2)/0.2$ to calculate γ (the vegetative surface area per unit volume of vegetation.
3. Use a meteorological network such as mesowest (url http://mesowest.utah.edu) to obtain the mean wind speed, u at a reference height of 10 m.
4. Use Seinfield and Pandis (2001) to obtain the Monion-Obukhov length scale, L for cloudy conditions L.
5. Use Eq. 39 to calculate $u_*/K(H_c)$.

This methodology can be applied by practitioners to determine characteristics of the vegetation needed to achieve a desired PM_{10} reduction in the nearest 100 m downwind of an unpaved road.

4. Results and Discussion

4.1. Laboratory Wind Tunnel Measurements

4.1.1. Deposition Experiments

The Stokes number (*Stk*) is a dimensionless parameter that describes the likelihood of a particle to deposit onto an impaction surface (Hinds 1982). This can also be understood as the deposition efficiency. Deposition efficiency is the ratio of deposited particles onto an impaction surface over the total volume of air occupied by the frontal impaction surface area per unit time. The Stokes number is shown below in Eq. 44, where ρ_p is particle density, d_p is particle diameter, C_c is the Cunningham correction factor (~1), μ_{air} is the dynamic viscosity of air, and L_s is the effective length scale of the impaction surface.

$$Stk = \frac{\rho_p d_p^2 C_c U_o}{18 \mu_{air} L_s}$$

(44)

In order to cover a larger *Stk* range and acquire data from the limit of detection (0%) to the point of saturation (100%), three substrate sizes and three velocities were used (i.e., L_s =1.4, 1.0, and 0.5 cm and U_o = 2, 5, and 8 m/s). Regardless of the variation in these parameters, our data for DF versus *Stk* appear to be almost identical to the shape of the curve developed from the experiments of Hinds (1982). The difference is that our data have much smaller *Stk* (due to relatively small particles) and our flow was turbulent. However, our present data indicate significant deposition, ranging from 0% to 100%, but at much smaller *Stk* than expected based on Hinds (1982). This seems to suggest our hypothesis that turbulent mixing enhances deposition onto surfaces is valid. Furthermore, R_λ^n can be used as the appropriate parameter to scale the Stk and fit to the curve developed from Hinds.

Figure 25 shows (i) a plot of *DF* versus *Stk* for the classical laminar flow experiments from Hinds (1982) for particle impaction onto a flat plate, (ii) laminar flow data from the experiments of May and Clifford (1967) using a vertical wind tunnel (neglecting gravitational settling), and (iii) grid-generated turbulence data from our present experiments. Also shown in this plot is our turbulence data that were scaled by $R_\lambda^{0.34}$. The reasoning for scaling by the Taylor-scale Reynolds number has been described in the previous section.
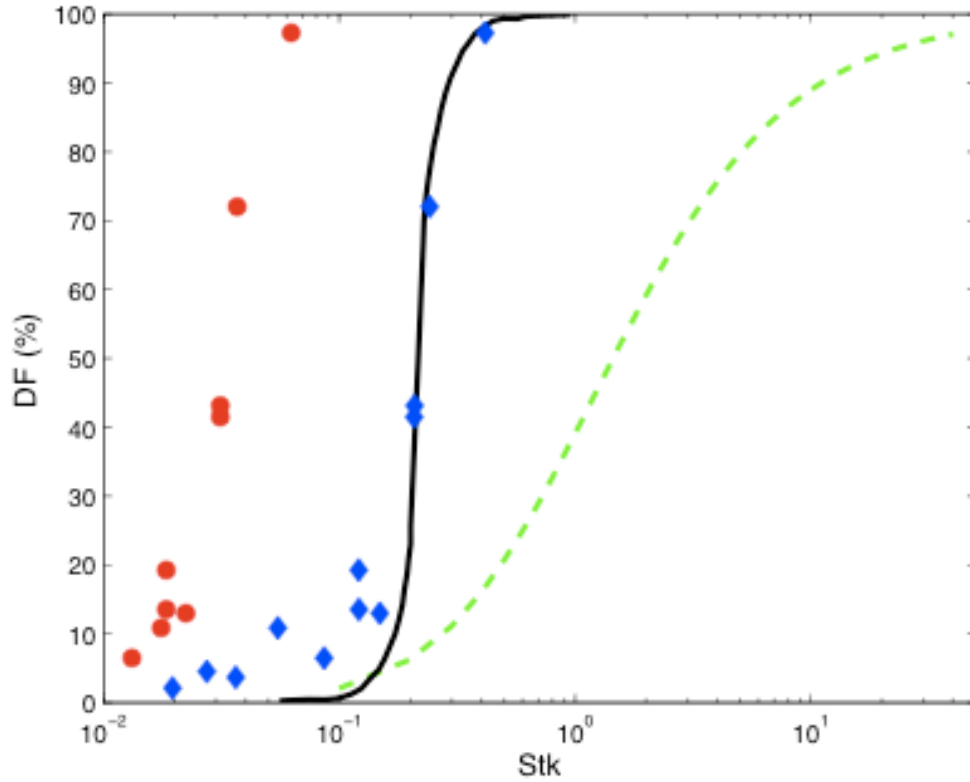
Figure 25: Plot of DF (deposition fraction) as a function of Stokes numbers where the solid black line is the Hinds data (1982), the green dashed line is from the May and Clifford experiments (1967), (red circles) are from the present experiments, and (blue diamonds) are our present experiments scaled by $R_\lambda^{0.34}$.

Figure 26 illustrates the decay of turbulence measured in our wind tunnel compared to a similar grid-turbulence experiment by Comte-Bellot and Corrsin (1965). The turbulence intensity (u_i) at each point is measured from the time series hot-wire data using Eq.10:

$$u_i = \frac{u'}{u}.$$

(45)

In Eq. 45, u is the mean velocity component in the streamwise direction and u' is the r.m.s. of the mean velocity. In theory, our turbulence intensities for every velocity measurement should scale exactly with each other at every point measured due to the behavior of isotropic turbulence. However, there appears to be variation in the calibration curves from before and after the data collection. Review of the two calibration curves indicated that there was a slight variation between velocity measurements before and after data collection. The calibration curves are third order polynomial fits of the voltage from the hot-wire to the velocity derived from the pressure measurements under the idealized conditions in calibration unit. In order to account for the variation between the curves, the two polynomial fits were averaged and a single equation was used for data processing ($R^2 \approx 0.998$). The use of this average fitted equation would suggest errors might have propagated in the calculations of the instantaneous velocity and further into the

turbulence intensity calculations. Figure 26 demonstrates the decay of turbulence intensities for our grid built in the University of Utah Environmental Fluids Lab. The different experiments from the Comte-Bellot and Corrsin (1965) and our present data follow slightly different slopes, owing to the different grid solidities used (0.44 for Comte-Bellot and Corrsin and 0.50 for our present data).

Note in Figure 26, that the distance from the grid (x), is normalized by the mesh spacing of the turbulence grid (M).
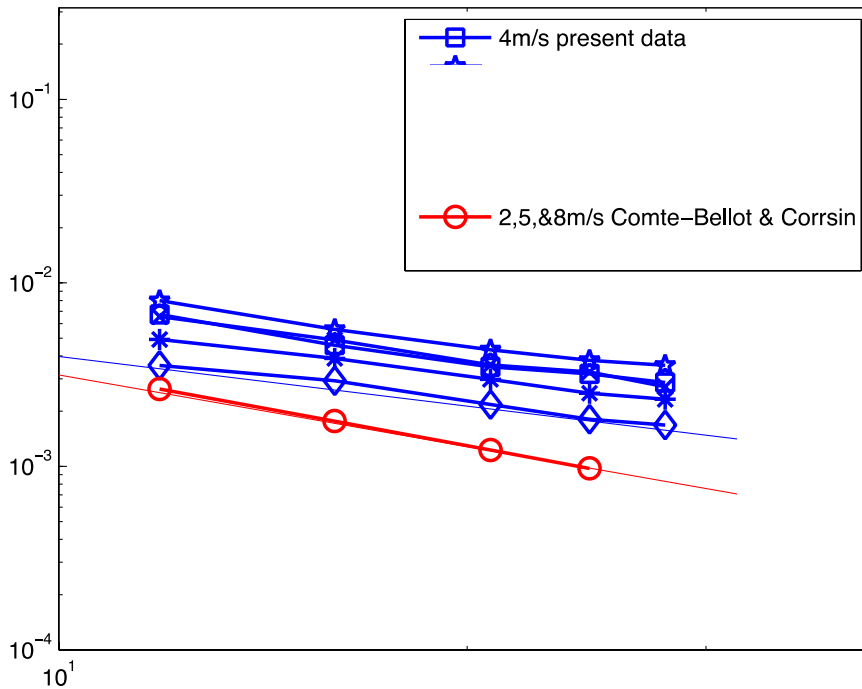
Figure 26: Plot showing the decay of normalized grid-generated turbulence in the University of Utah wind tunnel. Present data follows a line proportional to $(x/M)^{-0.9}$ and the Comte-Bellot and Corrsin data follows a line proportional to $(x/M)^{-1.3}$.

Considering *DF* results, the same *DF* curve at a lower Stokes number indicates that turbulent motion appears to increase the *DF* onto the impaction surface. However, this does not indicate if the turbulent motions are enhancing deposition on the other axes as well. Figure 27 illustrates the effect of isotropic turbulence on deposition for all six-deposition surfaces. Clearly, grid turbulence results in a significant deposition increase on all axes. It should be noted that the ratio of *DF* for turbulent to laminar flow (i.e. turbulence grid to no turbulence grid) is considerably more on the non-impaction surfaces. This appears to indicate that turbulent mixing has a greater influence on the non-impaction surfaces (Moran et al. 2011). Further, deposition onto the surface that is aligned with gravitational vector (+z, where gravitational settling would be important) is not significantly different from the other surfaces. This counter to what would be expected for larger particles (see e.g., Seinfeld and Pandis, 1998), where deposition onto the +z surface would

be very important. Comparing the overall deposition between grid and no-grid experiments, there was a 300% increase in deposition when the grid was used.
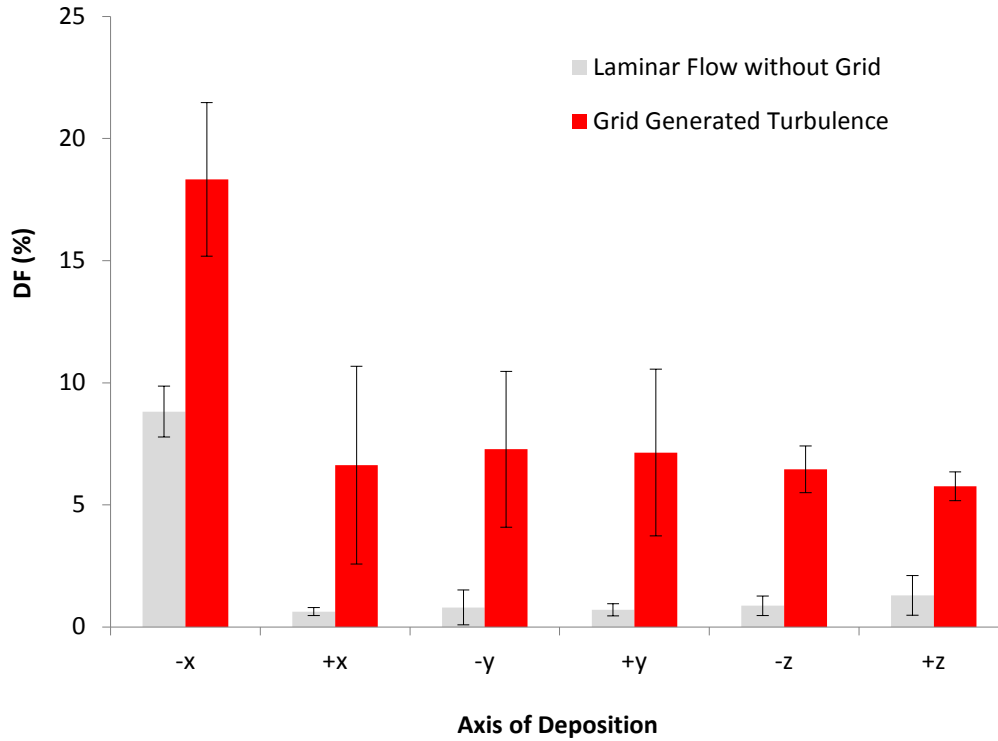
Figure 27: Aerosol DF for each of the various substrate axes for laminar and turbulent flow (U_o = 5 m/s and L_s = 1 cm).

The previous results have been utilized to parameterize deposition fraction, DF, for turbulent conditions. While doing this a new parameter is introduced, a modified Stokes number, Stk^*. It is the product of the traditional stokes number and the Taylor-scale Reynolds number, R_λ. This is expressed as:

$$Stk^* = StkR_\lambda^n. \tag{46}$$

Stk^* is utilized because of the results of the wind tunnel measurements suggest that DF is negligible for Stk* < 1 and becomes significant as Stk^* increases from 1. The traditional Stk does not yield a simple conclusion. DF is related to Stk* by the following expression:

$$DF=(100-100/(440.5*Stk^*)^{3.88}) \tag{47}$$

Eq. 47 has important impacts when using deposition instead of the traditional DF=(Stk/(Stk+0.8))^2. Both expressions require an estimate of mean vegetation element size to estimate DF. The traditional expression requires the mean vegetative element size, d_e, to be extremely small, on the order of 50 μm to give good agreement with PM_{10} field data. In contrast Eq. 47 requires a more reasonable 5-15 mm. Eq. 47 is also less sensitive to small changes to d_e. The collapsed results with the new parameterization are show in Fig. 28 below.

Amatul (2006) implemented the traditional deposition model into QUIC for canopies. One important concern with her model was the need for very small vegetative length scales to produce experimentally observed deposition levels. This current work has replaced the Amatul (2006) model, which required unrealistically small values of d_e to obtain plausible results with the new model, which has realistic values of d_e that correspond to field study results (See Section 3.2).
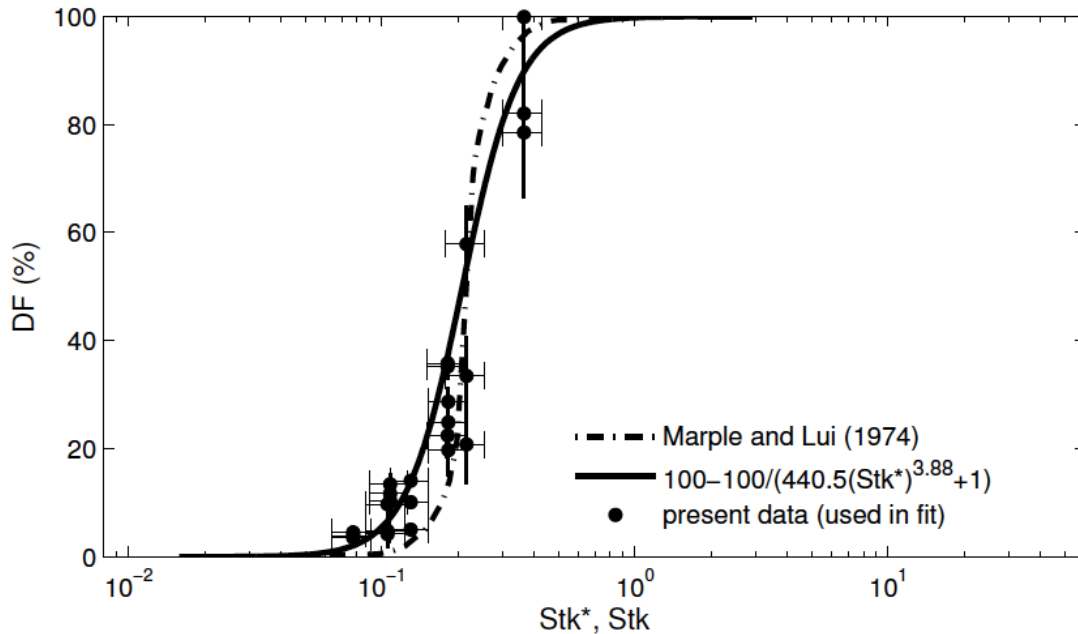
Figure 28: Deposition fraction, DF, as a function of *Stk** showing the collapse of the artificial substrate data.

4.1.2. Vegetation Deposition Experiment

In addition to the above artificial substrate deposition experiments, artificial vegetation, twig elements, and rods were tested to verify that the Stk^* scaling was valid for other geometry. A total of 60 wind tunnel tests were performed (after quality controls) on 7 size categories and wind speeds of 4.9, 8.3, and 9.5 m/s. Generally the results agree with the Stk^* parameterization, however, it is clear that specific geometry and the methods to calculate deposition fraction affect the parameterization.

The vegetation deposition fraction results clearly indicate that the classical laminar theory Stokes number underestimates the dry deposition for all vegetation and rod elements. This result is the same as the artificial substrates also shown in Figure 29.
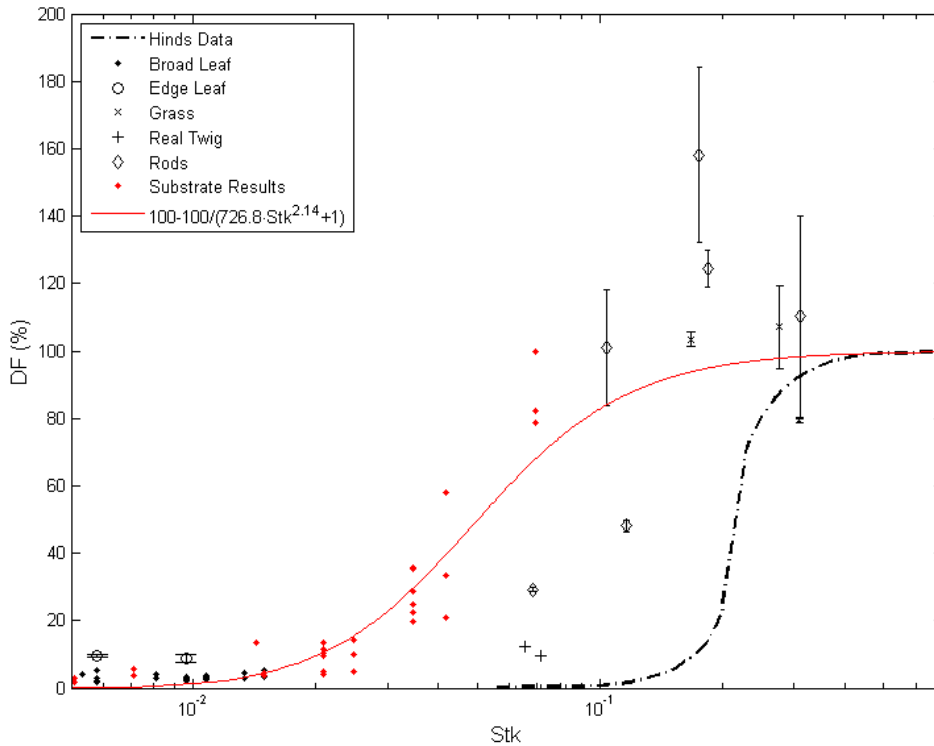
Figure 29: Deposition fraction, DF, as a function of the classical laminar Stokes number for all experiments including vegetation. Deposition values are shown for broad leaf (flat into the wind), edge leaf (broad leaf edge onto the wind), artificial onion grass, twigs, and aluminum and brass welding rod of several diameters. Error bars indicate the standard deviation for identical experiments. The artificial substrate results and parameterization are shown in red.

Applying the modified Stokes number described by Eq. 46, it appears that the parameterization fit is good for low Stk^* values and loosens for higher Stk^* as shown in Figure 30. This may be related to the reason the deposition fraction appears greater than 100%. Eq. 1 is used to calculate the deposition fraction based on the air velocity, the aerosol concentration, the length of time, and the frontal area of the surface. Basically, the deposition fraction is the mass deposited on the surface over the mass of particles in the volume of air that the surface has seen projected through time. In the case of the vegetation tests, DF values in excess of 100% are possible if the Stokes number is high enough to cause very high impaction on the windward surface. Any additional turbulence enhanced deposition on the downwind surface will be added to the deposited mass, thus possibly producing DF > 100%. The results showing DF greater than 100% serve to illustrate the effects of downwind deposition and to illustrate the deficiency of using the projected area when calculating deposition fraction.

48
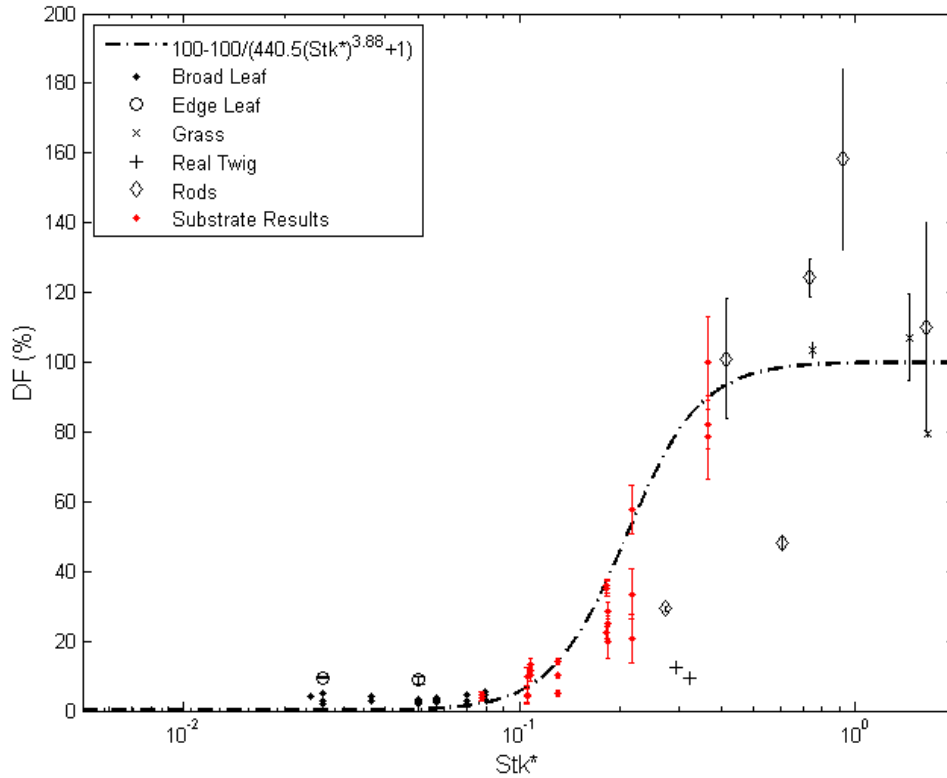
Figure 30: Deposition fraction, DF, as a function of the modified Stokes number (Stk*). Error bars indicate the standard deviation for identical experiments. The artificial substrate results and parameterization are shown in red.

The results show that the broad leaf elements, both faced into the wind and oriented edge into the wind, achieve low deposition rates as the Stokes number is very low. The other elements including grass and rods show much higher deposition as expected by the higher Stokes number (and Stk^*).

Several alternative scaling parameters were investigated to produce a better fit, but none were found that produced satisfactory results. It is believed that there are a combination of factors that may be significant including the ratio of the Taylor Microscale to the characteristic length (λ/D) and the geometry specific width distributions where one element has many Stk^* values. In order to keep the parameterization as general as possible (not species specific), the authors have chosen to incorporate the parameterization from the artificial substrates (Eq. 47) into the QUIC model (Section 3.2).

4.2. Comparison of the Improved QUIC model to the Full-scale Deposition Field Experiment Results

4.2.1. Hanford, Washington Semi-arid Vegetation Experiment

In this section results from the Hanford site field experiments are compared with the improved QUIC model. For these simulations, the coordinate system was defined as shown in Figure 1. That is, Y was parallel to road, X was perpendicular to the road, and Z was vertical. The computational domain was 1000 m x 180 m x 50 m in the Y, X and Z directions respectively. A fetch upwind of the road was specified to be 30 m. The computational grid was uniform in each direction and given by: dy $= 200$ m, dx $= 1$ m, and dz $= 0.25$ m. The vegetation height in QUIC is uniform and specified to be 1.4 m, which was the average vegetation height measured in the field. For all simulations 1,000,000 particles of 5 μm diameter were released. QUIC also requires an attenuation coefficient (e.g. Cionco 1965) to model the velocity profile within the vegetative canopy as described by Pardyjak et al. (2008). The attenuation coefficient was selected to best match the observed velocity profile (see Fig. 32). Within the vegetation, an attenuation coefficient of 1.4 was specified. The input meteorological conditions for each QUIC simulation were specified from the experimental data presented in Table 2.

Objective 1

The atmospheric conditions for the June 7, 2011 *Objective 1* IOP at Handford, WA were unstable as indicated by a Monin-Obukhov length scale $L = -47.7$ m. The average turbulent kinetic energy was 0.4 m^2/s^2 and the turbulent velocity scale u_* was 0.61 m/s. All of these quantities were evaluated from measurements made at a height of 3.9 m (which should be well within the constant flux layer of the atmosphere). The aerodynamic roughness height $z_o = 0.07$ m and the average wind speed at 3.9 m was 5.4 m/s during the experiment.

The experimentally measured horizontal flux, along with its location, and the calculated F_{min} value utilizing Eq. 23 are shown in Table 7 and Figure 31 where the horizontal flux F is normalized by the roadside flux, $F_{roadside}$.

Tower	Location Downwind (m)	Measured Flux $F/F_{road\ side}$	Measured $F_{min}/F_{road\ side}$	QUIC Estimated $F_{min}/F_{road\ side}$
Tower 1 (Roadside)	0	1.00	0.72	0.71
Tower 2 (Middle)	6.4	0.86±0.14	0.72±0.1	0.71
Tower 3 (Downwind)	56.4	0.74±0.13	0.71±0.11	0.71

Table 7: Results from the *Objective 1* IOP on June 7, 2011 (unstable atmospheric conditions). QUIC simulations predicted an $F_{min}/F_{roadside}$ value of 0.71 given the site roughness and meteorological conditions. The measured values in the right most column, closely agree with the QUIC value.
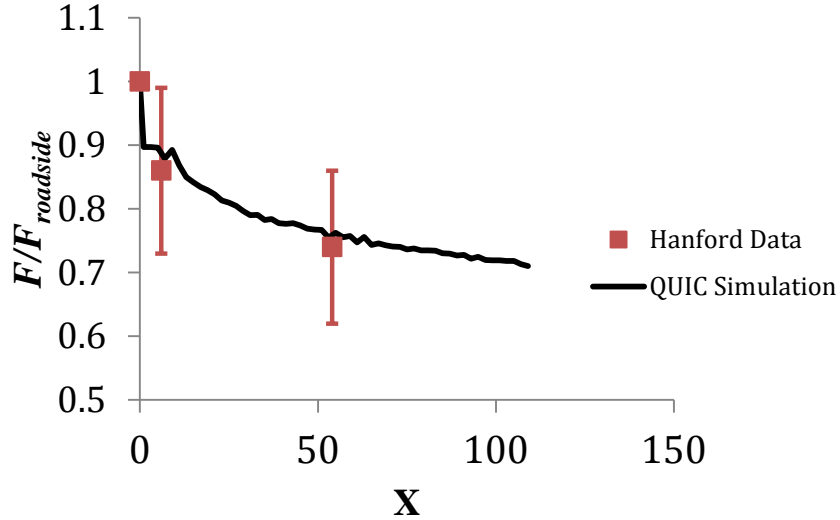
Figure 31: The measured decrease in normalized horizontal PM_{10} flux, F, compared to the QUIC simulation of the same of the Handford, WA June 7, 2011 IOP. Bars are 95 % confidence intervals.

Again, the first objective of the flux study was to validate the QUIC deposition model for vegetative canopies. The quantity $F_{min}/F_{road\ side}$ was utilized as a metric to estimate the accuracy of QUIC (See Fig. 31). The QUIC computations produced a value of 0.71 for $F_{min}/F_{roadside}$. This may be compared to the measured results in the right most column of Table 7. The measured results were calculated using Eq. 22 with the middle and far downwind towers. The result was then normalizing the by the measured $F_{roadside}$. The relative difference between the middle towers measured 0.72 and the QUIC estimated 0.71 is only 1.4% suggesting that for the June 7 IOP QUIC is modeling the processes of deposition and dispersion well.

Objective 2
The atmospheric conditions for the June 13, 2011 *Objective 2* IOP at Handford, WA were weakly unstable as indicated by a Monin-Obukhov length scale $L = -117$ m. In the constant flux layer above the canopy, the average turbulent kinetic energy was 0.3 m^2/s^2 and the turbulent velocity scale u_* was 0.71 m/s. All of these quantities were evaluated from measurements made at a height of 3.9 m (which should be well within the constant flux layer of the atmosphere). The aerodynamic roughness height $z_o = 0.07$ m and the average wind speed at 3.9 m was 6.8 m/s during the experiment. The QUIC models for mean advection and turbulent kinematic shear stress $u_* = \sqrt{\overline{u'w'}}$ within canopies are shown in Figures 32 and 33. The model for the mean wind shows excellent agreement. The model for turbulent shear stress is satisfactory; however the QUIC model displays a non-physical corner at the top of the canopy. This is most likely a consequence of the simple canopy model that assumes a constant vegetative density, γ, with height within the canopy.
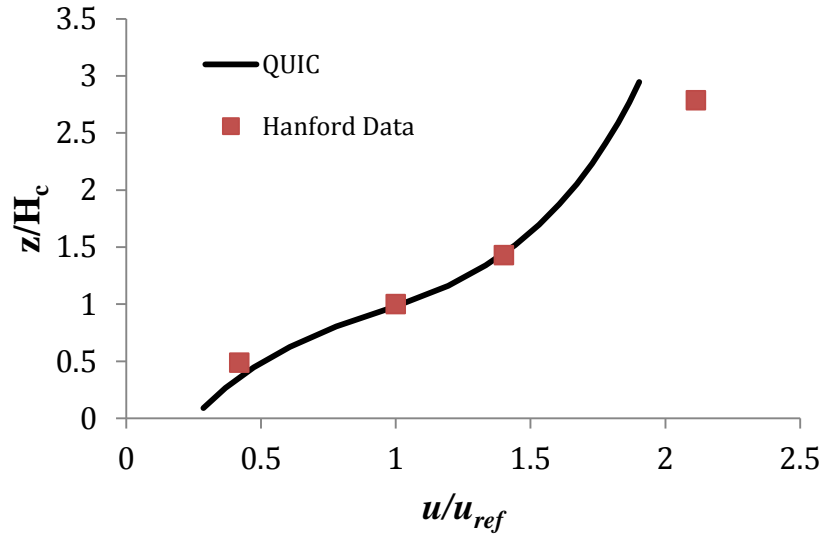
Figure 32: Comparison of the QUIC vegetative canopy mean wind model to 3D sonic anemometer data taken 37 m downwind of the road, during the June 13, 2011 IOP at Hanford, WA.
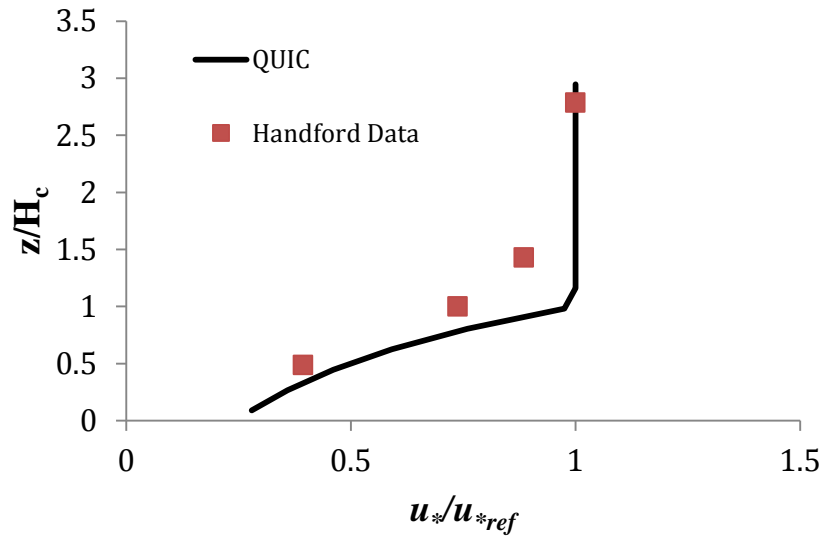
Figure 33: Comparison of the QUIC canopy turbulence model to 3D sonic anemometer data 37 m downwind of the road, taken during the June 13, 2011 IOP at Handford, WA. Here u_* is a local turbulent kinematic shear stress.
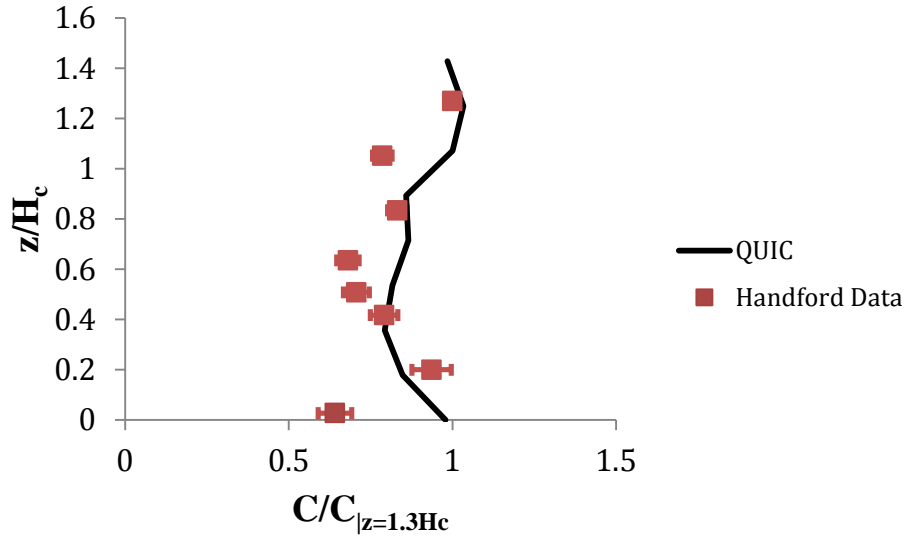
Figure 34: The variation of concentration with height within the canopy at Hanford, WA. The field data indicates that concentration, C increases with height in an irregular manner that is generally followed by the QUIC simulation except near the ground. These data were taken 32 m downwind of the road. Error bars indicate 95% confidence intervals.

Figure 34 shows the high-resolution concentration profile taken 32 m downwind of the road. The simulation and field data show good agreement except near the ground. This is most likely a consequence of deposition to the ground being underestimated. The QUIC simulation shows a decrease in concentration with increasing height in the bottom half of the canopy. In the top half of the canopy QUIC predicts an increase in concentration with increasing height. The data show the same basic trends but discrepancies between simulation and data occur at multiple points. This is most likely due to canopy heterogeneities. To better understand the significance in the variability shown in Fig. 34, we note that the colocation tests had a standard deviation of approximately 0.06 mg/m^3 (See Appendix A). In Fig. 34, the normalizing concentration was $C_{|z=1.3Hc} = 41$ mg/m^3. Hence, the differences in Fig. 34 which are greater than ~0.06/41 = 0.0015 are larger than the inter-instrument variability. This indicates the curvature in the measurements could indeed be real.

To better quantify the predicted error from the QUIC simulations, we introduce the following metrics that are often used (Warner et al., 2004) to evaluate dispersion models. In the following equations C_p indicate predicted values from running QUIC, while C_o are observed measurements from the field experiments. The following metrics have been computed:

FB - Fractional Bias

$$FB = \frac{\overline{C_p} - \overline{C_o}}{0.5(C_p + C_o)}$$

RE - Relative Error

$$RE = \frac{\overline{C_p} - \overline{C_o}}{\overline{C_o}} * 100\%$$

NMSE - Normalized Mean Square Error

$$NMSE = \frac{\overline{(C_p - C_o)^2}}{\overline{C_p}\,\overline{C_o}}.$$

Here, the overbar indicates an average over all of the samples. The first two metrics are indicative of the model's ability to over predict or under predict a value, while the NMSE is measure of the spread. Figure 35 Below illustrates these paired comparison parameters, while Table 8 shows the numeric values of the parameters. Here, Mean Wind is a comparison of mean wind speed, Turbulence is a comparison of the local u_* and Concentration is local concentration.

Quantity	FB	NMSE	RE (%)
Mean Wind	-0.00063	0.00621	0.24999
Turbulence	0.13993	0.02955	15.639
Concentration	0.10187	0.02687	11.682

Table 8: Error metrics for the Handford, WA experiment for the mean wind, turbulence and concentration measurements.
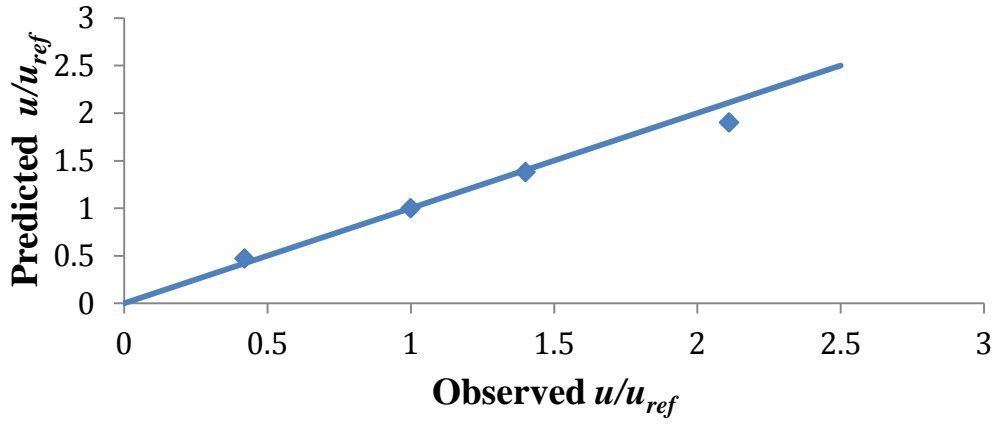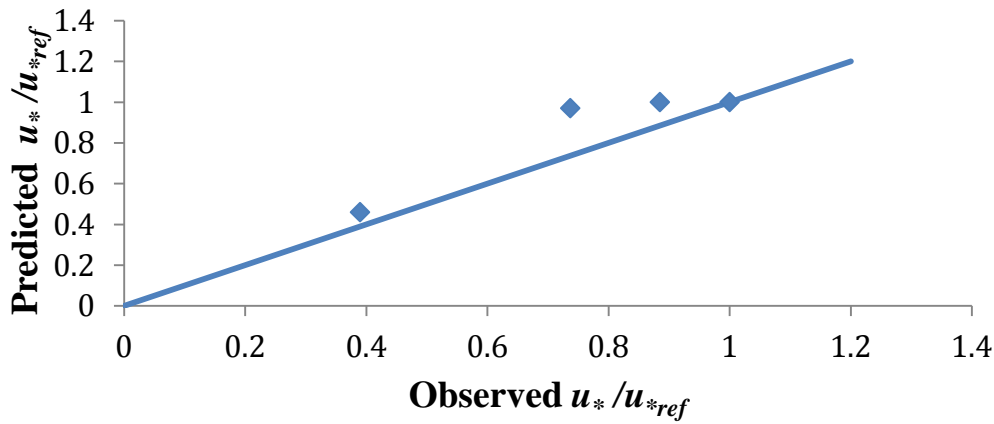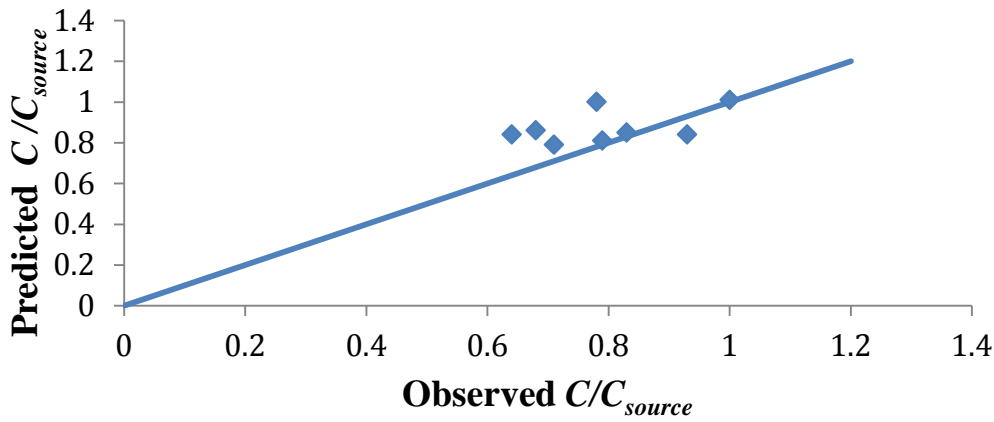
Figure 35: Normalize scatter plots comparing the QUIC predicted mean wind speed, turbulence and concentrations with the field observations taken at Handford, WA.

The heterogeneity of the canopy is shown in the results from the LAI measurements in Figure 36. The measurements indicate that the majority of the vegetative surface area is located near the ground. For example the top half of the canopy contains only about 10% of the vegetative surface area. This is in contrast to the simple canopy model that has been implemented in QUIC, which assumes that vegetative surface area is distributed evenly vertically and horizontally. This plot indicates there is tremendous variation of vegetative density in both the vertical and horizontal. Despite heterogeneities present in the canopy, the simple homogenous canopy model offers a simple modeling tool for estimating the transport and removal of PM_{10} in conditions typical of military ranges. The error metrics presented above provide an initial indication of the uncertainty in the model. Further experimental data are necessary to understand the models ability to be widely applicable over different types of vegetation.
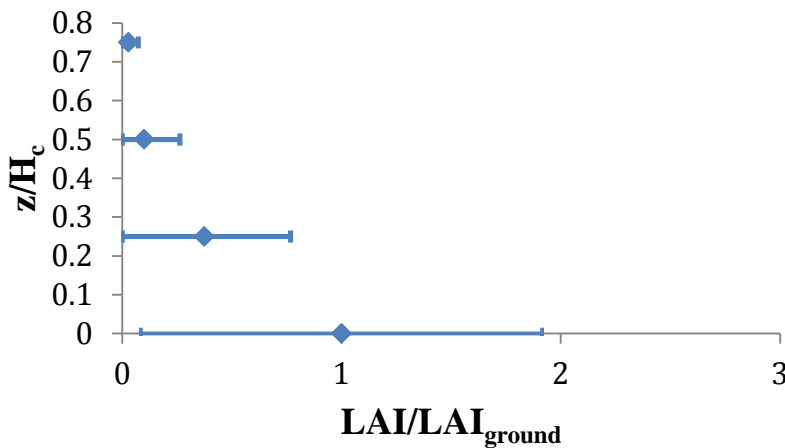
Figure 36: The decrease of LAI with height within the canopy at Hanford. The figure indicates the majority of the vegetative surface area is located near the ground. For example the plot indicates 100% of the vegetative surface area is located above $z/H_c = 0$, slightly less than 40% is located above $z/H_c = 0.25$, and so forth. Also note the tremendous variation in LAI measured as noted by the standard deviation error bars. These data were taken from 48 LAI profiles taken on a uniform grid with the 3D sonic tower being the origin.

Impact of the New Deposition Model

Figure 37 shows the dependence of the simulated QUIC transmitted fractions ($TF = F_{min}/F_{road\ side}$) on the vegetative element size that must be specified in the simulations, d_e, for the Handford, WA site on June 7, 2011. Figure 37a shows a traditional removal model that neglects turbulence enhancement of PM_{10} deposition and, while Fig. 37b shows results from the new model (Eq. 47) that incorporates turbulence enhancement. Note, that while *TF*s with reasonable values can be achieved with standard models in which turbulence enhancement is neglected, unrealistically small vegetation elements (~50 µm) must be used to explain the measured removal rates ($TF\approx70\%$) measured. If turbulence effects are, included realistic values for ($d_e \sim$ 10 mm) explain the removal measured. In summary vegetation in canopies (and windbreaks) have higher PM_{10} removal rates than suggested by traditional removal theory. The Handford June 7, 2011 data indicate that the new particle deposition model introduced into QUIC as part of this project has greater physical fidelity than traditional models such as those used by Amatul (2006) that utilize Eqs. 16 and 17. Note also that the new model also shows smaller sensitivity to d_e as well. This has large implications given the relatively high uncertainty which exists in estimating vegetative element sizes.
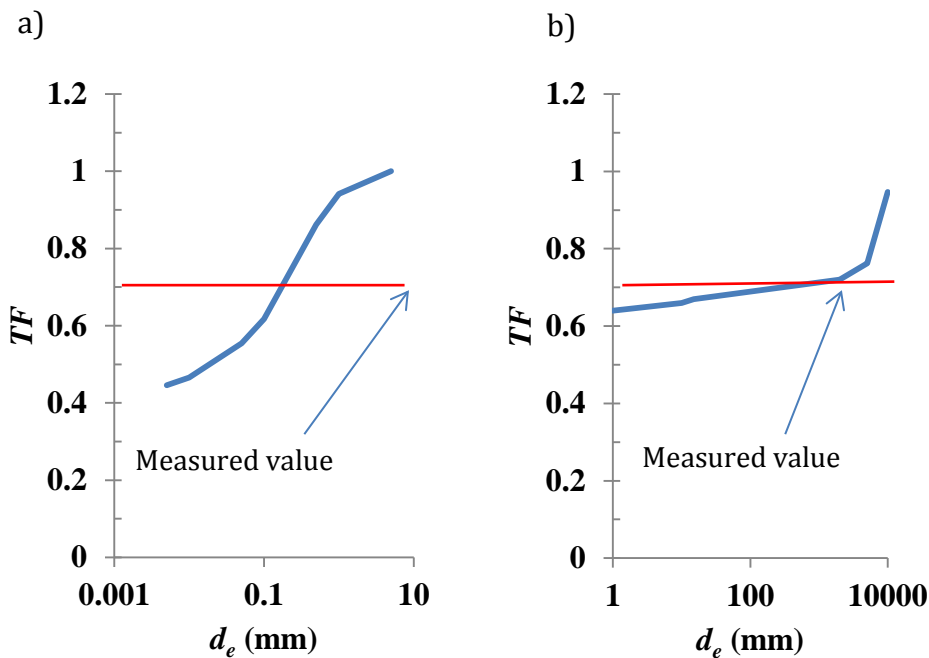
Figure 37: Dependence of QUIC measured transmitted fraction upon the vegitative element size, d_e, assumed in (a) the orginal QUIC model and (b) the modified QUIC model shown for the Handford, WA June 7, 2011 field study. Panel a) displays results from a traditional PM_{10} removal model, that neglects turbulence enhancement to deposition (Amatul 2006). In panel b) the new deposition model developed in this work includes turbulent enhancement of deposition. Accounting for the effects of turbulence on deposition results in realistic estimates for d_e ; neglecting it requires unrealistically small values for d_e to account for measured removal. Transmittance Fraction is defined Section 2.5.

4.2.2. Raft River Windbreak Experiment - Malta, Idaho

Because of two equipment failures, the wind data and PM_{10} concentration data were taken during two separate IOPs. The wind data were taken during the July 12th IOP and the concentration data were taken on the July 27th IOP. Even though a failure occurred that deleted the majority of the 3D sonic wind data on the July 27th IOP, the upstream 3D sonic data survived. This is important because these data are necessary to generate an accurate QUIC simulation of the PM_{10} dispersion.

The two thick windbreaks each had an optical porosity of approximately 0.01 and fetches (thicknesses) of 7 m. The optical porosity was determined by first computing an aerodynamic porosity (α) from the 3D sonic anemometer data subsequently using the $\alpha=\beta^{0.4}$ model to solve for β, the optical porosity. The height of each windbreak was approximately 4 m. The upstream roughness was 0.02 m.

In this section results from the Raft River Windbreak field experiments are compared with the improved QUIC model. For these simulations, the coordinate system was defined as shown in Figure 1. That is, Y was parallel to road, X was perpendicular to the road, and Z was vertical. The computational domain was 1000 m x 180 m x 50 m in the Y, X and Z directions respectively. A fetch upwind of the road was specified to be 30 m. The computational grid was uniform in each direction and given by: dy = 200 m, dx = 1 m, and dz = 0.25 m. For all simulations 1,000,000 particles of 5 μm diameter were released were released. The input meteorological conditions for each QUIC simulation were specified from the experimental data presented in Table 2.

July 12th IOP
This nighttime IOP measured the mean and turbulent winds created by the presence of the windbreak. The atmospheric conditions were slightly stable with a Monin-Obukhov length scale, L = 95 m that was measured at a height of 3.25 m upstream of the windbreaks. The turbulent velocity scale, u_*, was 0.33 m s^{-1} again measured at 3.25 m upstream. The wind speed data for winds that were approximately perpendicular to the windbreaks are shown for Towers: B (x = 13.8 m), C(x=24.8 m), D(x=3.5 m), and E(x=55.8) are shown in Figures 38 and 39 along with the QUIC simulation results.

x = 13. 8 m (in between windbreaks)

x = 27. 8 m (leeward of 2nd windbreak)

x = 42.1 m (3.5 H_{wb} Downwind of 2nd windbreak)

x = 55.4 m (6. 75 H_{wb} Downwind of 2nd windbreak)

QUIC

Malta Field Study

z/H_{wb}

u/u_{ref}
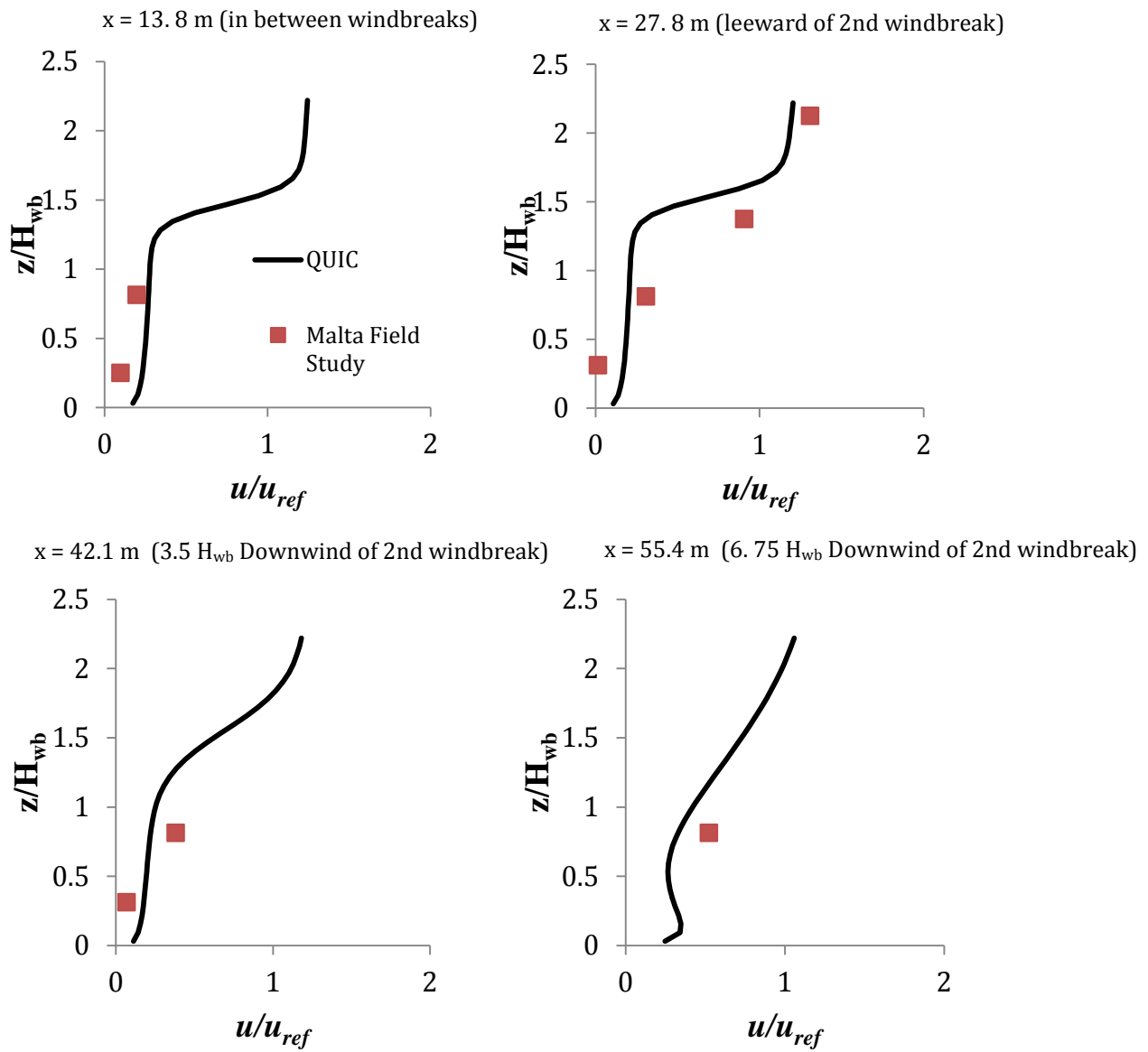
Figure 38: Comparison of QUIC simulations and Raft River Windbreak field experiment data for the mean winds from the July 12, 2012 IOP. Reference values measured at a height of 3.25 m upstream of wind breaks.
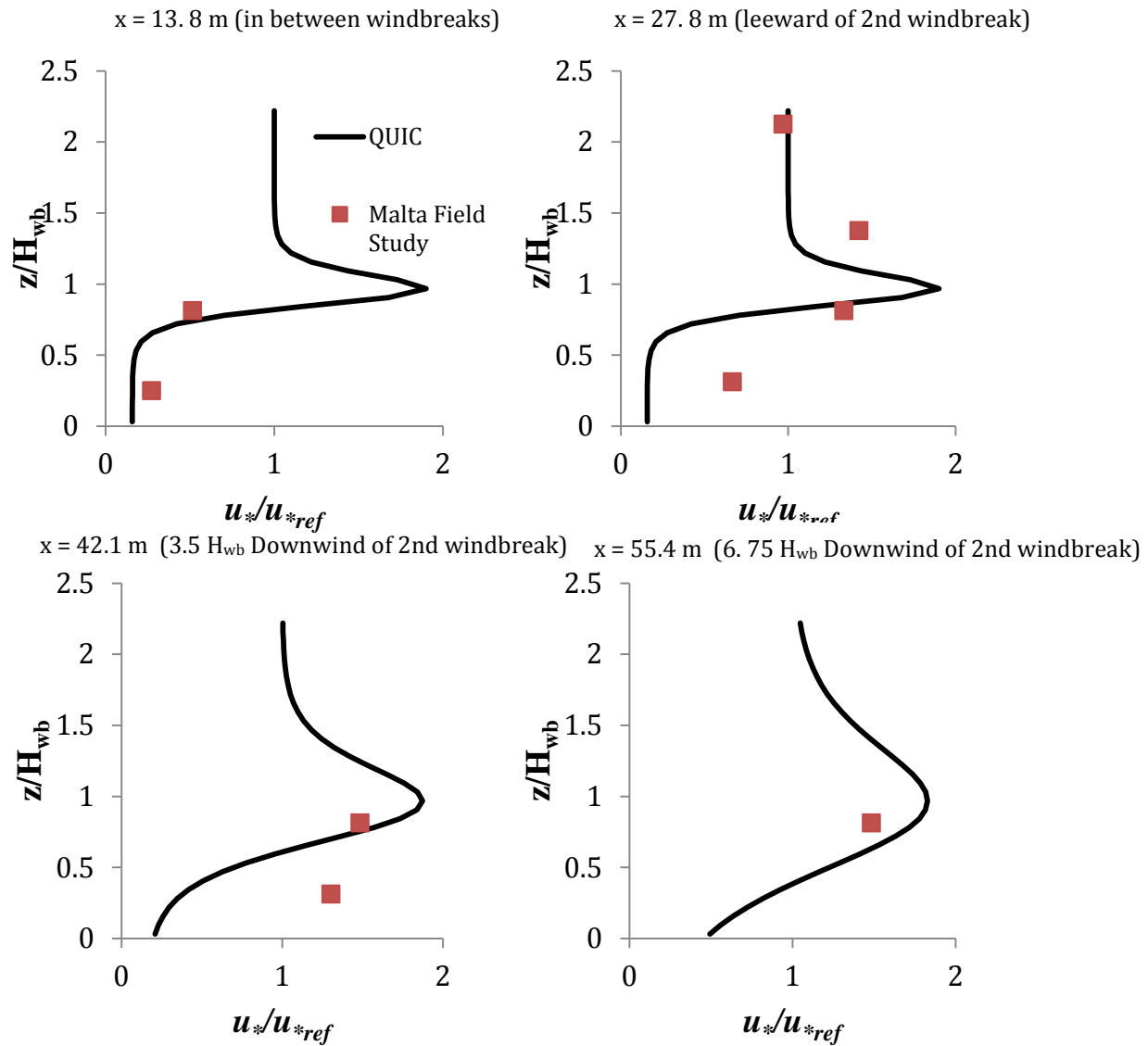
Figure 39: Comparison of QUIC simulations of windbreak turbulence (local kinematic turbulent shear stress) to Malta wind IOP (July 12, 2012). Reference values measured at a height of 3.25 m and 35 m upstream of the windbreaks.

The figures indicate that the QUIC simulation and the Raft River Windbreak wind data is able to follow the trends of both the mean wind and the turbulence. The quiet zone is evident between the windbreaks (upper left panel) as well as the high shear located leeward of the second windbreak (upper right panel). The initial recovery of the flow from the disruption of the windbreak is evident in the lower two panels. The sensor array, which was limited in size by a highway, was not sufficiently large to capture the complete recovery of the flow from the disruption of the windbreak.

QUIC suggests some trends that were not observed by our sensor array. Namely, concerning the mean wind, the lower right panel of Fig. 39 shows a slightly elevated velocity "bump" near the ground in the vertical profile of u. This is a result of the high shear zone, which starts at the top of the windbreak, reaching the ground and accelerating the local flow. Such phenomena are

difficult to observe in field studies. They have, however, been observed in wind tunnel studies such as Judd et al. (1996). Evidently, the new QUIC model is able to resolve such features.

July 27th IOP

This daytime IOP measured dispersion of PM_{10} with the flow the presence of the windbreak. The atmospheric conditions were very unstable with a Monin-Obukhov length scale of $L = -2$ m that was measured at a height of 3.25 m upstream of the windbreaks. The turbulent velocity scale, u_*, was 0.36 m s^{-1} again measured at 3.25 m upstream. The measurements at Towers: B (x = 13.8 m), C (x=24.8 m) and D (x = 3.5 m), are shown in Figure 40.
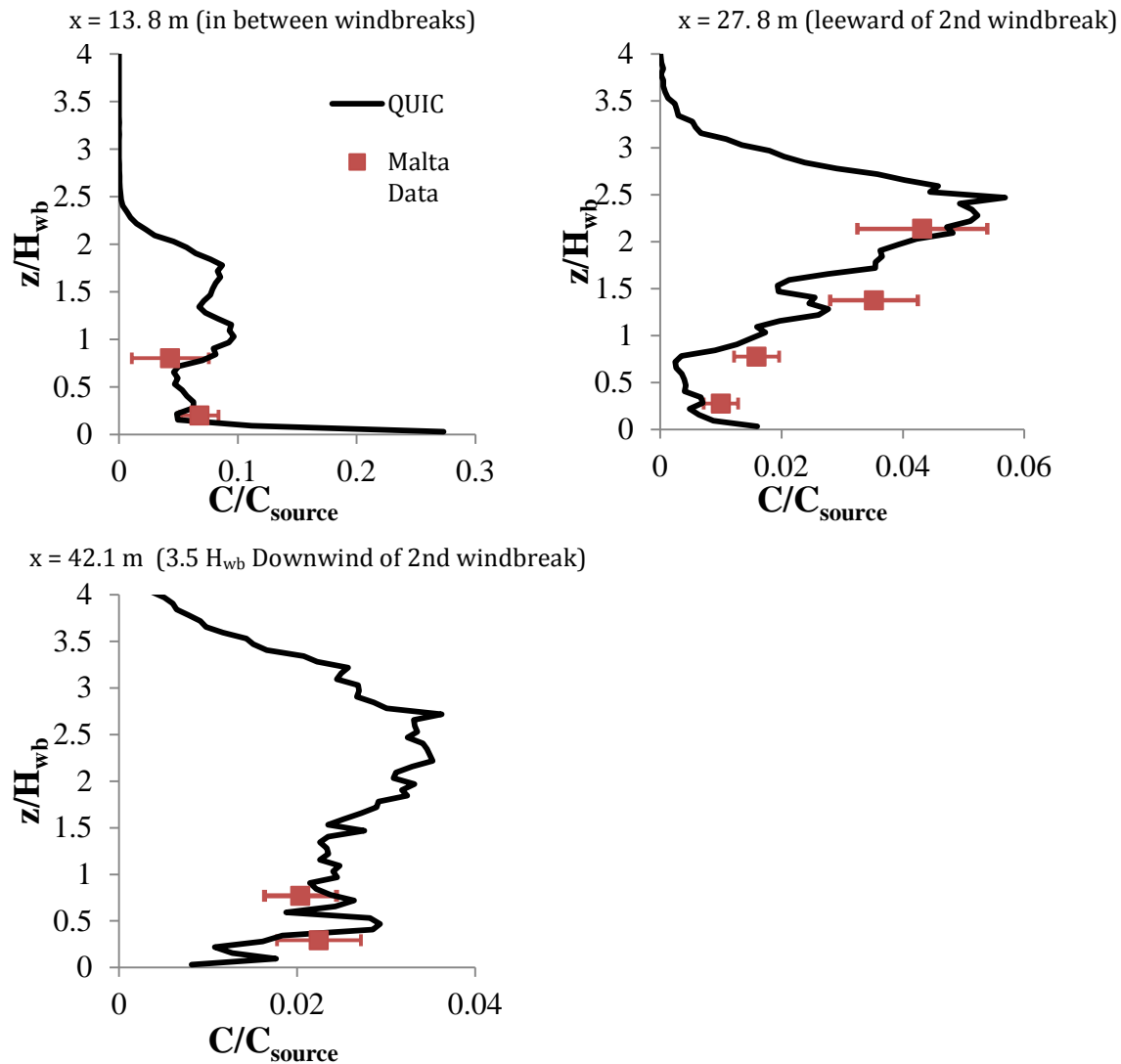
**Figure 40:** Comparison of QUIC simulation results to the Raft River Windbreak (Malta, ID) PM_{10} concentrations for the July 27, 2012 IOP. C_{source} is the PM_{10} measurement at x=1.0 m z= 1.39 m on tower B (just adjacent to the road).

The results indicate a general agreement between the PM_{10} and the QUIC simulations trends, as was the case for the mean wind and turbulence profiles. The quiet zones exhibit substantial removal as shown by the bottom two measurements in each of the two top panels. The PM_{10} concentration measurements in the displaced profile (Region C in Fig. 8) are significantly higher than those in the quiet and bleed zones. This is a result of two mechanisms: 1) The windbreaks are tremendously effective at removing PM_{10} from the flow field and 2) the very low porous windbreaks permit a very low flow rate to pass through them; to compensate the flow contains a component that flows over the windbreaks. This flow component is present at the windward side of the first windbreak. Because this is also the location of the road PM_{10} is transported over the windbreak and cannot be removed. The flow of PM_{10} over the windbreaks can be greatly mitigated if a windbreak is installed upwind of the road along with the downwind windbreaks. The upwind windbreak strategy   has the undesirable consequence that concentrations near the road will be significantly higher than they would without the upstream windbreak.

In an effort to better quantify the performance of the model with the limited data sets, the following performance metrics were computed as done for Handford, WA above: (FB), NMSE, and RE. Here, Mean Wind is a comparison of mean wind speed, Turbulence is a comparison of the local u_* and Concentration is local concentration.

Quantity	FB	NMSE	RE
Mean Wind	0.12446	1.29956	-38.46
Turbulence	-0.32409	0.55432	-19.84
Concentration	-0.14765	0.14106	-9.62

Table 9: Error metrics for the Raft River Valley Windbreak experiment for the mean wind, turbulence and concentration measurements.

Figure 41 below illustrates the model performance using scatter plots. The RE for the wind and turbulence field for windbreak (Malta, ID) case is larger than for the deep vegetation field experiment (Handford, WA), however in spite of the larger flow error the concentration errors are similar in both cases (12% for Handford and 9.6% Malta).
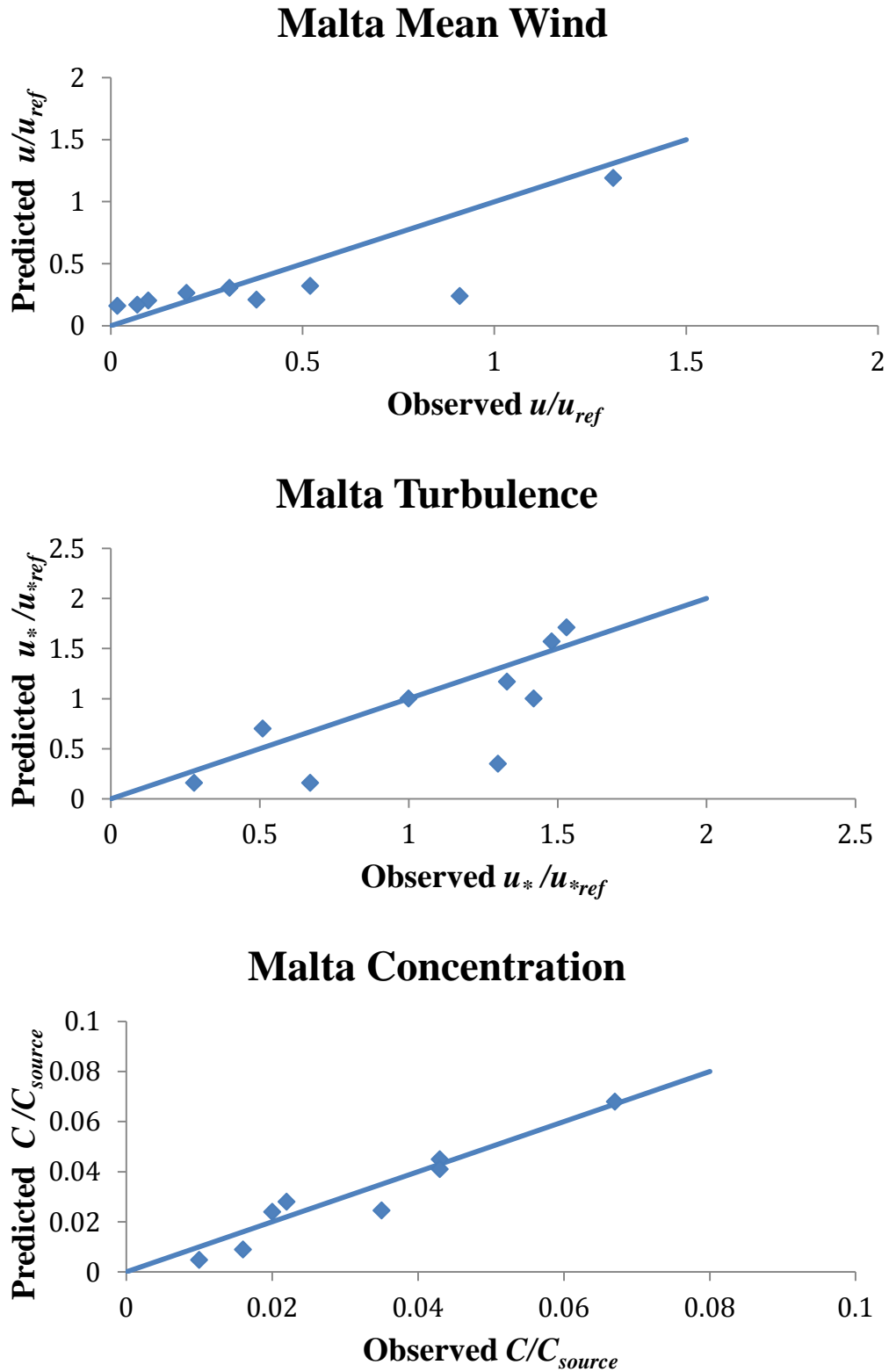
Figure 41: Normalize scatter plots comparing the QUIC predicted mean wind speed, turbulence and concentrations with the field observations for the Raft River Windbreak field experiment.

4.3. Development of Simple Empirical Formula for Native Vegetative Removal

A set of many QUIC-PLUME simulations was performed to estimate canopy removal as a function of the height and thickness of the native vegetation. The simulations were run with the same basic QUIC set-up described in Section 4.2.1. The results are shown in Figure 42 together with results from four field studies including the Handford, WA field study. Fluxes were computing by counting particles as they passed horizontal planes over a time interval. These studies include Dugway, Utah (Veranth et al. 2003), Ft. Bliss, Texas (Etyemezian et al. 2004) and Las Cruces, New Mexico (Speckart et al. 2013). The QUIC simulation results and the four field studies indicate increases in canopy height (H^*) and canopy density T_m^* exponentially decrease the transmitted fraction, *TF*. For relatively sparse and short canopies, shown on the lower left hand corner, a relatively small increase in either density or height greatly reduces *TF* and for tall and dense canopies, on the upper right hand corner, *TF* is insensitive to changes in either canopy height or density. This suggests that there is a "law of diminishing returns" in the mitigation of fugitive dust. Once a critical height and density are reached, the addition of more vegetation would not enhance the canopy's removal ability.

It should be noted that Figure 42 also indicates the sensitivity of the model to changes in parameters related to H* and T_m^*. Regions where the contour lines are packed closely together are particularly sensitive. Recalling Eq. (43)

$$T_m^* = \left. \alpha u_* H_{can}^2 \middle/ K(H_{can}) \right. \tag{43}$$

We see that T_m^* includes key parameters related to leaf area (via α), roughness (via the canopy heights), atmospheric stability and turbulence (via K and u_*). Hence, this non-dimensional result provides key insight into the sensitivity of a wide range of variables effecting deposition in canopies.
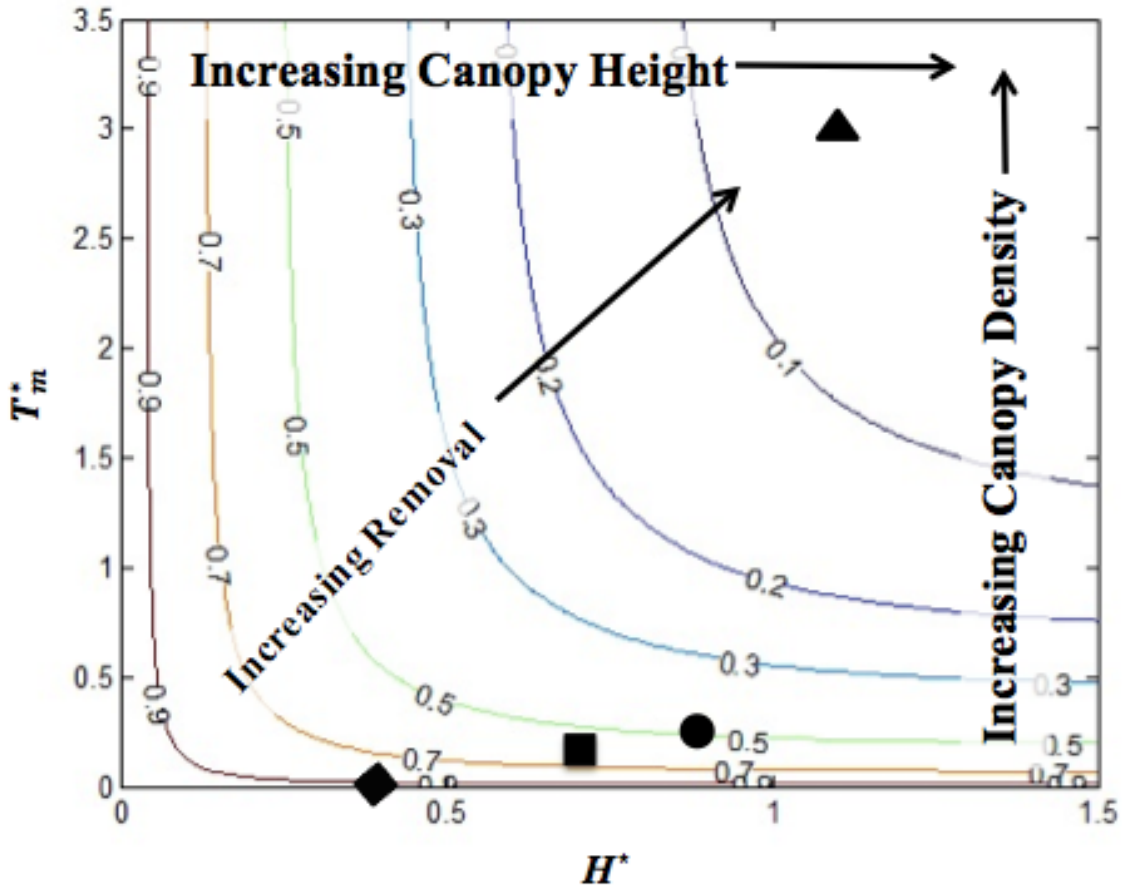
Figure 42: Contours of constant transmitted fraction, *TF*, as a function of H^* and T_m^* together with the field data from the Dugway (■), Ft. Bliss (▲), Las Cruces(◆) and Handford (●) field studies. Contours are generated from the results of 56 QUIC simulations.

Lastly, the 56 QUIC simulations can be fit by the following equation:

$$TF = (1 - CF) = (1 - \exp(-2.8H^*))\exp(-2.0T_m^{*0.64}) + \exp(-2.8H^*). \qquad (48)$$

In Eq. 48, *CF* and *TF* are the captured fractions and transmitted fractions respectively.
This equation is compared to the experimental data in the plot shown in Figure 43. The ordinate of the plot is physically interpreted as the transmission efficiency (1-removal efficiency) and incorporates the effects of varying the canopy height for a given plume height. Canopies at the far left, such as Ft. Bliss, are sparse and inefficient at removing particles. Dense canopies such as Dugway are efficient and intermediate canopies such as Las Cruces are intermediate between the two extremes. Eventually, as at a canopy density similar to that of Dugway ($T_m^* \sim 3$), the removal efficiency reaches a limit and increases in canopy density fails to increase removal efficiency. The fitted model to the 56 QUIC plume simulations slightly over predicts removal compared to the experimental data.
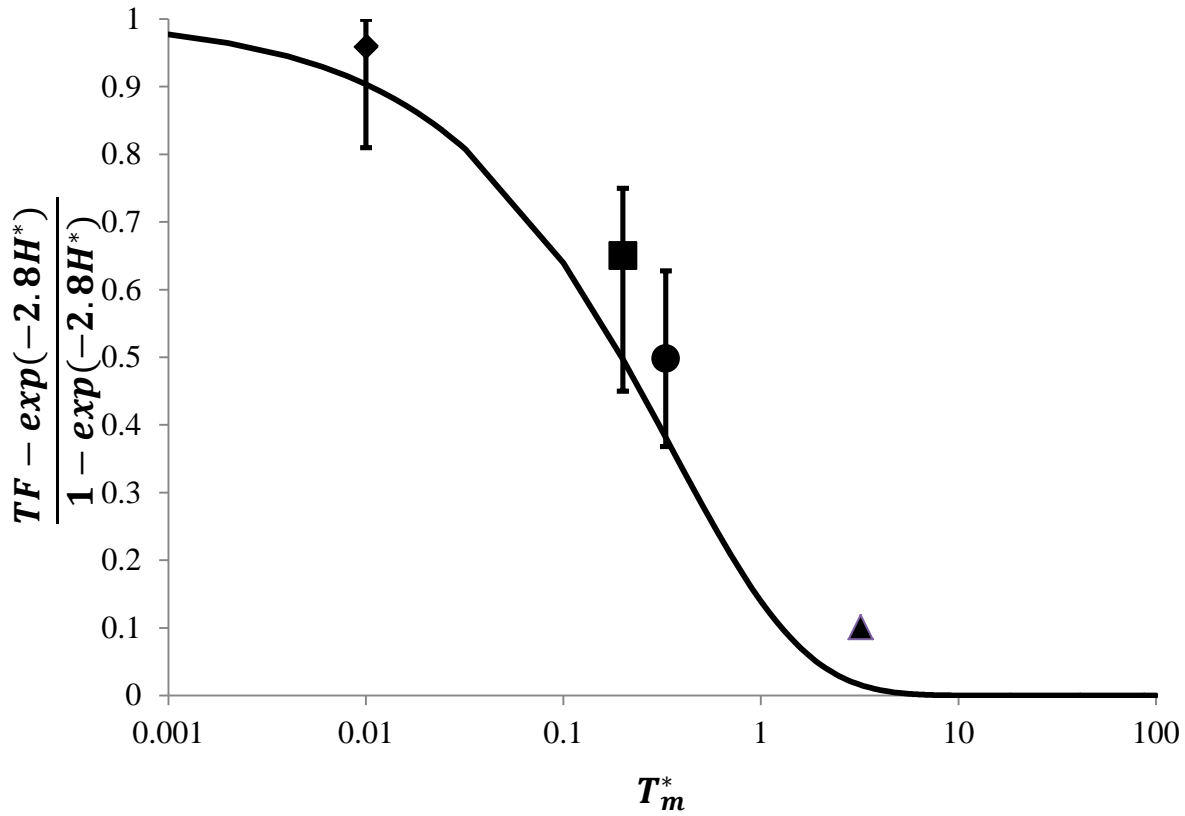
Figure 43: Eq. 34 compared to the four field studies measuring ambient removal. This figure shows that the PM_{10} transmission efficiency, $\frac{TF-exp(-2.8H^*)}{1-exp(-2.8H^*)}$,increases with increasing T_m^* . Consequently the removal efficiently, $1 - \frac{TF-exp(-2.8H^*)}{1-exp(-2.8H^*)}$

Increases with increasing T_m^*.

5. Conclusions and Implications for Future Research/Implementation

This SERDP project produced a wide range of important results that have improved our understanding of flow and deposition in vegetative canopies and around windbreaks as well as improved modeling capabilities. Specifically, we have (i) shown experimental evidence that turbulence enhances dry-deposition onto all surfaces of vegetation even for small particle sizes (e.g. PM_{10}), (ii) developed a dry-deposition model for the removal of particles that incorporated the effects of turbulence, which were neglected in previous dry-deposition models, (iii) developed accurate models for the mean wind and turbulent flow resulting from windbreaks, (iv) conducted a field study at Handford, WA that demonstrated the utility of *real-time* QUIC modeling for experimental design and prediction of transport within native vegetation, (v) developed a simple empirical relationship and methodology that relates PM_{10} removal to native vegetative height and thickness (vi) conducted a second field study in the Raft River Valley near Malta, ID in which mean and turbulent flows were measured along with PM_{10} transport within and downwind of windbreaks and produced data used to validate the new windbreak and particle models integrated into QUIC. The results from the enhanced QUIC model show good agreement with the field data from the Handford, WA and Malta, ID studies along with data from the other field studies. Specifically the predicted concentration relative error at Malta, ID was ~10% and the error at Handford, WA was ~12%.

Implications: (i) The improved QUIC model can be run to estimate the effectiveness of vegetation or windbreaks on near-source removal in the field, minimizing the need for costly field experiments or providing a way to help design experiments. (ii) The *Simple Empirical Formula* that was developed can be very useful for practitioners to make first estimates of the effectiveness of vegetation in remove near-source dust at a specific location. The non-dimensional form of this method provides insight into the sensitivity of a wide range of variables effecting deposition in canopies. (iii) The new deposition model that was produced yields plausible PM_{10} removal rates while assuming realistic vegetation element sizes. Previous models required unrealistically small element sizes for plausible PM_{10} removal rates. This implies that measurements of typical vegetation length scales (e.g. leaf width) can be used in the new model.

Future research: This work has improved our understanding of how turbulence influences PM_{10} deposition to vegetation. However, to be more practically useful, more generalization is needed. Further field experiment data are necessary to better understand the new deposition model's ability to be widely applicable over different types of vegetation and windbreak designs. For example, Finch (1988) provides a list of species of vegetation that are particularly tolerant to mechanical damage from wind blown soils that should be better understood in the context of the new models. Further, the USDA (1999) provides recommendations and standards for windbreak/shelterbelt establishment. Understanding the effectiveness of these recommended windbreaks in terms of turbulent transport and deposition on a species-specific basis is a critical need. In addition, the QUIC model should also be evaluated for a larger range of particle sizes so as to ensure its usefulness for other practical applications including windbreak interactions with snow and sand particles. Additional field datasets would be necessary to do this.

6. Literature Cited

Arya, S. P., 2001. Introduction to micrometeorology, 2nd Edition. Academic Press, New York.

Amatul U., 2006. Implementation and validation of particle transport model for vegetation in Quick Urban Dispersion Modeling System. MS Thesis, Department of Mechanical Engineering, University of Utah, Salt Lake City, Utah.

Aylor, D., Ferrandino, F., 1989. Dispersion of spores released from an elevated line source within a wheat canopy. Bound.-Lay. Meteorol., 46, 251–273.

Aylor, D. E., Flesch T.K., 2001. Estimating spore release rates using a Lagrangian stochastic simulation model. J. Appl. Meteorol., 40, 1196-1208.

Bréda, N.J.J., 2003. Ground-based measurements of leaf area index: a review of methods, instruments and current controversies. J. Exp. Botany, 54, 2403-2417.

Bradley, E. F., Mulhearn, P. J., 1983. Development of velocity and shear stress distributions in the wake of a porous shelter fence, J. Ind. Aerod., 15, 145-156.

Bruun, H.H., 1995. Hot-wire anemometry: principles of signal analysis. Oxford University Press, New York.

Chapra, S.C., Canale, R.P., 2006. Numerical methods for engineers. McGraw Hill, New York.

Cheng-I, H., Katul, G., Tze-wen, C., 2000. An approximate analytical model for footprint estimation of scalar fluxes in thermally stratified atmospheric flows. Adv. Water Resour., 23, 765-772.

Choudhury, B. J., and Monteith, J. L. (1988). A four-layer model for the heat budget of homogeneous land surfaces. Q. J. Roy. Meteorol. Soc., 114, 373–398.

Cionco, R.M., 1965. Mathematical model for air flow in vegetative canopy.
J. Appl. Meteorol., 4, 517–522.

Comte-Bellot, G., Corrsin, S., 1965. The use of a contraction to improve the isotropy of grid-generated turbulence. J. Fluid Mech., 25 657-682.

Counihan, J.C.R., Hunt, Jackson P.S., 1974. Wakes behind two-dimensional surface obstacles in turbulent boundary layers, J. Fluid Mech., 64, 529-563.

Etyemezian V., Ahonen S., Nikolic D., Gillies J., Kuhns H., Gillette D., Veranth J., 2004. Deposition and removal of fugitive dust in the arid southwestern United States: measurements and model results. J. Air Waste Manag. Assoc., 54, 1099–1111.

Finch, S.J., 1988. Field windbreaks: design criteria. Agr. Ecosyst. Environ., 22, 215–228.

Guan, D., Zhang, Y., Zhu, T., 2003. A wind-tunnel study of windbreak drag. Agr. Forest meteorol., 118, 75-84.

Hinds, W.C., 1982. Aerosol technology: properties, behaviors, and measurement of airborne particles. Wiley, New York.

Judd M.J., Raupach M.R., Finnigan J.J., 1996. A wind tunnel study of turbulent flow around single and multiple windbreaks, part1: velocity fields. Bound.-Lay. Meteorol., 80, 127-165.

Mao, Y., Wilson, J.D., Kort, J., 2013. Effects of a shelterbelt on road dust dispersion. Atmos. Environ., 79, 590-598.

May, K.R., Clifford, R., 1967. The impaction of aerosol particles on cylinders, spheres, ribbons, and discs. Ann. Occup. Hyg., 10, 83-95.

Marple, V., Liu, B., 1974. Characteristics of laminar jet impactors. Environ. Sci. Technol., 8, 648-654.

Moran, S.M., Pardyjak, E.R., Veranth, J.M., Speckart, S.O., Edmunds, B.L., Stoll, J.R., 2011. Developing strategies for fugitive dust mitigation and transport flux using native vegetative windbreaks for dust control. Proceedings for Student Poster and Paper Session. Air and Waste Management Association, Orlando, FL, Paper #16.

Pace, T.G., 2005. Methodology to estimate the transportable fraction (TF) of fugitive dust emissions for urban scale air quality analyses. USEPA. (8/3/2005 Revision) http://www.epa.gov/ttnchie1/emch/dustfractions/transportable_fraction_080305_rev.pdf

Pardyjak, E.R., Brown, M.J., 2001. Evaluation of a fast-response urban wind model: comparison to single building wind-tunnel data. Proceedings of the 3rd International Symposium on Environmental Hydraulics. D. Boyer and R. Rankin (Eds.), Tempe, AZ.

Pardyjak, E.R., Speckart, S., Yin, F., Veranth, J.M., 2008. Near source deposition of vehicle generated fugitive dust on vegetation and buildings: model development and theory. Atmos. Environ., 42, 6442-6452.

Perera, M., 1981. Shelter behind two-dimensional solid and porous fences, J. Wind Eng. Ind. Aerod., 8, 93-104.

Pope, S.B., 2000. Turbulent flows. Cambridge University Press, New York.

Raupach, M.R., Woods, N., Dorr, G., Leys, J.F., Cleugh, H.A., 2001. The entrapment of particles by windbreaks. Atmos. Environ., 35, 3373–3383.

Seinfeld, J.H., Pandis, S.N., 1998. Atmospheric chemistry and physics: from air pollution to climate change. Wiley, New York.

Singh, B., Hansen, B., Brown, M.J., Pardyjak, E.R., 2008. Evaluation of the QUIC-URB fast response urban wind model for a cubical building array and wide building street canyon, Environ. Fluid Mech., 8, 281-312.

Singh, B., Pardyjak, E.R., Norgren, A., Willemsen, P., 2011. Speeding-up urban fast response Lagrangian dispersion simulations using video game technology, Environ. Model. Softw., 26, 739-750.

Slinn, W.G.N., 1982. Predictions for particle deposition to vegetative canopies. Atmos.Environ., 16, 1785–1794.

Speckart S.O., Pardyjak E.R., 2013. Removal of PM_{10} in the near-source zone downwind of unpaved roads part 1: field study, in-prep, to be submitted to Atmos. Environ.

Tabler, R.D., 1991. Snow fence guide. Strategic Highway Research Program, Report SHRP-W/FR-91-106. National Research Council, Washington, D.C.

Tabler, R.D., 1992. What's new in fences for snow, sand, and wind control, Proceedings of the 97th Annual Conference, American Railway Bridge and Building Association, Chicago, Illinois, 188-195.

Tennekes, H., Lumley, J.L., 1972. A first course in turbulence. The MIT Press, Cambridge.

T.S.I., 2010. Model 8520 DustTrak Aerosol Monitor Operation and Service Manual 1980198, Revision S, Shoreview, MN.

USDA, 1999. Natural Resources Conservation Service. CORE4 Conservation Practices. Chapter 3j: Windbreak/Shelterbelt.

Van Ulden, A.P., 1978. Simple estimates for vertical diffusion from sources near the ground. Atmos. Environ., 12, 2125-2129.

Venkatram, A., 2004. On estimating emissions through horizontal fluxes. Atmos. Environ., 38, 1337-1344.

Veranth, J.M., E.R. Pardyjak, Seshadri, G., 2003. Vehicle-generated dust transport: analytic models and field study, Atmos. Environ., 37, 2295-2303.

Warner, S., Platt, N., Heagy, J.F., 2004. Comparisons of transport and dispersion model predictions of the URBAN 2000 field experiment. J. Appl. Meteorol., 43, 829–846.

Williams, M.D., Brown, M.J., Boswell, D., Singh, B., and E.R. Pardyjak, 2004: Testing of the Quic-Plume model with wind-tunnel measurements for a high-rise building, Fifth AMS Symposium on the Urban Environment, Vancouver, BC, J5.3.

Wilzack, J.M., Oncley, S.P., Stage, S.A., 2001. Sonic anemometer tilt corrections algorithms. Bound.-Lay. Meteorol., 99, 127-150.

Woods, N., Craig, I.P., Dorr, G., Young, B., 2001. Spray drift of pesticides arising from aerial application in cotton. J. Environ. Qual., 30, 697–701.

Zhu, D., Kuhns, H.D., Gillies, J.A., Etyemezian, V., Gertler, A.W., Brown, S., 2011. Inferring deposition velocities from changes in aerosol size distributions downwind of a roadway. Atmos. Environ., 45, 957-966.

Appendix A. T.S.I. DustTrak Colocation Tests

The DustTrak sensors used in both of the new field experiments reported here were rented from Galson Labs (http://galsonlabs.com/) and Argus-Hazco (http://argus-hazco.com/). The companies calibrate the instruments prior to shipment. DustTrak monitors are calibrated to PM_{10} concentrations by the utilizing the respirable fraction of Arizona Road Dust (ISO 12103–1, A1). Further, just prior to each of the field tests, on-site colocations test were conducted. Each test consisted of placing all of the instruments at 2.5 m above ground level and sampling for 95 min. All DustTraks were located 2 – 3 m downwind of traffic generated by a vehicle. Table A1 shows the results from the Malta Raft River Windbreak Experiment colocation test. The data indicate a standard deviation of 0.32 mg/m^3 if DT_RS_1 is included. If that sensor is omitted the standard deviation is 0.068 mg/m^3. For the Hanford tests (Table A2) the standard deviation was 0.062 mg/m^3.

DT_21	0.298	mg/m^3
DT_22	0.466	mg/m^3
DT_31	0.364	mg/m^3
DT_32	0.48	mg/m^3
DT_33	0.395	mg/m^3
DT_34	0.294	mg/m^3
DT_41	0.347	mg/m^3
DT_42	0.312	mg/m^3
DT_RS_1	1.352	mg/m^3
DT_UP	0.372	mg/m^3

Table A1 – Comparison of the concentrations measured during colocation tests for the Malta, ID Raft River Windbreak Experiment.

DT_1	0.413	mg/m^3
DT_2	0.432	mg/m^3
DT_3	0.413	mg/m^3
DT_4	0.384	mg/m^3
DT_5	0.536	mg/m^3
DT_6	0.482	mg/m^3
DT_7	0.554	mg/m^3
DT_8	0.436	mg/m^3

Table A2 – Comparison of the concentrations measured during colocation tests for the Handford, WA tests.

Appendix B. List of Scientific/Technical Publications

1. Peer-Reviewed Journal Articles:
    a. Moran, S.M., E.R. Pardyjak, and J.M. Veranth, 2013. Understanding the role of grid turbulence in enhancing PM_{10} deposition: Scaling the Stokes number with R_λ, *Physics of Fluids*, **25**, 115103; http://dx.doi.org/10.1063/1.4829451.
    b. Speckart, S.O. and E.R. Pardyjak, A method for rapidly computing windbreak flow field variables, <u>submitted</u>, *Journal of Wind Engineering and Industrial Aerodynamics*, December 2013.
    c. Speckart, S.O., J.M. Veranth, and E.R. Pardyjak, Removal of PM_{10} in the near-source zone downwind of unpaved roads. Part I: Las Cruces, NM field Study, <u>in-preparation</u> for submission to *Atmospheric Environmen*t, manuscript available upon request.
    d. Speckart, S.O., J.M. Veranth, and E.R. Pardyjak, Removal of PM_{10} in the near-source zone downwind of unpaved roads. Part 2: Quantifying near-source capture, <u>in-preparation</u> for submission to *Atmospheric Environmen*t, manuscript available upon request.

2. Thesis/Dissertations
    a. Moran, S., 2012. The influence of vegetative windbreaks on fugitive dust (PM_{10}) mitigation and transport flux: the role of turbulence in enhancing particulate deposition. MS Thesis, University of Utah.
    b. Speckart, S.O., 2013. Numerical modeling and field measurement of vehicle-generated road dust transport and removal near the road. PhD Thesis, University of Utah.
    c. Price, T., 2014 (In preparation). Toward understanding the role of turbulence in enhancing particle deposition onto vegetation. MS Thesis, University of Utah
3. Conference Proceedings
    a. Moran, S.M., E.R. Pardyjak, S.O. Speckart, B.L. Edmunds, and J.M. Veranth, 2011. Developing strategies for fugitive dust mitigation and transport flux using native vegetative windbreaks for dust control, 2011 Air & Waste Management Associations Conference & Exposition, June 21-24, Orlando, FL, Paper #16.
4. Conference/Symposium Abstracts
    a. Price, T., E. Pardyjak, J. Veranth, and S. Moran, 2012. Toward understanding the role of turbulence in enhancing particle deposition onto vegetation. AAAR 31th Annual Conference Minneapolis, Minnesota, USA, October 8-12, 2012, Paper Number: 10.AP.3.